Fall 2018

Predicted Deepwater Bathymetry From Satellite Altimetry: Non-Fourier Transform Alternatives

Maxsimo Salazar
University of Southern Mississippi

PREDICTED DEEPWATER BATHYMETRY FROM SATELLITE ALTIMETRY: NON-FOURIER TRANSFORM ALTERNATIVES

by

Maxsimo Salazar

A Dissertation
Submitted to the Graduate School,
the College of Arts and Sciences
and the School of Ocean Science and Engineering
at The University of Southern Mississippi
in Partial Fulfillment of the Requirements
for the Degree of Doctor of Philosophy

Approved by:

Jerry Wiggert, Committee Chair
Stephan Howden
David Wells
Paul Elmore
Juliette W. Ioup
Ian Church

_____	_____	_____
Dr. Stephan Howden	Dr. Jerry Wiggert	Dr. Karen S. Coats
Committee Chair	Director of School	Dean of the Graduate School

December 2018

Published by the Graduate School

ABSTRACT

Robert Parker (1972) demonstrated the effectiveness of Fourier Transforms (FT) to compute gravitational potential anomalies caused by uneven, non-uniform layers of material. This important calculation relates the gravitational potential anomaly to sea-floor topography. As outlined by Sandwell and Smith (1997), a six-step procedure, utilizing the FT, then demonstrated how satellite altimetry measurements of marine geoid height are inverted into seafloor topography. However, FTs are not local in space and produce Gibb's phenomenon around discontinuities. Seafloor features exhibit spatial locality and features such as seamounts and ridges often have sharp inclines. Initial tests compared the windowed-FT to wavelets in reconstruction of the step and saw-tooth functions and resulted in lower Root Mean Square (RMS) error with fewer coefficients. This investigation, thus, examined the feasibility of utilizing sparser base functions such as the Mexican Hat Wavelet, which is local in space, to first calculate the gravitational potential, and then relate it to sea-floor topography, with the aim of improving satellite derived bathymetry maps.

ACKNOWLEDGMENTS

I would like to acknowledge Dr. Paul Elmore of the Naval Research Laboratory, Geo-Sciences Division for allowing me to do my dissertation as part of his research into sparsity and machine learning, Dr. Juliette Ioup of the University of New Orleans for help on wavelet transforms, and the rest of my committee, Dr. Stephan Howden (Committee Chair), Dr. David Wells, both of the University of Southern Mississippi, as well as Dr. Ian Church of the University of New Brunswick for their patient support and keen insights.

DEDICATION

I would like to sincerely thank the leadership of the Naval Research Laboratory for allowing me the opportunity and time to continue my studies. Without their support, this work would not be possible. I would also like to thank Dr. Brenda Little, Senior Scientist with the Naval Research Laboratory, Oceanography Division for her mentorship, guidance on technical writing and friendship. Finally, I give thanks to my family who encouraged me throughout the many long days and evenings that went towards my degree. I am forever grateful to them.

TABLE OF CONTENTS

LIST OF TABLES

LIST OF ILLUSTRATIONS

LIST OF ABBREVIATIONS

COI	Cone of Influence
CWT	Continuous Wavelet Transform
DOG	Derivative of the Gaussian
DWT	Discrete Wavelet Transform
FFT	Fast Fourier Transform
FT	Fourier Transform
FT(MHW)	FT of the Mexican Hat Wavelet
iFFT	Inverse Fast Fourier Transform
MHW	Mexican Hat Wavelet
MHWF	Mexican Hat Wavelet Family
PSD	Power Spectral Density
RMSE	Root Mean Square Error
SEPR	Southern East Pacific Rise
SNR	Signal to Noise Ratio
STFT	Short Time Fourier Transform
WT	Wavelet Transform

CHAPTER I – INTRODUCTION

1.1 Overview, Background and Motivation

In the public domain, eighty percent of Earth's ocean floor in ice-free regions remain unmapped by sonar systems (Sandwell et al., 2014). Mappings for the remainder of Earth's deep-water (> 1km depth) undersea topography in ice-free regions is by inversion of marine geoid height to topography (Smith and Sandwell, 1994 & 1997). Marine geoid height is obtained by satellite altimetry, in which two-way travel time of a radar signal sent by the satellite and reflected back by the ocean surface provides altitude above the Earth (Chelton et al., 2001), (Wolfgang Torge, 2012)). Seafloor topographic features > 15 km in size and > 1 km in height such as seamounts, mid-ocean ridges, trenches, etc. cause enough near-field anomalies in gravity for static undulations to form over these features that are large enough to be measured in the altimeter spatio-data series data (Sandwell and Smith, 1994; Sandwell et al., 2014). These data are processed (Garcia et al. 2015) to create grid data products of the geoid, gravity field, vertical gravity gradient, and vertical gravity deflection for public download (Pavlis et al. 2012, Sandwell et al., 2014).

This inversion of the geoid to seafloor topography requires two sets of analytic equations involving Newtonian physics and satellite altimeter measurements. Parker (1972) published the potential solution for the part of the inversion that was computable. Using Newtonian gravitational potential, Parker's theory relates a convergent infinite series of Fourier transform (FT) of undersea topography, $\mathcal{F}[h(x,y)]$, to the FT of the vertical component of the gravity anomaly, $\mathcal{F}[\Delta g(x,y)]$, (Fig. 1). The second part of the inversion comes from Haxby et. al. (1983). Given measurements of marine geoid height,

$N(x,y)$, their paper provides the equation to relate the FT of the geoid gradient, $\mathcal{F}\left[\nabla_{x,y}N(x,y)\right]$, to $\mathcal{F}[\Delta g(x,y)]$. With both pieces, $\mathcal{F}[h(x,y)]$ is predictable from $\mathcal{F}\left[\nabla_{x,y}N(x,y)\right]$ using $N(x,y)$ from satellite altimeter measurements.

With these equations, Smith and Sandwell (1994, 1997) created their algorithms to process geoid height to predicted bathymetry, using only the first term from the infinite series of $\mathcal{F}[h(x,y)]$. For the data they had in the 1990's, they found that the correlation between bathymetry and gravity resided between a limited band of wavelengths in the gravity field, $\lambda(x,y) = 1/\left|\vec{k}(x,y)\right|$, from 15 and 160 km. Wavelengths in the gravity field less than 15 km resulted in a small signal to noise ratio (SNR) making prediction unobtainable for navigation; whereas, wavelengths greater than 160 km produced no gravity anomaly due to isostatic compensation (Smith & Sandwell 1994). Smith and Sandwell (1994) calculated total predicted bathymetry as the sum of passband prediction and long-wavelength regional depth. The passband prediction was the product of downward continued gravity that is also band-pass filtered and a scaling factor.

Smith and Sandwell published their first version of worldwide predicted bathymetry in 1997 in the journal *Science*. Since then, they have continued to use new multibeam data, data from new satellite altimeter missions, and re-tracked satellite altimetry data (Sandwell and Smith, 2009) to produce newer versions of predicted bathymetry. The current version is Version 17.1 (Scripps Institute of Oceanography, 2014).

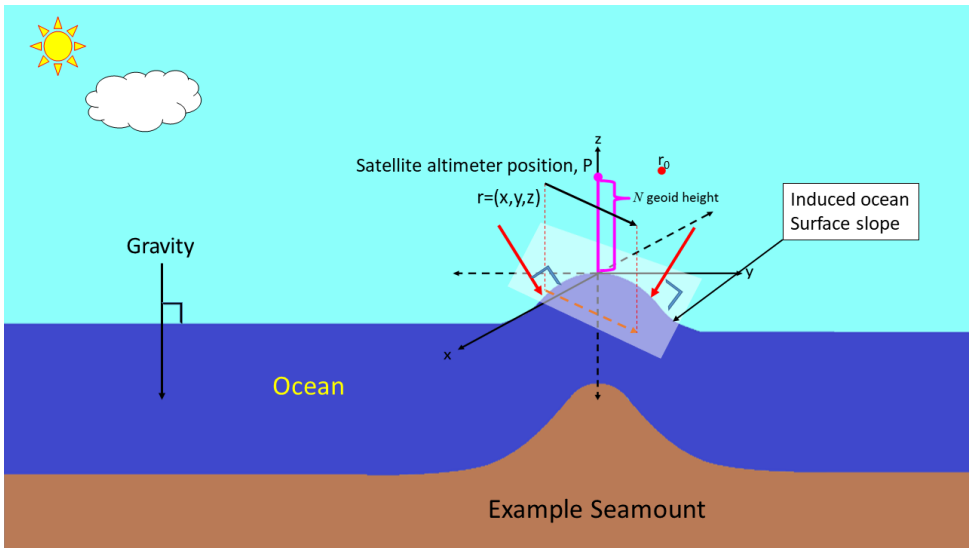

Figure 1.1 The Geometry of Parker's Paper.

This is the geometry of Parker's paper on top of a background image courtesy of NOAA.

1.2 New Approach

Although Fourier transforms are a proven mathematical tool and rapidly computable, they are not without issue. Specifically, although their basis functions are local in wavenumber, they are not local in space. Seafloor features, however, exhibit spatial locality, meaning that the amplitude goes to zero away from the object. Thus, the FT of seafloor topography will have a wide spectrum of wavenumber components, requiring computation of many Fourier coefficients, because the components have constant amplitude from $-\infty$ to $+\infty$. Small changes in the transform will produce changes everywhere in the spatial domain (Vidakovic & Mueller, 1991). As a result, the root-mean-square error (RMSE) in the transform will eventually reach a lower limit that is pragmatically unreducible without the use of a different transformation method.

The proposed dissertation effort focuses on the applicability of alternate transformation methods to perform the inversion. Specifically, these transformation methods were sparse representations of seafloor features. The transformation of a signal from a basis space (dense measurements required for characterization) to a new basis space that requires only minimal measurements or terms is defined as a sparse representation (Elad, 2010; Starck et. al. 2010). Sparse representations enable lower RMSE between original and constructed information because there is better correlation term-by-term in the sparse transform space compared to a dense transform space. In contrast, the FT is a dense representation for seafloor features.

If a sparse representation could be found to replace the Fourier method, the associated RMSE of inversion calculations to get $h(x, y)$ from $N(x, y)$ could be lowered. The result could reduce uncertainty of sea floor topography heights and the location and depths of navigational hazards. Using different sparse transform methods may not only maximize the use of new satellite systems but also help to capitalize on older systems and data.

The aim of this research is to determine what candidate sparse basis function will best remediate the resolution problem. However, sparse basis functions are well known to require heavy computational power (Elad, 2010). Unlike the time in the early 1990's in which the Smith and Sandwell work appeared, computational power is now orders of magnitude larger, making computationally intractable problems that existed then to be potentially applicable now.

A determination of what candidate sparse basis functions, in lieu of the FT, are capable of providing an increase in resolution of the inverse transformation was the first

step. Candidate functions that exhibit localization include wavelets, ridgelets, curvelets, contourlets and fractals (Starck et al., 2010). The second Derivative of the Gaussian (DOG) named the Ricker Wavelet, is also known as the Mexican Hat Wavelet (MHW) due to its sombrero-like shape (Daubechies, 1992; Ryan, 1994). The MHWs are real zero-phase functions that consist of a central peak with two smaller lobes on either side; and, they are uniquely specified by a singular frequency parameter, which is its peak frequency (Ryan, 1994).

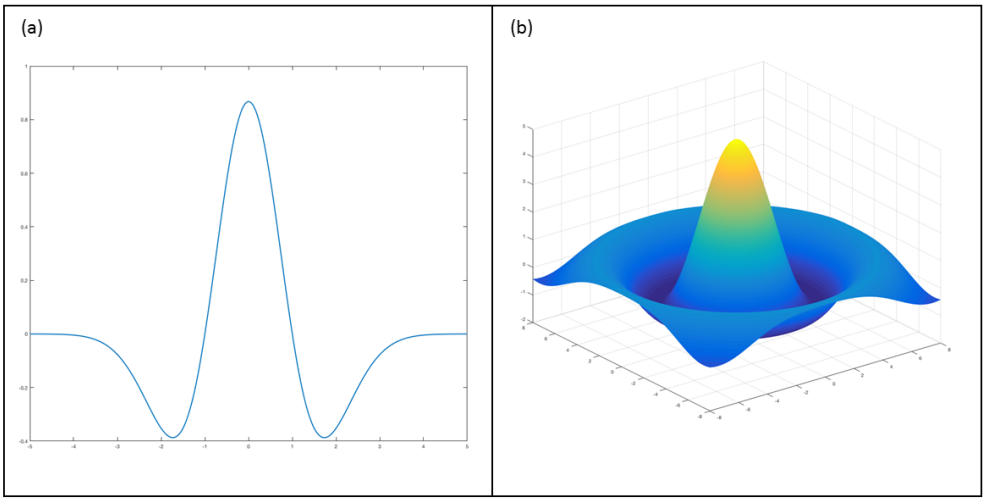

Figure 1.2 The 2D and 3D MHW

Figure a is the 2D MHW and figure b is the 3D MHW.

This particular wavelet and its extension to the sphere have been used extensively to detect structures on a 2D image, utilizing signal amplification to move from real to wavelet space (Argueso et al., 2006). Also, because the MHW is circularly symmetric, its FT results in a zero order Hankel function, many solutions for which are listed in tables. Unlike the FT, wavelets are local in both frequency and time (Vidakovic & Mueller, 1991) and wavenumber and space. Further, many different function classes are

more compactly represented by wavelets than FTs, such as functions with discontinuities and sharp spikes (Vidakovic & Mueller, 1991). Further reasons for selecting the MHW as the initial candidate are its properties as a non-orthogonal, real valued function, capable of separating both positive and negative values of time series oscillations into separate peaks in wavelet power (Torrence & Compo 1998). When a smooth and continuous variation in wavelet amplitude is expected, non-orthogonal transforms are of great utility in time series analysis (Torrence & Compo 1998). Further, they have a very small cone of influence (COI), thus less affected by edge effects (Torrence & Compo 1998). For these reasons, the primary candidate function tested was the MHW. An attempt was made to produce inverse solutions using similar procedures that Parker (1972) and Sandwell and Smith (2009) used in their methods, however, utilizing the MHW.

Ridgelets, contourlets and fractals were also considered for their practicality in this problem, though, due to time constraints were not applied during this study. Like the MHW, these basis functions should be studied. Should the methods proposed decrease RMSE, then compressed sensing algorithms should be considered to calculate the coefficients of the candidate basis functions. One last alternative method, however, was also considered. As highlighted by Argueso et al. (2006), the calculation of the basis function coefficients can be made by taking the FT of the basis function. In the case of Argueso et at. (2006) for the Mexican Hat Wavelet Family (MHWF), the iterative process of applying the Laplacian to the MHW, produced the set of basis functions. This technique employed the use of the signal's amplification moving from real to wavelet space (Argueso et al., 2006). They credited their technique's success of point source

detection in cosmic microwave background maps on the fact that wavelets amplified the ratio between the background dispersion and point source intensity. Thus, this method was thought to allow for a comparison of results of two different approaches such that a determination could be made as to which was more efficient and computationally more practical.

1.3 Hypotheses

- H1: The application of sparse basis functions to satellite altimetry data will result in a lower RMSE than the Fourier transform approach when predicting Newtonian gravitational potential with fewer coefficients.
- H2: These functions then, will be applicable for sparse transformation operations to predict higher resolution bathymetry.
- H3: Taking the Fourier transform of the candidate basis functions to calculate their coefficients will also result in a decrease in RMSE and may result in an analytical solution.

1.4 Proposed Test Case

Due to the extensive amount of research conducted at the Southern East Pacific Rise (SEPR), this area was used to test the hypotheses. A quick scan of the area via Global Multi-Resolution Topography (GMRT) visualizations (powered using Google Earth) revealed several seamounts that could be used as test cases.

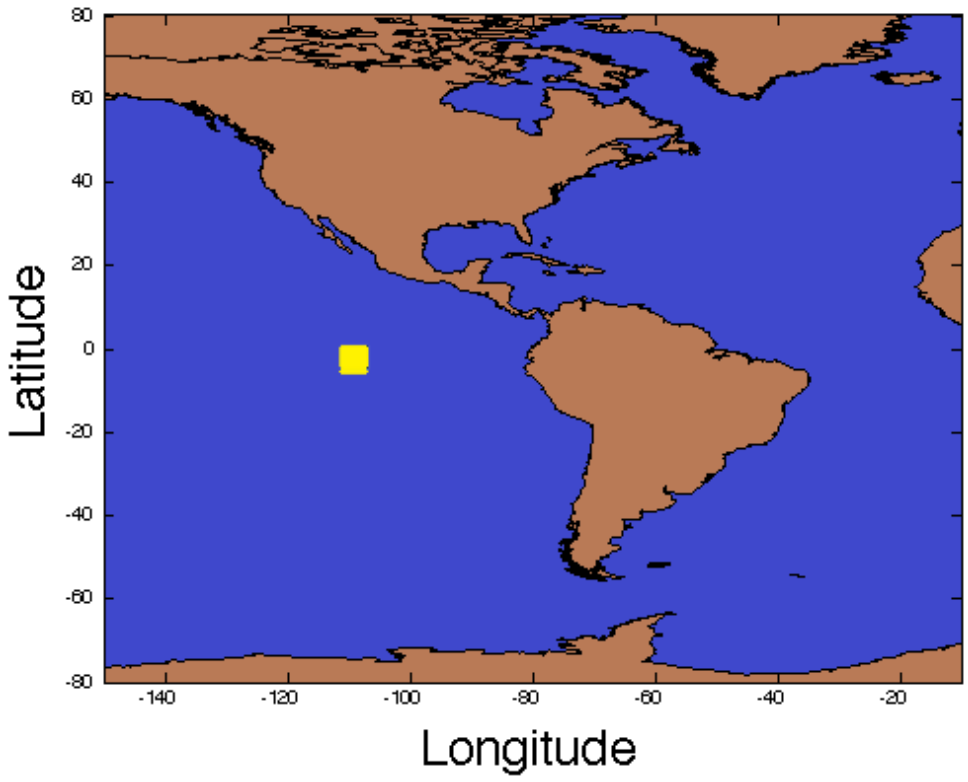

Figure 1.3 Area of interest: Southern East Pacific Rise (From Google Earth)

1.5 Importance of Work

The practicality of this approach lies in its economic as well as ecological utility. As Fourier methods do not produce the level of resolution required for navigation in naval warfare, general scientific and commercial needs, increased costly sea time would be required to resolve this issue as the fruits of increases in satellite resolution cannot be met with current calculation methods. In fact, it was estimated that an approximate 900 ship years would be required to complete a complete multibeam survey of the world's oceans (Weatherall 2015). However, the cost of applying a different mathematical/computational approach to the current data is low.

1.6 Proposed Approach

Application of various transforms to the earth's gravitational potential was attempted including the MHW, the Paul wavlet and Morlet wavelet. The Mexican Hat Wavelet, was the first transform applied to the earth's gravitational potential. A numerical solution was obtained. Data from the Southern Eastern Pacific Rise was applied to the transform solutions and then compared to the method used by Parker (1972) and Smith & Sandwell (1994) using Fourier transforms, by calculating the RMSE of both. Transform performance was evaluated by comparing each tested method against each other with regards to RMSE vs. number of coefficients, utilizing the same datasets.

1.7 Constraints

In order to provide a clear and focused research directive, the following constraints were made. The data considered was from the Juan de Fuca Ridge. Bathymetry and gravity data for tests are publically available through the Global Multi-Resolution Topography synthesis database (Ryan et al. 2009). Because there are large amounts of data for this particular site, and it is well studied, any test results can be met with greater certainty of truth than for other areas not as well studied. All geoid height datasets used were strictly from satellite altimetry with the intent to invert the data to derive bathymetry. To further constrain the research timeline, only a few basis functions were considered. The first priority for testing of the basis functions was the Mexican Hat wavelet followed by the Paul and Morlet wavelets. There is great utility in applying these same methods to increasing resolution between satellite altimeter tracks. Resolution is highest on the tracks but drops between them. However, this line of study

was not tested due to time constraints, but should be considered for future research interests

CHAPTER II - BACKGROUND

(Kellogg, 1953) defined the gravity potential or Newtonian potential as "the work done by the field on a test particle." As the gravitational field is conservative, net work is not required to move a mass around a closed loop (Blakely 1995) which makes the concept of gravity potential useful. To begin this study and further understand the concepts behind the gravitational potential, a review of some basic principles was required. Key among them is the principle of superposition which states that the interaction of two stimuli is completely unaffected by the presence of others, thus the combination of two or more potentials may be taken simply as their sum (Griffiths 1981). Following this convention, the gravitational potential of a group of masses is defined as the sum of the individual masses' potentials (Blakely 1995). This concept will prove useful when considering the potential of a mass source in conjunction with a smooth flat earth later in the study. Fundamentally, however, this study will begin with simpler problems and build from there. Blakely (1995) first considered the potential of a mass distribution expressed as:

$$U(P) = \gamma \int_S \frac{\sigma(S)}{r} dS, \tag{2.1}$$

where γ is Newton's gravitational constant, σ is the surface mass density and r is the distance from a point P to any point on the sphere (see figure 2.1). From this expression, Blakely went on to define the gravitational potential of various geometries such as a spherical shell, both inside and out, a solid sphere, which is a special case of a spherical shell, as well as the potentials of finite and infinite wires.

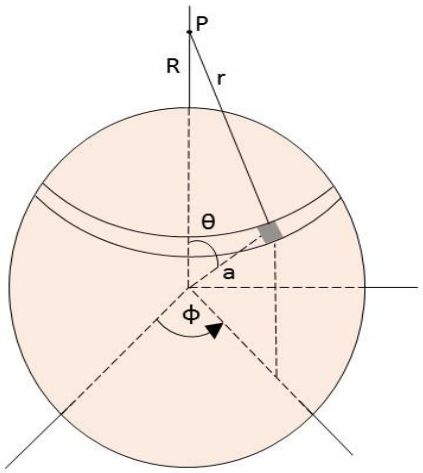

Figure 2.1 Thin walled spherical shell.

Reproduction of figure 3.3 from Blakely of a thin walled, spherical shell of radius a with an observation point at P

After a review of the derivations by Blakely of the gravitational potential of these simple geometries, attempts at arriving at the same results were made. Upon successful completion, Blakely's discussion of the application of the Fourier Transform to these potentials was also reviewed. Table 11.1 of Blakely (1995) lists a number of gravitational attraction potentials and their Fourier transforms. Gravitational attraction is related to the gravitational potential in that it is simply its gradient (Blakely 1995). Below is a systematic derivation of the top four transforms listed in the table per Blakely (1995), however, for gravitational potential not attraction.

2.1 Monopole

The gravitational potential observed on a horizontal plane at the point $z=z_0$ that is caused by a point mass located below the plane is considered and is given by the formula

$$U(P) = \frac{\gamma\mu}{r} \tag{2.2}$$

where μ is the point mass in question, γ remains the gravitational constant and r is the distance to the horizontal plane from the point mass. Pulling the two constants outside, the Fourier transform is then expressed as:

$$\mathcal{F}[U] = \gamma\mu\mathcal{F}\left[\frac{1}{r}\right] \tag{2.3}$$

However, we know from Blakely (1995) that due to cylindrical symmetry about the z-axis, after transformation into cylindrical coordinates a Hankel transform of zeroth order ensues that result in the following expression:

$$\mathcal{F}\left[\frac{1}{r}\right] = 2\pi\frac{e^{|k|(z_0-z')}}{|k|}, z' < z_0, |k| \neq 0 \tag{2.4}$$

Thus,

$$\mathcal{F}[U] = 2\pi\gamma\mu\frac{e^{|k|(z_0-z')}}{|k|}, z' < z_0, |k| \neq 0 \tag{2.5}$$

2.2 Vertical Line

For the case of the vertical line we with start with its potential given by Blakely

$$U(P) = \gamma\rho\int_{-a}^{a}\frac{1}{r}dz'$$

where ρ is density and the limits a and –a will be the points z_2 and z_1, respectively. Again, we can note the solution of the Fourier transform of 1/r. As such, we have the following:

$$\mathcal{F}[U] = 2\pi\gamma\lambda\int_{z_1}^{z_2}\frac{e^{|k|(z_0-z')}}{|k|}dz', z_2 > z_1 \tag{2.6}$$

where λ is the mass per unit length of the wire. After removal of the constants to outside of the integral and then integration, we end up with the solution

$$\mathcal{F}[U] = \frac{2\pi\gamma\lambda}{|k|^2}e^{|k|z_0}\left(e^{-|k|z_1} - e^{-|k|z_2}\right) \tag{2.7}$$

This equation will be used again in a later section.

2.3 *Calculation of Gravitational Potential Anomaly*

The process of inversion of satellite altimetry measurements of marine geoid height to seafloor topography, is covered in conjunction by two papers, the theory by Robert Parker (1972), "The Rapid Calculation of Potential Anomalies" and the 1997 Sandwell and Smith paper, "Marine Gravity Anomaly from Geosat and ERS 1 Satellite Altimetry." A six-step process of this procedure is detailed below.

The first step is to derive the Newtonian gravitational potential of a vertical line segment mass whose density is given by

$$\rho(\hat{\boldsymbol{r}}) = \lambda\delta(x)\delta(y) \tag{2.8}$$

between z_1 and z_2 and zero elsewhere, where λ is a finite positive constant, and $z_1<z_2$.

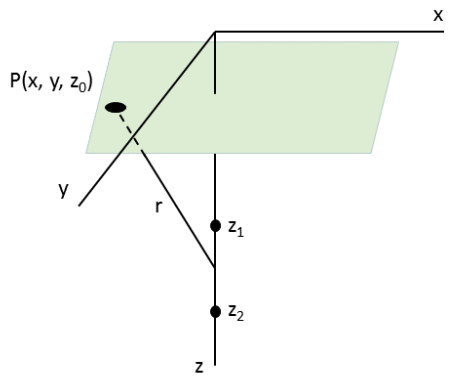

Figure 2.2 Coordinate system adopted after Blakely (1996).

We start with the general formula for the Newtonian Potential of mass distribution

$$U(P) = \gamma \iiint_V \frac{\rho(Q)}{r} dV \tag{2.9}$$

Substitution of $\rho(\vec{r})$ into the above equation yields:

$$U(P) = \gamma \iiint_V \frac{\rho(Q)}{r} dV = \gamma \iiint_V \frac{\lambda\delta(x)\delta(y)}{r} dV \quad (2.10)$$

As, λ is a finite constant, it can move outside of the integrals; and, after conversion of "r" to Cartesian coordinates,

$$\gamma\lambda \iiint_V \frac{\delta(x)\delta(y)}{[(x-x_0)^2+(y-y)^2+(z-z_0)^2]^{\frac{1}{2}}} dV \quad (2.11)$$

However, the triple volume integral is evaluated from negative to plus infinity for x and y. Thus, it can be noted that

$$\int_{-\infty}^{\infty} \delta(x)dx = 1 \quad \text{and} \int_{-\infty}^{\infty} \delta(y)dy = 1 \quad (2.12, 2.13)$$

Further, we know that

$$\int_{-\infty}^{\infty} f(x)\delta(x)dx = f(a) \quad (2.14)$$

If we consider x and y to be centered at the origin, with the x-y plane at z=0 and set a=0, then we can simplify the integral to the form

$$U(P) = \gamma\lambda \int_{z_1}^{z_2} \frac{1}{[(x-x_0)^2+(y-y)^2+(z-z_0)^2]^{\frac{1}{2}}} dz = \gamma\lambda \int_{z_1}^{z_2} \frac{1}{[(x_0^2)+(y_0^2)+(z-z_0)^2]^{\frac{1}{2}}} dz$$

(2.15)

A further simplification was made through the summation of x_0^2 and y_0^2 to some other constant r_0^2 yielding

$$\gamma\lambda \int_{z_1}^{z_2} \frac{1}{[r_0^2+(z-z_0)^2]^{\frac{1}{2}}} dz \quad (2.16)$$

Expansion of the denominator and rearrangement of the constant terms gives

$$\gamma\lambda \int_{z_1}^{z_2} \frac{1}{[z^2-2z_0z+(r_0^2+z_0^2)]^{\frac{1}{2}}} dz \quad (2.17)$$

which is in the form of an integral whose solution is listed on a standard table of integrals

$$\int \frac{1}{\sqrt{ax^2+bx+c}} dx \quad (2.18)$$

whose solution from Spiegel, (1968) is

$$\frac{1}{\sqrt{a}} ln \left| 2ax + b + 2\sqrt{a(ax^2 + bx + c)} \right| \tag{2.19}$$

Setting z_1=-a, z_2 =a and z_0=0, evaluation of the integral results in

$$U(P) = \gamma\lambda \left[ln \left| 2z_2 - 2z_0 + 2\sqrt{z_2^2 - 2z_0 z_2 + (r_0^2 + z_0^2)} \right| - ln \left| 2z_1 - 2z_0 + 2\sqrt{z_1^2 - 2z_0 z_1 + (r_0^2 + z_0^2)} \right| \right] \tag{2.20}$$

After further reductions (see Appendix C for full steps), the final solution is

$$U(P) = \gamma\lambda \, ln \left[\frac{a + \sqrt{a^2 + (r_0^2 + z_0^2)}}{-a + \sqrt{a^2 + (r_0^2 + z_0^2)}} \right] \tag{2.21}$$

The requirement is that the potential should vanish at infinity (Blakely, 1995). In order to prevent the potential from approaching infinity, a constant was added to the equation (Blakely, 1995).

$$U(P) = \gamma\lambda \left[ln \frac{a + \sqrt{a^2 + (r_0^2 + z_0^2)}}{-a + \sqrt{a^2 + (r_0^2 + z_0^2)}} - ln \frac{a + \sqrt{a^2 + 1}}{-a + \sqrt{a^2 + 1}} \right] \tag{2.22}$$

The potential as a $\rightarrow \infty$ is then

$$U(P) = 2\gamma\lambda \, log \frac{1}{r} \tag{2.23}$$

Utilizing Wolfram Alpha, the FT of this potential is given as

$$2\gamma\lambda \left[\frac{\sqrt{\frac{\pi}{2}}}{|k|} + \gamma^* \sqrt{2\pi}\delta(k) - \frac{i\pi^{3/2}\delta(k)}{\sqrt{2}} - \frac{\sqrt{\frac{\pi}{2}}}{k} \right] \tag{2.24}$$

where γ^* is the Euler-Mascheroni constant. If, however, like Parker (1972) we assume that density is constant, then the potential may be expressed as

$$U(P) = \gamma\rho \int_{z_1}^{z_2} \frac{1}{r} dz' \tag{2.25}$$

Recall equation 2.4

$$\mathcal{F}\left[\frac{1}{r}\right] = 2\pi \frac{e^{|k|(z_0 - z')}}{|k|}, z' < z_0, |k| \neq 0$$

Thus,

$$\mathcal{F}[U(P)] = 2\pi\gamma\lambda \int_{z_1}^{z_2} \frac{e^{|k|(z_0 - z')}}{|k|} dz', z_2 > z_1 \tag{2.26}$$

$$\mathcal{F}[U(P)] = \frac{2\pi\gamma\lambda}{|k|} e^{|k|z_0} \int_{z_1}^{z_2} e^{-|k|z'} dz' \tag{2.27}$$

$$\mathcal{F}[U(P)] = \frac{2\pi\gamma\lambda}{|k|} e^{|k|z_0} \left[\frac{-e^{-|k|z'}}{|k|}\right]\Bigg|_{z_1}^{z_2} \tag{2.28}$$

Thus, the solution is

$$\mathcal{F}[U(P)] = \frac{2\pi\gamma\lambda}{|k|^2} e^{|k|z_0}\left(e^{-|k|z_1} - e^{-|k|z_2}\right) \tag{2.29}$$

Parker (1972) considered the gravitational attraction of a layer of material with a lower boundary at $z = 0$ and an upper boundary defined at $z = h(\vec{\mathbf{r}})$. He further required that the layer vanish at a finite domain, D such that $h(\vec{\mathbf{r}}) = 0$ if $|\vec{\mathbf{r}}| > R$. It is also assumed that "h" is bounded and integrable. The Newtonian gravitational potential at $\vec{\mathbf{r}}_0$ due to a layer is

$$U(\vec{\mathbf{r}}_0) = \gamma\rho \int_V \frac{dV}{|\vec{\mathbf{r}}_0 - \vec{\mathbf{r}}|} = \gamma\rho \int_D dS \int_0^{h(\vec{\mathbf{r}})} \frac{dz}{|\vec{\mathbf{r}}_0 - \vec{\mathbf{r}}|} \tag{2.30}$$

Note: $\vec{\mathbf{r}}$ is a vector in x-y-z space and its projection onto the x-y plane is $\vec{r}$. In spherical coordinates: $\vec{r}$ is the source coordinates and $\overrightarrow{r_0}$ is the observation coordinates.

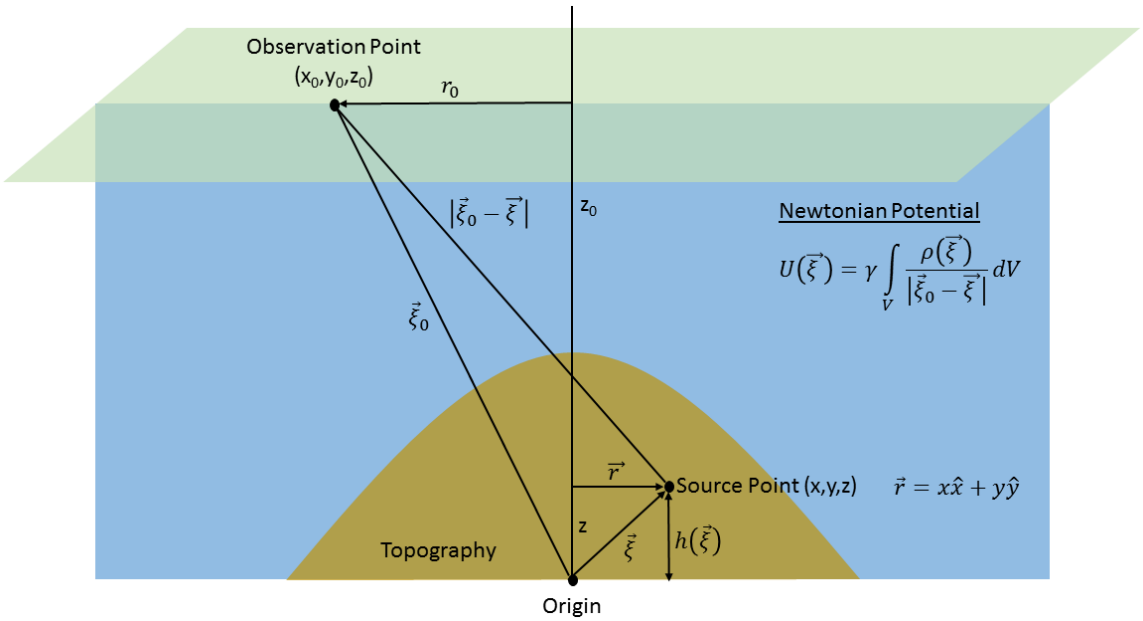

Figure 2.3 Geometric coordinate system adopted after Sandwell and Smith (1997).

Geometric coordinate system adopted after Sandwell and Smith (1997).

1. Define: $z = 0$ to be the mean seafloor within a domain of diameter D << diameter of the earth and is centered at the origin of the $x - y$ plane. Further, $R \equiv D/2$.
2. Any influence of gravitational source outside R to be zero (the layer disappears for $|\vec{\mathbf{r}}|$ > R.

From figure 2.3, the Newtonian gravitational potential from mass density source $\rho(\vec{\mathbf{r}})$ at the observation point $\vec{\mathbf{r}}_0$ from the layer is

$$U(\vec{\xi}_0) = \gamma \iiint \left[\frac{\rho(\vec{\mathbf{r}})}{|\vec{\xi}_0 - \vec{\xi}|}\right] dxdydz, \tag{2.31}$$

Note, $\vec{\xi}$ is the 3D distance from the origin to the source point and $\overrightarrow{\xi_0}$ is the 3D distance from the origin to the observation point.

Note: for consistency, here, the gravitational constant is represented by the lower case γ. However, in Parker's 1972 paper, the upper case Γ is used instead.

Parker then makes the assumption that $\rho(\vec{\mathbf{r}})$=ρ=constant. Thus,

$$U(\vec{\xi}_0) = \gamma\rho \iiint \left[\frac{dxdydz}{|\vec{\xi}_0 - \vec{\xi}|}\right] \tag{2.32}$$

The z-coordinate is then separated from the x-y plane to arrive at the following:

$$U(\vec{\xi}_0) = \gamma\rho \int_D dxdy \int_0^{h(\xi)} \frac{dz}{|\vec{\xi}_0 - \vec{\xi}|}, \tag{2.33}$$

where the $\int_D dxdy$ is the surface integral within the aperture D=2R. Furthermore, $h(\vec{\xi})$ is the height of the topography as a function of x and y ($h(\vec{\xi})$ = bathymetry(x,y)–regional depth(x,y)).

Applying a 2-D FT for the observation point in cylindrical coordinates $\vec{\xi}_0 = x_0\widehat{x_0} + y_0\widehat{y_0}$ with the form

$$\mathcal{F}[\mathrm{f}(\vec{\xi}_0)] = \int_X dS_0\, f(\vec{\xi}_0) e^{i\vec{k}\cdot\vec{\xi}_0}, \tag{2.34}$$

where $\vec{k} = k_x\hat{x} + k_y\hat{y}$ is the 2D wavenumber corresponding to $\vec{\xi} = x\hat{x} + y\hat{y}$ in transform space. This is done so that the 3-D vector $\vec{\xi} = \vec{r} + z\hat{z}$ and similarly for $\vec{\xi}_0$, results in the 2-D FT being

$$\mathcal{F}\,[U(\vec{\xi}_0)] \;=\; \gamma\rho \int_X dS_0 \int_D dS e^{i\vec{k}\cdot r_0} \int_0^{h(\xi)} \frac{dz}{|\vec{\xi}_0 - \vec{\xi}|} \tag{2.35}$$

After rearrangement the equation becomes

$$\mathcal{F}\,[U(\vec{\xi}_0)] \;= \gamma\rho \int_D dS \int_0^{h(\xi)} dz \int_X dS_0 \frac{e^{i\vec{k}\cdot\vec{\xi}_0}}{|\vec{\xi}_0 - \vec{\xi}|} \tag{2.36}$$

Equation 2.36 is the first equation at the top of page 449 of Parker (1972).

2.3.2 Intermediate Calculations

Although Parker cites Bracewell (1965) for going from Eq. (2.36) to the second equation that appears on page 449 of Parker (1972), this derivation is not intuitive. The equation referred to here from Parker is listed as Eq. (2.46) in this paper. The missing mathematical steps are given in this paragraph. To evaluate Eq. (2.36) the coordinate system needs to be in cylindrical coordinates. For continuity with Parker's paper, a switch is made from ξ to r. With coordinates given by script characters $(\mathcal{r}, \mathcal{z}, \vartheta)$, Eq. Eq. (2.36) becomes (Blakely, 1995)

$$\mathcal{F}\,[U(\vec{\mathbf{r}}_0)] \;= \gamma\rho \int_D dS \int_0^{h(\vec{\mathbf{r}})} d\mathcal{z} \int_X \frac{e^{i\vec{k}\cdot((w_0+\mathcal{r})\hat{\mathcal{r}}}}{(w_0^2+a^2)^{1/2}} w_0 dw_0 d\vartheta, \tag{2.37}$$

where

$$\vec{\mathbf{r}}_0 - \vec{\mathbf{r}} \;=\; (\mathcal{r}_0 - \mathcal{r})\hat{\mathcal{r}} \;+\; (\mathcal{z}_0 - \mathcal{z})\hat{\mathcal{z}} \tag{2.38}$$

$$|\vec{\mathbf{r}}_0 - \mathbf{r}| = [(\mathcal{r}_0 - \mathcal{r})^2 + \;(\mathcal{z}_0 - \mathcal{z})^2]^{1/2} \tag{2.39}$$

$$w_0 \equiv \mathcal{r}_0 - \mathcal{r} \tag{2.40}$$

$$a \equiv \mathcal{z}_0 - \mathcal{z} \tag{2.41}$$

In addition, $dw_0 = d\mathcal{r}_0$, $\mathcal{r}_0 = w_0 + \mathcal{r}$, and $dS = w_0 dw_0 d\vartheta$ in Eq. 2.33. The exponential in Eq. Eq. 2.33 can be factored such that

$$\begin{aligned}\exp\left(i\vec{k}\cdot((w_0+\mathcal{r})\hat{r}\right) &= \exp\left(i\vec{k}\cdot w_0\hat{r}\right)\exp\left(i\vec{k}\cdot\mathcal{r}\hat{r}\right) \\ &= \exp\left(i|\vec{k}|w_0\cos\vartheta\right)\exp\left(i\vec{k}\cdot\mathcal{r}\hat{r}\right)\end{aligned} \tag{2.42}$$

Using this result in Eq. 2.33, the factor $\exp\left(i\vec{k}\cdot\mathcal{r}\hat{r}\right)$ may be placed outside the integral over *X* to produce

$$\mathcal{F}\,[U(\vec{\mathbf{r}}_0)] \;=\; \gamma\rho \int_D dS \int_0^{h(r)} dz \exp\left(i\vec{k}\cdot r\hat{r}\right) \int_X \frac{\exp\left(-i|\vec{k}|w_0\cos\vartheta\right)}{(w_0^2+a^2)^{1/2}} w_0 dw_0 d\vartheta \tag{2.43}$$

The integral over ϑ is $2\pi J_0\left(|\vec{k}|w_0\right)$ (Eq. 10.9.2 of NIST, 2015). Thus,

$$\mathcal{F}\,[U(\vec{\mathbf{r}}_0)] \;=\; \gamma\rho \int_D dS \int_0^{h(r)} dz \exp\left(i\vec{k}\cdot r\hat{r}\right) \int_0^{\infty} \frac{2\pi J_0\left(|\vec{k}|w_0\right)}{(w_0^2+a^2)^{1/2}} w_0 dw_0 \tag{2.44}$$

The integral over w_0 is the Hankel transform of the function $2\pi(w_0^2 + a^2)^{-1/2}$ (Eq. 10.22.76 of NIST, 2015). From Table 12.2 of Bracewell (1965) or Téllez et. al. (1997), (Eq. (2.36) on p. 275), the result is

$$2\pi \int_0^{\infty} \frac{J_0\left(|\vec{k}|w_0\right)}{(w_0^2+a^2)^{1/2}} w_0 dw_0 = 2\pi \frac{\exp(-|\vec{k}|a)}{|\vec{k}|} \tag{2.45}$$

Putting this result into Eq. 2.40 produces the second equation on p. 449 of Parker (1972)

$$\mathcal{F}\,[U(\vec{\mathbf{r}}_0)] \;=\; \gamma\rho \int_D dS \int_0^{h(r\hat{r})} dz \left\{2\pi \exp\left(i\vec{k}\cdot r\hat{r} - |\vec{k}|(z_0 - z)\right)\right\} / |\vec{k}| \tag{2.46}$$

after resubstituting $z_0 - z$ for a.

2.3.3 Obtaining relation between $\mathcal{F}[\Delta\mathbf{g}]$ and $\mathcal{F}[\Delta\mathbf{h}]$

Parker (1972) $\mathcal{F}[U(\vec{\mathbf{r}}_0)] \;=\; \gamma\rho \int_D dS \exp\left(i\vec{k}\cdot r\hat{r} - |\vec{k}|z_0\right)\left\{\exp\left[|\vec{k}|h(r\hat{r})\right] - 1\right\}/|\vec{k}|^2$ (2.47)

integrates explicitly over z. Referring back to equation 2.7, the result is

Factoring out the upward continuation term, $\exp\left(-|\vec{k}|z_0\right)$, from the integral and using the Taylor series expansion of $\exp\left[|\vec{k}|h(r\hat{r})\right]$ produces Parker's result (his Eq. (2)) linking the potential to the topography as an infinite series of Fourier transforms.

$$\mathcal{F}[U(\vec{\mathbf{r}}_0)] \;=\; 2\pi\gamma\rho e^{-|\vec{k}|z_0} \sum_{n=1}^{\infty} \frac{|\vec{k}|^{n-2}}{n!} \mathcal{F}[h^n(\vec{r})] \tag{2.48}$$

The terrain correction is not the potential but rather the vertical attraction of the material. Since $\hat{z} \cdot \overrightarrow{\mathbf{r_0}} \;>\; \max\{h(\vec{r}_0)\}$, the gravitational potential obeys Laplace's equation (Section 2.12 of Hofmann-Wellenhof and Moritz, 2005), $\nabla^2 U = 0$. Under this condition, a general solution to Laplace's equation in Cartesian coordinates is of the form (Sec. 4.12 of Wyld, 1999; Sec. 13.2 of Boas, 2005)

$$U(\vec{\mathbf{r}}_\mathbf{0}) \;= \frac{1}{4\pi^2} \int d^2\, k \overline{U}\left(\vec{k}\right) e^{\left(-|\vec{k}|\hat{z}\cdot\vec{\mathbf{r}}_\mathbf{0} - i\vec{k}\cdot\vec{\mathbf{r}}_\mathbf{0}\right)} \tag{2.49}$$

where $\overline{U}\left(\vec{k}\right)$ is an unknown function for the moment. Comparison of this equation with Eq. 2.42 shows that

$$\mathcal{F}|U(\vec{r}_0)| = \overline{U}(\vec{k}) e^{-|\vec{k}|\hat{z}\cdot r_0} \tag{2.50}$$

By the definition of potential, the vertical attraction is $\Delta g = +\frac{\partial U}{\partial z}$. Using this equality in Eq. (2.46) produces

$$\mathcal{F}|\Delta g| = \; -\left|\vec{k}\right| \mathcal{F}|U| \tag{2.51}$$

Equation 2.51 is possible due to the Fourier Transform's derivative theorem. See appendix g for the proof as outlined by Bracewell (1965).

The desired generalized expression where the lower boundary of the layer is not flat but instead given by $z = g(\vec{\mathbf{r}})$ and where the density is free to vary with $\vec{\mathbf{r}}$ gives the result sought.

$$\mathcal{F}|\Delta g| = \; -2\pi\gamma e^{\left(-|\vec{k}|z_0\right)} \sum_{n=1}^{\infty} \frac{|\vec{k}|^{n-1}}{n!} \mathcal{F}[\rho(\vec{r})\{h^n(\vec{r}) - \; g^n(\vec{r})\}] \tag{2.52}$$

2.4 Gibbs Phenomenon

Given the assumption that some signal f(t) is continuous, the ability for a standard FT to represent its frequency content is difficult if time-localization is needed (Daubechies, 1992). Time-localization is possible through windowing, heretofore called the windowed Fourier transform (Daubechies, 1992). However, the wavelet transform also provides a time-frequency description but does so with the increased zoom capability for "short-lived high frequency phenomena, such as transient signals" (Daubechies, 1992). The advantage of the wavelet transform over the windowed FT results from its ability to be manipulated to cover different frequency ranges and relocate its time localization center (Daubechies, 1992). As an example, the MHW is well localized in both time (or space) and frequency (Daubechies, 1992).

The periodicity of the sine and cosine functions results in difficulty when attempting to accurately represent discontinuous functions such as step functions, saw tooth functions and square functions as a Fourier series (Rasmussen 1993). Removal of the highest frequency contributions results in a filtered function that is unable to uniformly converge at any interval which contains a discontinuity, overshooting between 0-17% in the vicinity of said discontinuity (Rasmussen 1993). This is the Gibb's phenomenon, which was rediscovered by J. Willard Gibbs and discussed in a letter to the journal Nature in 1898 (Gibbs 1898). The step function was used as an example to demonstrate this phenomenon. As the number of coefficient terms increased, the Fast Fourier Transform (FFT) more closely approximated the step function but nonetheless, continued to overshoot. See Figure 2.4 below.

The occurrence of this phenomenon is critical in the determination of the number of coefficients required to recreate a signal (Bracewell 1965). Figure 2.5 thus demonstrates how many coefficient terms are required to effectively diminish the Gibbs phenomenon. For the case of the step function, a minimum of 226 coefficients was required. The calculation was made by taking the square root of the sum of the coefficients a_n and b_n. The results were plotted and a visual inspection was made to determine when Gibbs induced error was no longer visible.

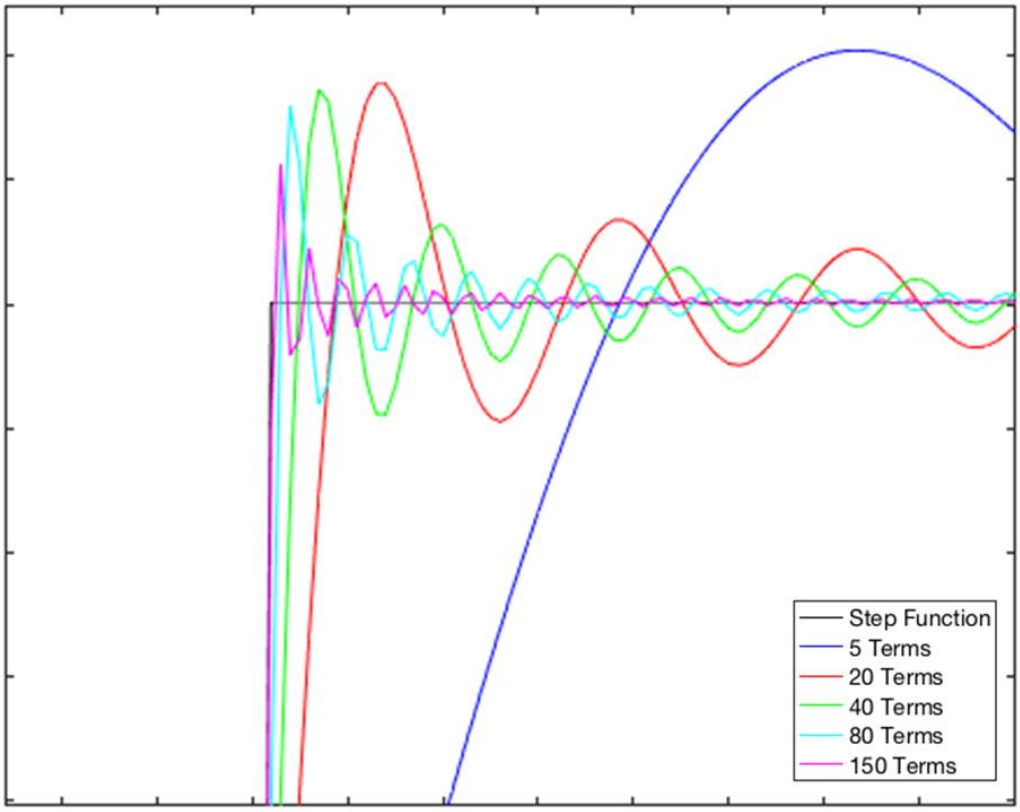

Figure 2.4 Gibbs Phenomenon of a Step function.

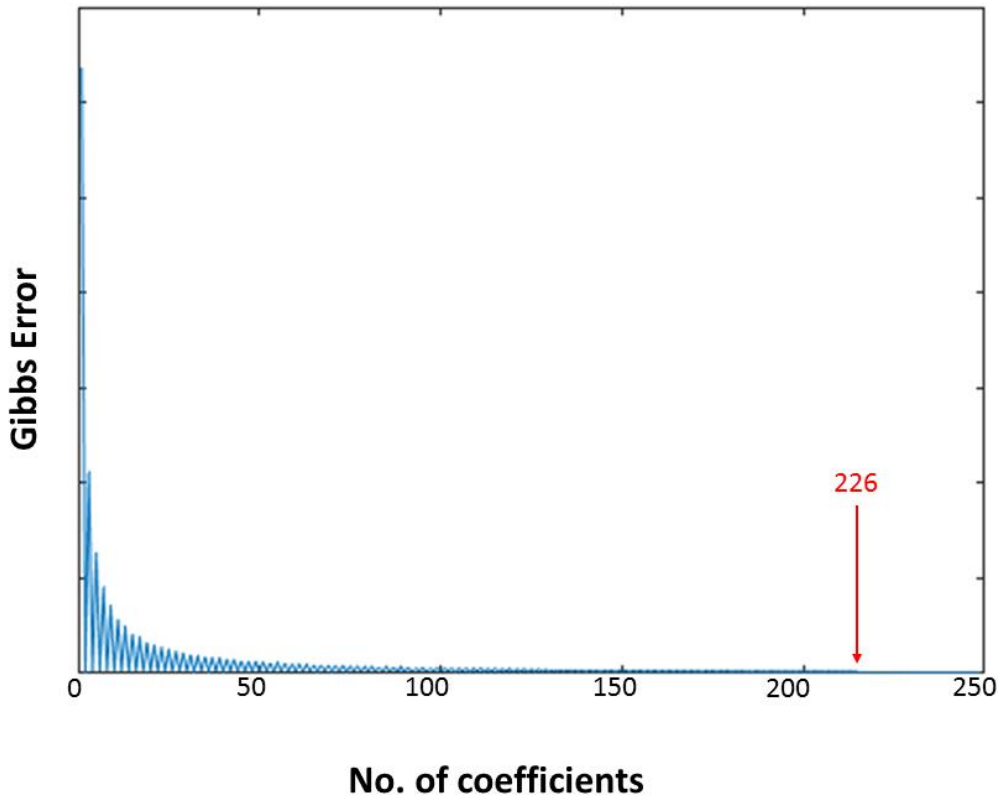

Figure 2.5 Gibbs Error vs. No. of Coefficients.

Note. Relates how many coefficients are needed to minimize Gibbs phenomenon issues.

This phenomenon also exists for wavelets (Rasmussen 1993). According to Rasmussen, however, wavelets should not overshoot the FFT; and, a wavelet may be chosen such that overshoot will not occur (the advantage of time and frequency localization by wavelets for short-lived high frequency phenomena). Figure 2.6 gives a comparison of various wavelets against the FFT for a step function. The step function was poorly reproduced by the FFT with all terms (blue line). The Daubechies wavelets performed best, although, the MHW produced a near perfect replication of the step function as well (green line). As can be seen in the figure inset, however, the MHW

smoothed the corner of the step function. It may be determined at least for this basic function, that the MHW dramatically outperformed the FFT at reproducing a function at a discontinuity. This could be of significant importance when attempting to predict bathymetric features with sharp inclinations, such as ridges, fracture zones and steep sea mounts.

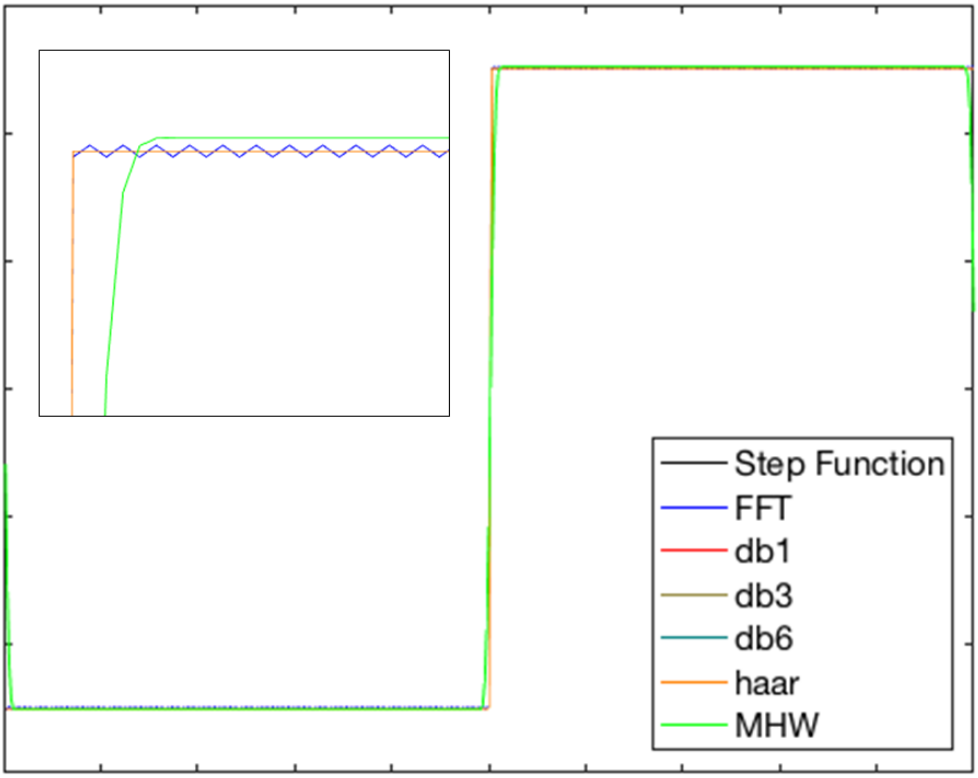

Figure 2.6 Gibbs Phenomenon of a step function with respect to the FFT, selected discrete wavelets and MHW.

Another example of a signal with discontinuities is the saw tooth function. Figure 2.7 demonstrates the superiority of wavelet transforms over the FFT, however utilizing the db6 wavelet developed by Ingrid Daubechies.

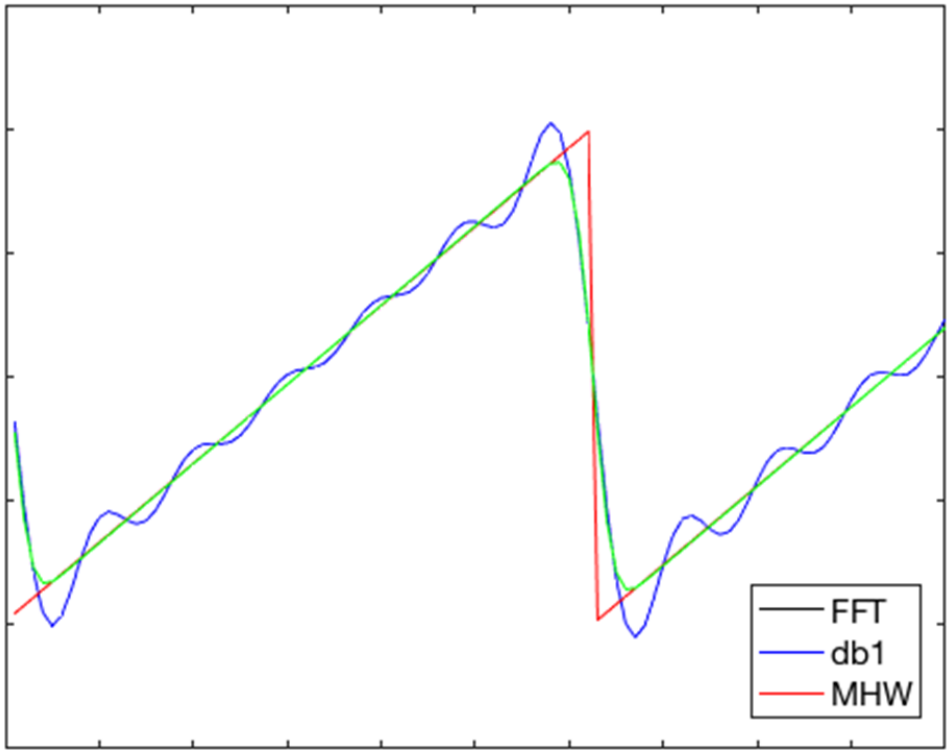

Figure 2.7 Gibbs Phenomenon of the FFT and db6 wavelet.

It is clear in Figure 2.7 that the analyzing wavelets outperformed the FFT at reconstructing the saw-tooth function and that overshoot by the FFT is clearly apparent at the discontinuities.

CHAPTER III - METHODS

The following methods will be utilized for this study.

3.1 Fourier Transforms

The Fourier Transform is a linear mathematical method used to solve linear problems (Bracewell, 1965). If there is some function f(x), then it can be mapped from the time/spatial domain to the frequency/wavenumber domain and then back again (David M. Glover 2011). That is, using an infinite series of sine and cosine pairs multiplied by a function containing the sine and cosine coefficients, a function can be transformed from one domain to the other (David M. Glover 2011). Expressing the sine and cosine pairs exponentially, the FT of some function f(x) is expressed as (Bracewell 1965):

$$F(s) = \int_{-\infty}^{\infty} f(x) e^{-i2\pi xs}\, dx \tag{3.1}$$

However, if the integral of |f(x)| exists from –infinity to infinity and any discontinuities in f(x) are finite, then the Fourier Theorem states that (Bracewell 1965):

$$f(x) = \int_{-\infty}^{\infty} F(s)\, e^{i2\pi xs} ds \tag{3.2}$$

Thus, under the aforementioned conditions, these transforms are cyclical, otherwise known as the Fourier Theorem.

Proof of this theorem, below, is from (Papoulis 1962). Beginning with the Fundamental Theorem:

$$f(t) = \frac{1}{2\pi} \int_{-\infty}^{\infty} F(\omega)\, e^{i\omega t} d\omega, \tag{3.3}$$

where the transform of the function f(t) is F(ω) defined as:

$$F(\omega) = \int_{-\infty}^{\infty} f(t)\, e^{-i\omega t} dt \tag{3.4}$$

Substitution of the equation for F(ω) into the Fundamental Theorem yields:

$$f(t) = \frac{1}{2\pi}\int_{-\infty}^{\infty} e^{i\omega t}\, d\omega \int_{-\infty}^{\infty} f(t)\, e^{-i\omega t} dt \tag{3.5}$$

$$\frac{1}{2\pi}\int_{-\infty}^{\infty} e^{i\omega t}\, d\omega = \delta(t) \tag{3.6}$$

$$\int_{-\infty}^{\infty} \varphi(x)\, \delta(t-x) dx = \varphi(t) \tag{3.7}$$

After rearrangement and application of the first identity, we arrive at:

$$f(t) = \frac{1}{2\pi}\int_{-\infty}^{\infty} F(\omega) e^{i\omega t}\, d\omega = \frac{1}{2\pi}\int_{-\infty}^{\infty} f(x)\, dx \int_{-\infty}^{\infty} e^{i\omega(t-x)}\, d\omega = \int_{-\infty}^{\infty} f(x)\delta(t-x)\, dx \tag{3.8}$$

Recall, however the second identity listed. Thus,

$$f(t) = \frac{1}{2\pi}\int_{-\infty}^{\infty} F(\omega) e^{i\omega t}\, d\omega = \frac{1}{2\pi}\int_{-\infty}^{\infty} f(x)\, dx \int_{-\infty}^{\infty} e^{i\omega(t-x)}\, d\omega = \int_{-\infty}^{\infty} f(x)\delta(t-x)\, dx = f(t) \tag{3.9}$$

The following two theorems will also be of particular importance to this study:

1. The Addition Theorem states that if two functions, f(x) and g(x) have FTs F(s) and G(s), respectively, then the sum of the two functions has a FT equal to the sum of their respective transforms (Bracewell 1965).
2. The Derivative Theorem states that for some function f(x) whose transform is F(s), then the transform of its derivative, f ’(x) is i2πsF(s) (Bracewell 1965).

These two theorems, whose proofs are available in Bracewell’s text, will prove invaluable towards calculating the FT of gravitational potentials.

3.2 Wavelet Transforms

Due to the time-independent frequency content of the sine and cosine basis functions that comprise the FT, the analysis of the signal is purely in the frequency domain. However, for the windowed FT and Wavelet Transform (WT), the objective is

to conduct an analysis of both time and frequency (Starck 2015). Starck, 2015 notes the introduction of the windowed FT, which is a short-time FT (STFT) by (Gabor, 1946) in his 1946 paper, "The Theory of Communications". This method allows for the analysis of non-stationary signals through the use of a sliding Gaussian window yielding information on both time and frequency domains (Starck 2015). From Starck, 2015, begin with the formula for the STFT

$$STFT(\tau, \omega) = \int_{-\infty}^{\infty} s(t)\, g(t-\tau) e^{-j\omega t} dt \tag{3.10}$$

A new basis is considered

$$k_{\tau,\omega}(t) = g(t-\tau) e^{-j\omega t} \tag{3.11}$$

and rewritten with a new window size, a, which will be inversely proportional to the frequency ω. Further, τ is replaced by a positional parameter b resulting in the continuous wavelet transform (CWT)

$$k_{b,a}(t) = \frac{1}{\sqrt{a}} \psi^* \left(\frac{t-b}{a}\right) \tag{3.12}$$

where, ψ^* is the complex conjugate of ψ. For the CWT, the basis functions are scaled forms of the mother wavelet ψ (Starck 2015). Taking the second derivative of the Gaussian (DOG) function, though, results in the Ricker Wavelet, otherwise known as the Mexican Hat Wavelet (MHW) due to its sombrero like shape (Daubechies, 1992; Ryan, 1994). Per Daubechies, 1992, if the second derivative of the Gaussian is normalized such that L^2 norm is 1, then the formula of the MHW is:

$$\psi(x) = \frac{2}{\sqrt{3}} \pi^{-1/4} (1 - x^2) e^{-x^2/2} \tag{3.13}$$

Starck, 2015 provides a simplified version of this formula as

$$\psi(x) = (1 - x^2) e^{-x^2/2} \tag{3.14}$$

The MHWs are zero-phase that consist of a central peak with two smaller lobes on either side; and, they are uniquely specified by a singular frequency parameter, which is its peak frequency (Ryan, 1994). Like the FT, the CWT also has an inverse that can be recovered using the formula below (Starck 2015)

$$f(x) = \frac{1}{C_\chi}\int_0^{+\infty}\int_{-\infty}^{+\infty}\frac{1}{\sqrt{a}}W(a,b)\chi\left(\frac{x-b}{a}\right)\frac{da.db}{a^2}, \tag{3.15}$$

where

$$C_\chi\int_0^{+\infty}\frac{\widehat{\psi}^*(\nu)\widehat{\chi}(\nu)}{\nu}d\nu = \int_{-\infty}^{0}\frac{\widehat{\psi}^*(\nu)\widehat{\chi}(\nu)}{\nu} \tag{3.16}$$

The admissibility condition, however, for reconstruction is that C_χ must be finite, which means that the mean of the wavelet function is zero (Starck 2015). Proof of this cyclical property will not be addressed here.

3.3 Power Spectral Density

Here, the term power refers to the measure of variance; and, power spectral density (PSD), also referred to as the power spectrum, is the measure of variance distribution with respect to frequency, wavenumber or scale that is contained within the signal in question (David M. Glover 2011). Through the extraction of variance in a signal at specific frequencies or wavenumbers, information regarding the placement of peaks and the overall shape of the spectrum can help a researcher determine the nature of the signal being studied. PSD can be defined as (Bracewell 1965)

$$\int_{-\infty}^{\infty}|F(s)|^2 ds \tag{3.17}$$

Also, per Parseval's Theorem, regardless of how total power is defined, total power in the frequency/wavenumber domain must equal total power in the time/spatial domain (Starck 2015).

$$\int_{-\infty}^{\infty}|F(s)|^2 ds = \int_{-\infty}^{\infty}|Y(x)|^2 dx \quad (3.18)$$

Similarly, the same methodology applies with wavelets, where its PSD may be defined as

$$\int_{-\infty}^{\infty}|\psi(x)|^2 dx \quad (3.19)$$

3.4 Histogram

The frequency-of-occurrence diagram or histogram is a type of graphical plot dealing with the concepts of sampling and probability (Thomson 1998). For a given set of sample values, a histogram gives information on the frequency of occurrence of a particular value (Thomson 1998). Here, the area distribution of depth references to hypsometry, where the calculated curve may be used as a base for describing a region's morphology and geological evolution (Weatherall 2015).

3.5 Root Mean Square Error

The root mean square error (RMSE) is defined as

$$RMSE = \sqrt{\frac{\sum_{i=1}^{n}(x_{obs\,i} - x_{model\,i})^2}{n}} \quad (3.20)$$

This calculation will give the difference in meters between the original bathymetric and reconstructed signals which will allow for the comparison between the FFT and sparser basis functions.

The following MATLAB functions were used for the computation of the FFT and wavelets:

- fft/ifft, where ifft is the inverse Fast Fourier Transform.
- cwtft/icwtft: Continuous Wavelet Fourier Transform and icwtft is its inverse. Note that the cwtft is the required command if an inverse transform is required, per Simulink documentation with the reason given

is that computation of continuous wavelets and their inverses are too computationally demanding via convolution. Therefore the computations are made in the Fourier domain for speed. The non-Fourier method command for cwt's is "cwt." An inverse cannot be computed for the cwt utilizing convolutions in MATLAB.

- dwt/idwt, where dwt is the Discrete Wavelet Transform and idwt is the inverse Discrete Wavelet Transform.

CHAPTER IV – RESULTS

4.1 Initial RMS Error Test

The first test was the comparison of RMSE for a few different wavelet functions with the FT. The first test utilized a simple function, in this case the step function. MATLAB provided a built-in function to create this: "heaviside.m." Also, a small data set was taken from the Southern East Pacific Rise, utilizing only one longitudinal value (-108 West) and moving across latitudinally. The MATLAB "fft" function will utilize all coefficients. As such, reconstruction of the original bathymetric signal utilizing the "fft" and "ifft" functions result in a near identical signal reconstruction. Therefore, utilizing the example located in the MATLAB "fft" documentation and the definition of the Fourier series as a sum of sines and cosines, the signal was able to be constructed term-by-term with an increasing number of coefficients. From Duffy, 1998

$$f(x) = \frac{a_0}{2} + \sum_{n=1}^{\infty} a_n cos\left(\frac{\pi n x}{L}\right) + b_n sin\left(\frac{\pi n x}{L}\right) \quad (4.1)$$

where the DC term a_0, a_n and b_n are the Fourier coefficients. These coefficients were calculated directly utilizing the "fft" MATLAB function. Due to the locality of wavelets, a direct comparison of RMSE between them and the FT is not possible unless the FT is windowed due to the global nature of the fft. MATLAB provided the "hamming" function to accomplish this. Afterwards, the RMSE of the original and reconstructed signals was calculated for the FT, MHW and the first six Daubechies wavelets. Their RMSE was calculated and then were plotted alongside each other for comparison.

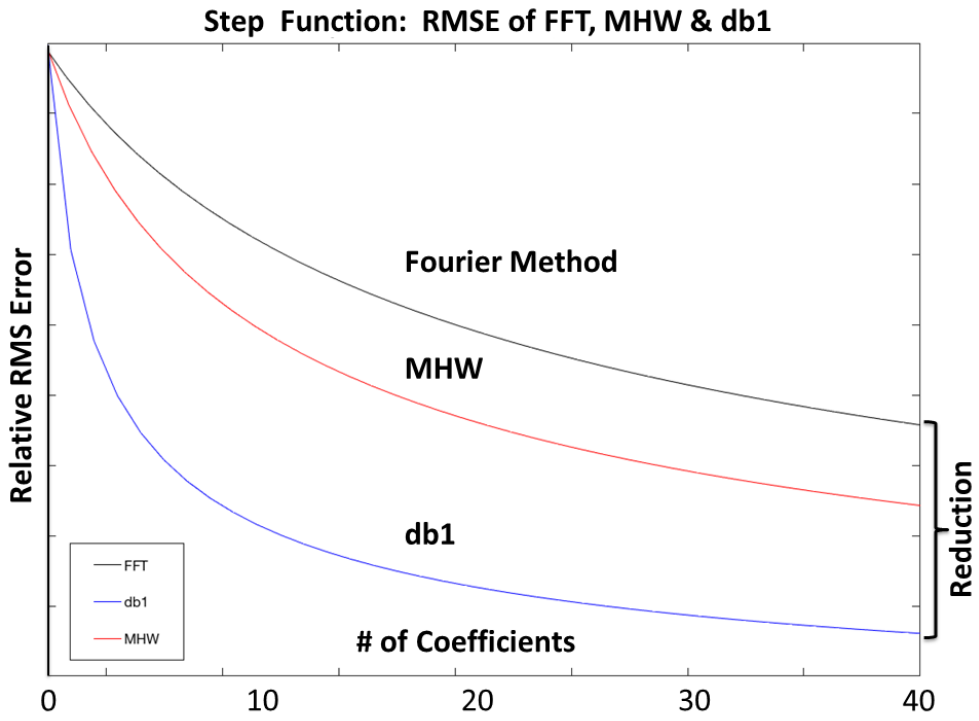

Figure 4.1 RMSE of the FT, MHW and DB1 wavelets.

Figure 4.1 depicts only three transforms: the Fourier, MHW and db1 wavelet. The plot demonstrates that both the continuous and discrete wavelets outperformed the FT, resulting in a lower RMSE while utilizing fewer coefficients to compute the signal reconstruction. Notably, the db1 wavelet revealed a dramatic drop in RMSE with only a slight increase in the number of coefficients. A subset of the Southern East Pacific Rise (SEPR) sample data set was tested next. Figure 4.2 similarly demonstrated the effectiveness of wavelets at producing a lower RMSE with fewer coefficients, which translates into a more economical reconstruction of the signal. In figure 4.2, only the FT and Daubechies wavelets (1-6) are shown.

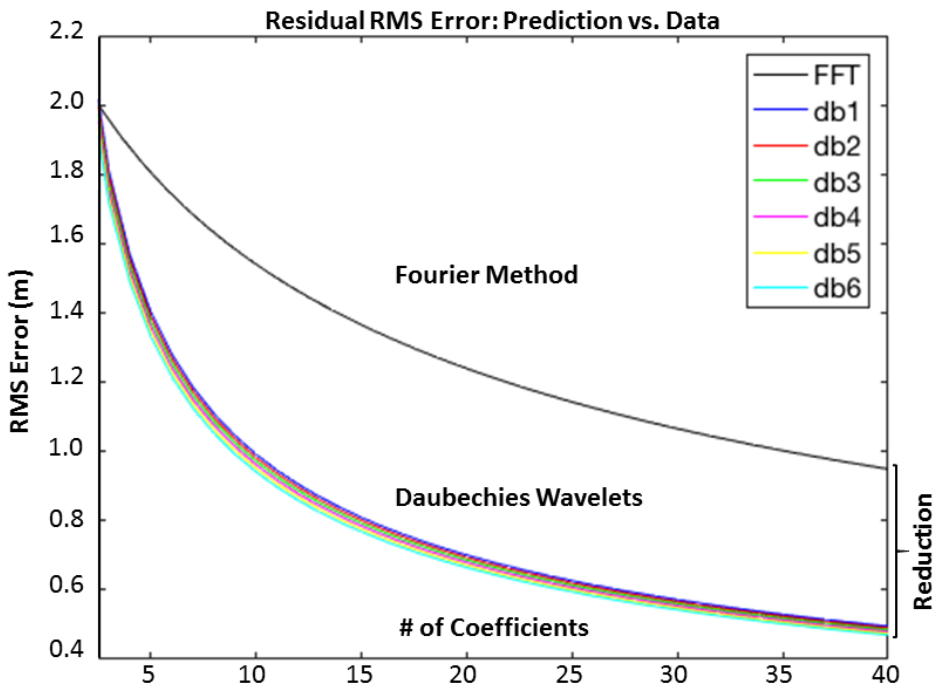

Figure 4.2 FFT Reconstruction of a Step-Function

Note: This shows the FFT reconstruction of a step function compared to each of the six mentioned discrete wavelet transforms with respect to RMSE.

The reconstruction of the signal with only fifty terms demonstrates the inefficiency of the FT and its tendency to overshoot. This is the Gibbs phenomenon. A few selected discrete wavelets utilized the same number of coefficients and did not have the overshoot issues of the FT. Figure 4.3, below, depicts the reconstruction of the step function.

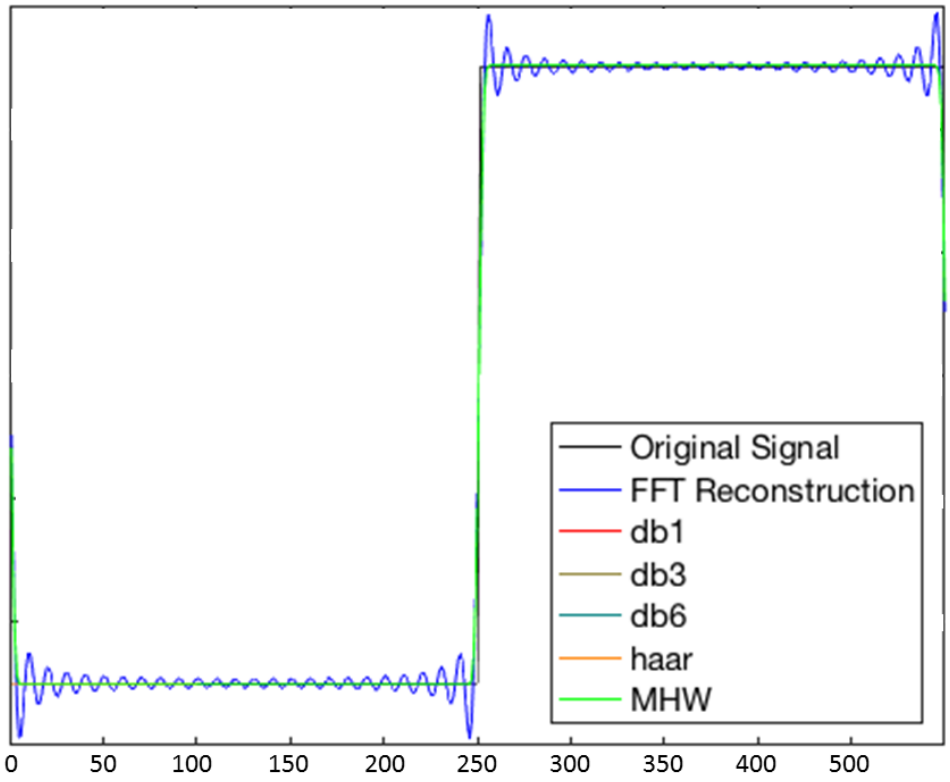

Figure 4.3 Reconstruction of a Step Function via the FFT and Continuous and Discrete Wavelets.

Note: This shows the reconstruction of the step function utilizing 50 coefficients for the FT, MHW, the Haar wavelet and three Daubechies wavelets.

A 1D-bathymetric signal was tested utilizing the same methodology. Whereas the Gibbs phenomenon is not easily discernible for this particular case, the comparison of RMSE gives insight into the efficiency of wavelets over the FT. Figure 4.4 gives a comparison of the MHW and the FT. Although, there is little difference in their evaluated RMSE, the MHW slightly outperformed the FT. The reason for the MHW not having a significant advantage in recreating the signal could be attributed to this particular wavelet's smoothing function. It is possible that too much detail is removed during the

reconstruction process. However, the discrete wavelet cases did demonstrate a clear advantage over the FT (see figure 4.5).

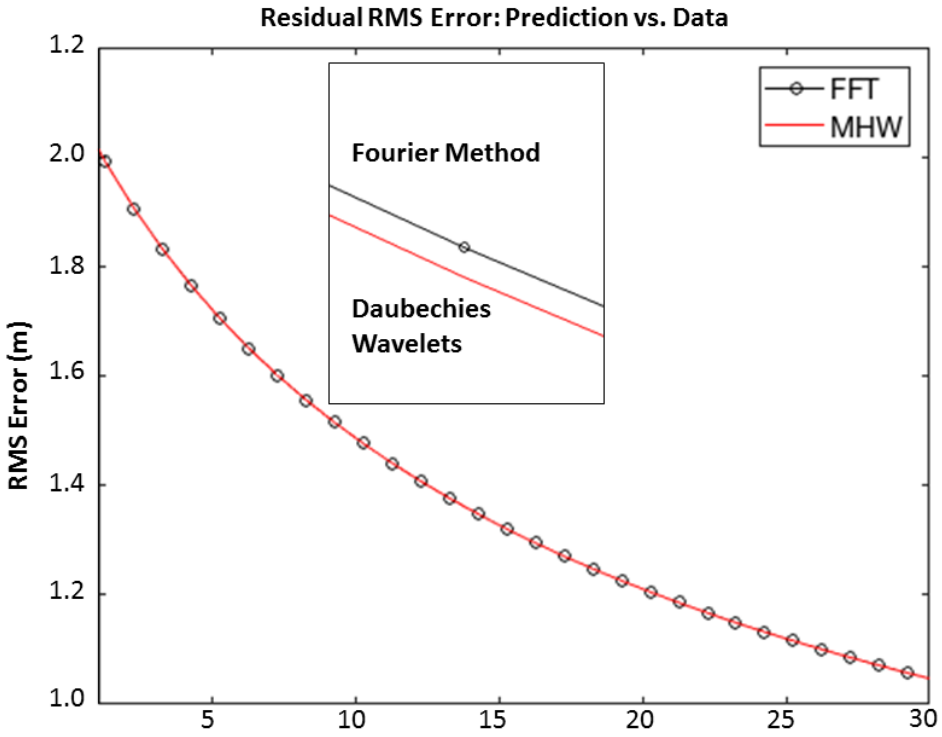

Figure 4.4 1D Bathymetric Signal, MHW vs. FFT.

Note: This plot demonstrates the slight advantage of the MHW over the FT in a 1D bathymetric signal reconstruction through comparison of their RMSE.

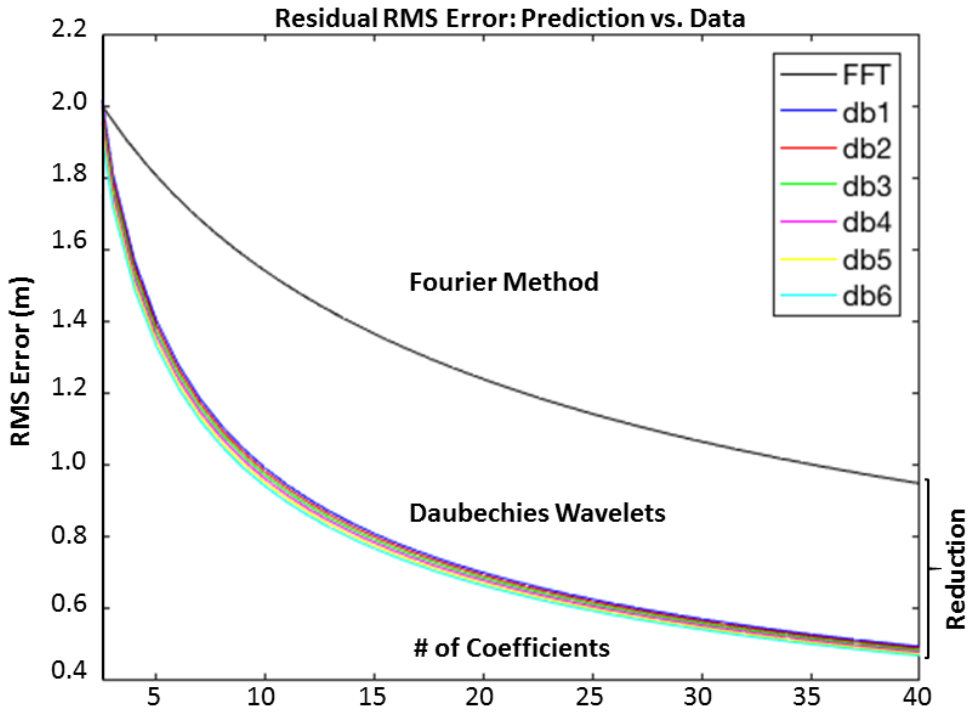

Figure 4.5 1D Bathymetric Signal, DB Wavelets vs. FFT

Note: This demonstrates the clear advantage of six selected Daubechies wavelets over the FT in a 1D bathymetric signal reconstruction through comparison of their RMSE.

4.2 Noise

As it makes sense that noise will invariably be included in any raw data set, a simple de-noising test was conducted to determine which transform, FFT, CWT and Discrete Wavelet Transform (DWT) would perform best at removing noise to achieve a better representation of the signal. The aforementioned SEPR was utilized. Random noise was added until the original signal was sufficiently hidden. The signal was then transformed and then transformed back via the respective inverse transforms. The FFT reconstruction did not remove any discernable noise. Convolutions were not used here, though will be addressed later in the dissertation. However, continuous wavelets are such

that their nature has a built in filter. Figure 4.6 shows that the FFT reconstruction is nearly identical to the noisy signal as all coefficient terms were utilized.

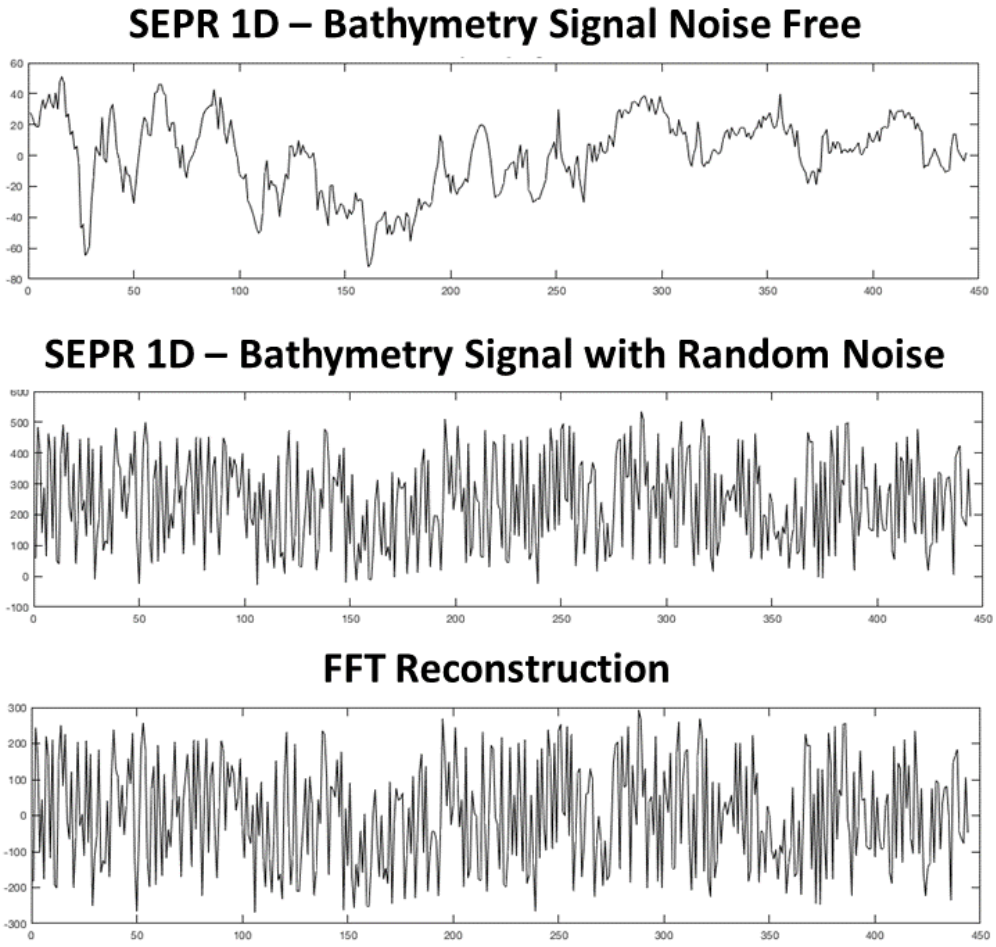

Figure 4.6 Noise removal of a signal via FFT filtering.

The MHW, however, due to its smoothing function was able to remove much of the noise while losing only a minimal amount of detail of the actual noise free signal. This method, then, is less of true filter and more of smoothing function. See Figure 4.7 below.

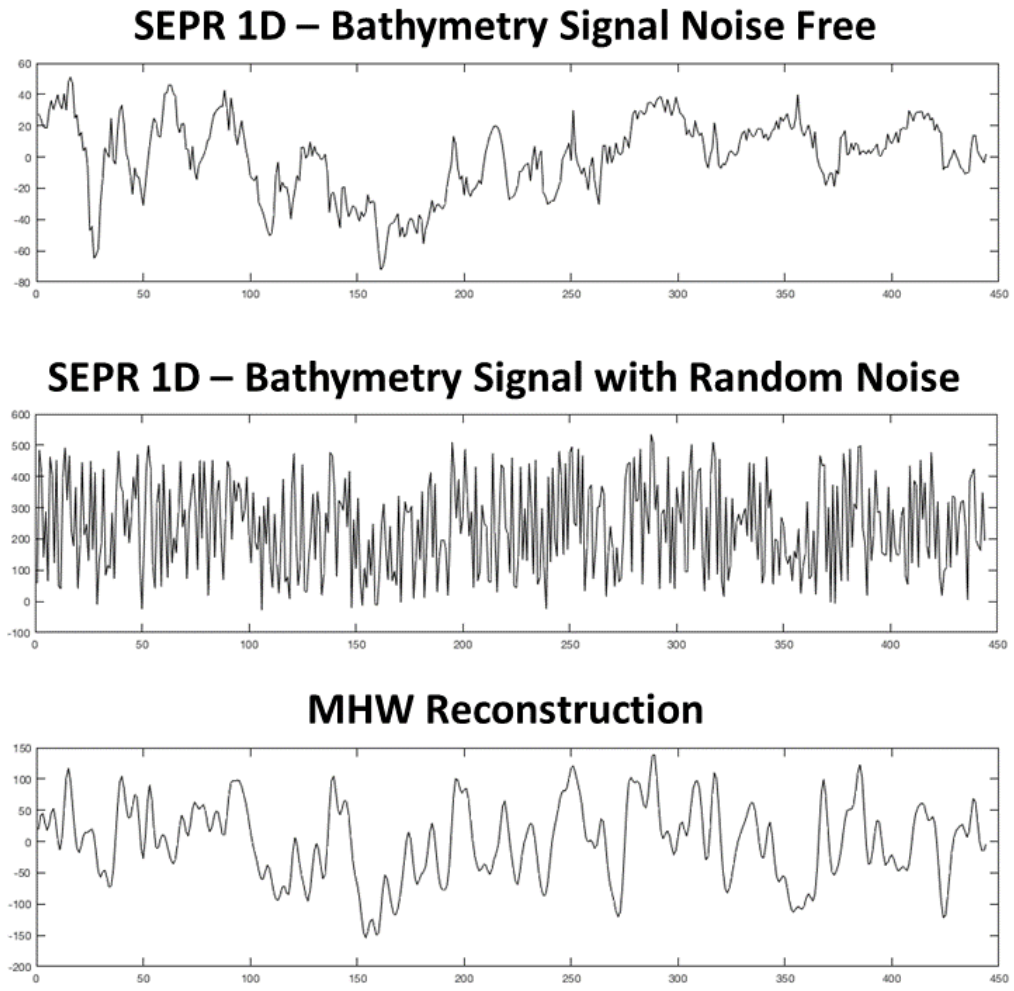

Figure 4.7 Noise removal via MHW filtering.

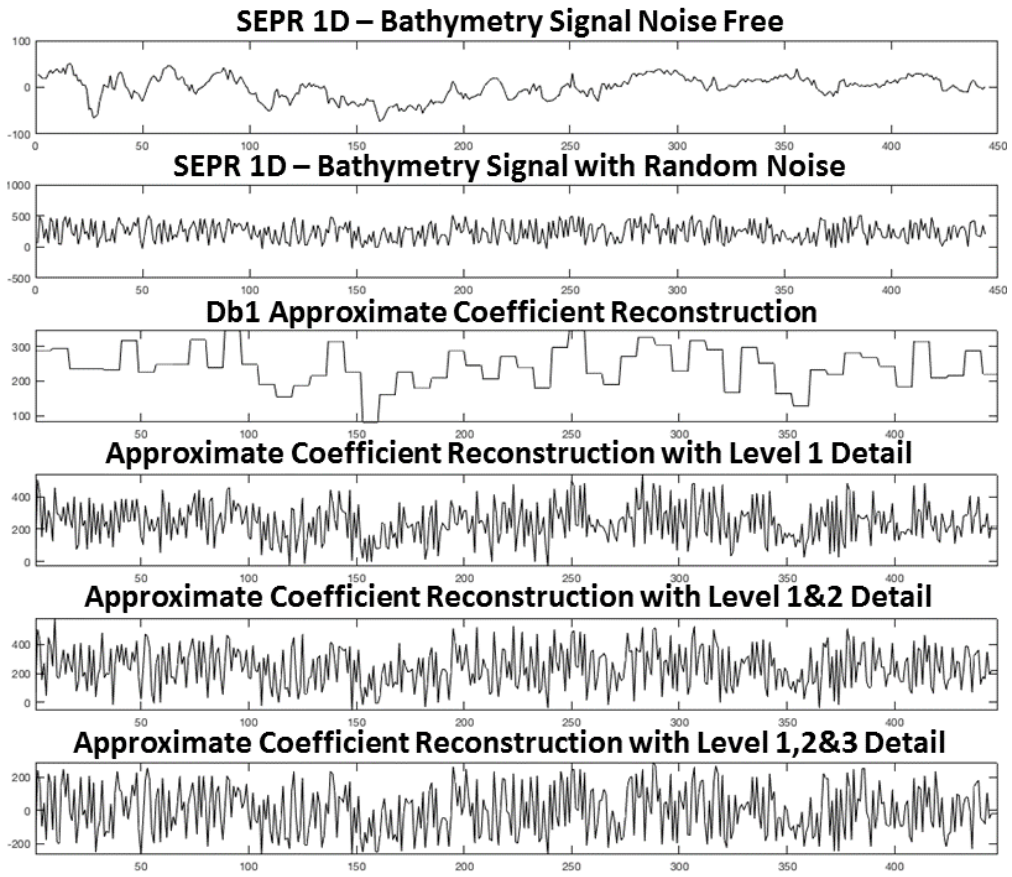

Figure 4.8 Depiction of the DWT to remove and add noise from and to a signal.

In order to better demonstrate the ability of wavelets to remove noise from a signal, a simple square wave function is used as an example. As can be seen in figure 4.9, both a continuous wavelet (MHW) and a discrete wavelet (db1) were able to remove noise while the FFT did not. Although it is not shown here, discrete wavelets do have a superior method of noise removal via a tree-like method where one can add as much detail coefficients to the absolute coefficients as desired. This capability is well documented function in MATLAB.

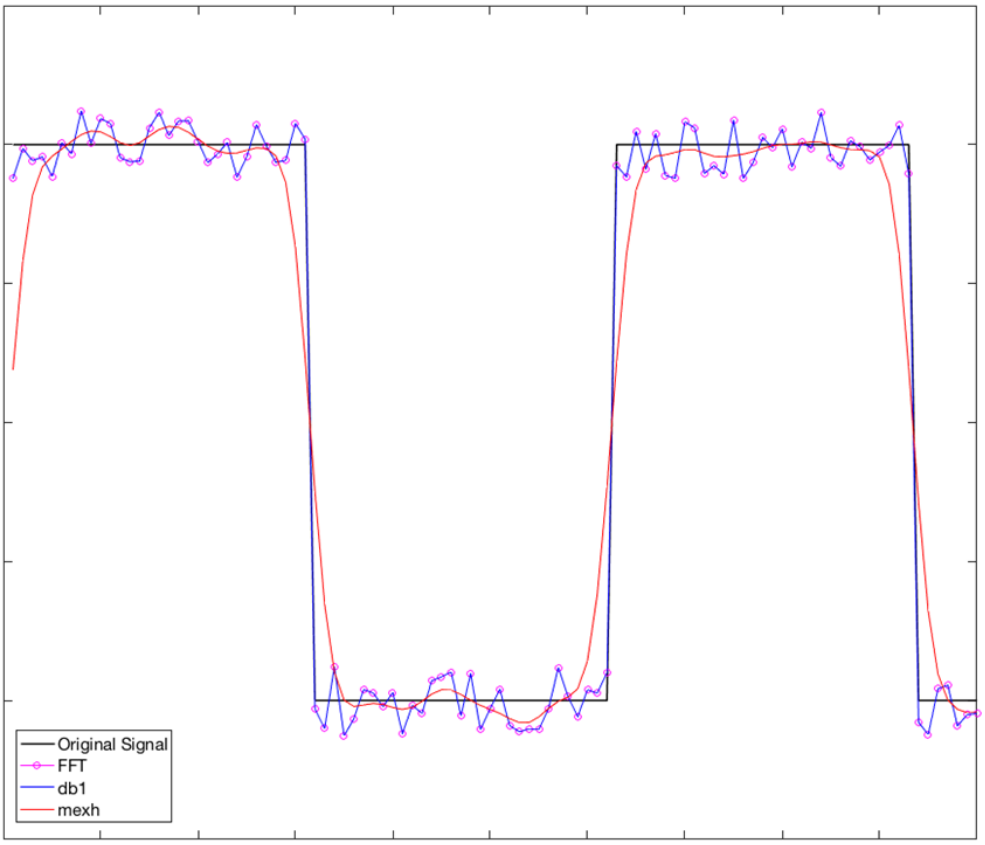

Figure 4.9 Noise Removal for a Step Function by the FFT, db1 and MHW

4.3 Feasibility of an Analytical Solution of the CWT of the Gravitational Potential

Prior to testing the applicability of the CWT in bathymetric prediction from satellite altimetry outright, an analytical solution in accordance with the methods of Parker was first considered. However, due to the extra complexity of the CWT in comparison to the FT, a simple test case was considered: the aforementioned potential of the monopole.

Recall:

$$U(P) = \frac{\gamma\mu}{x} \tag{4.2}$$

The MHW (1D) will be applied

$$\psi(x) = \int_{-\infty}^{\infty} \frac{2}{\sqrt{3s}\pi^{1/4}} \left(1 - \frac{x^2}{s^2}\right) e^{-x^2/2s^2} \tag{4.3}$$

Taking the CWT (MHW) of the monopole potential results in

$$\psi[U(x)] = \int_{-\infty}^{\infty} \frac{\gamma\mu}{x} \frac{2}{\sqrt{3s}\pi^{1/4}} \left(1 - \frac{x^2}{s^2}\right) e^{-x^2/2s^2} \tag{4.4}$$

After distribution and removal of constants outside the transform, this integral may be broken up into two parts

$$\psi[U(x)] = \frac{2\gamma\mu}{\sqrt{3s}\pi^{1/4}} \left[\int_{-\infty}^{\infty} \frac{e^{-x^2/2s^2}}{x} dx - \int_{-\infty}^{\infty} \frac{x^2 e^{-x^2/2s^2}}{x} dx \right] \tag{4.5}$$

After integration by parts, the second integral can be shown to converge to zero. The first integral, though, results in an Exponential integral (Ei) function, thus the CWT of the monopole potential results in the following

$$\psi[U(x)] = \frac{\gamma\mu}{\sqrt{3s}\pi^{1/4}} \left(Ei\left(\frac{-sx^2}{2}\right)\right) \tag{4.6}$$

as computed in Mathematica. Although, this is a closed form solution, it is not necessarily useful. As such, another attempt was made at solving the problem using the methods of Argueso et al., (2006). This method calls for the FT of the MHW. Their procedure for this calculation is outlined below in detail.

The FT of the MHW is set forth as

$$\mathcal{F}[\psi_n(x)] = \widehat{\psi_n}(k) = \int_0^{\infty} dx\, x\, J_0(kx)\psi_n(x), \tag{4.7}$$

where $\psi_n(x) = \frac{(-1)^n}{2^n n!}\Delta_n\varphi(x)$, $\varphi(x) = \frac{e^{-x^2/2}}{2\pi}$ and J_0 is the Bessel function.

Note: $\varphi(x) = \frac{e^{-x^2/2}}{2\pi}$ is the 2-D Gaussian.

We now have

$$\mathcal{F}[\psi_n(x)] = \int_0^\infty dx\, x\, J_0(kx)\, \frac{(-1)^n}{2^n n!}\, \Delta_n \frac{e^{-x^2/2}}{2\pi}, \tag{4.8}$$

where Δ_n is the derivative function. For the R^2 case where n=1 (standard MHW), Δ_n becomes the second derivative which applied to the 2-D Gaussian results in

$$\frac{d^2}{dx^2}\left[e^{-x^2/2}\right] = x^2 e^{-x^2/2} - e^{-x^2/2} \tag{4.9}$$

Thus,

$$\mathcal{F}[\psi_1(x)] = \int_0^\infty dx\, x\, J_0(kx)\, \frac{-1}{2}\left(\frac{x^2 e^{-x^2/2} - e^{-x^2/2}}{2\pi}\right) \tag{4.10}$$

Removing the constants to outside of the integral and further separating into two integrals gives

$$\mathcal{F}[\psi_1(x)] = \frac{-1}{4\pi}\left[\int_0^\infty dx\, x\, J_0(kx)\left(x^2 e^{-x^2/2}\right) - \int_0^\infty dx\, x\, J_0(kx)\left(e^{-x^2/2}\right)\right] \tag{4.11}$$

Applying the gravitational potential of the monopole results in

$$\mathcal{F}[\psi_1(x)] = \frac{-1}{4\pi}\left[\int_0^\infty dx\, x\, J_0(kx)\left(x\, e^{-x^2/2}\right) - \int_0^\infty dx\, x\, J_0(kx)\left(\frac{e^{-x^2/2}}{x}\right)\right] \tag{4.12}$$

Utilizing, *Tables of Integral Transforms* (Bateman, 1954) a solution to the above integrals was found. From page 9 of volume 2

$$x^{2\mu - 3/2} e^{-x^2/2}\ Re\ \mu > 0 \tag{4.13}$$

Per the table, the solutions are Hankel transforms; and, for the last integral setting μ = 1 gives the result

$$\Gamma(1) y^{1/2}\ {}_1F_1\left(1; 1; -\frac{1}{2}y^2\right), y > 0 \tag{4.14}$$

For the first integral setting $\mu = 2$ gives the result

$$2\,\Gamma(2)y^{1/2}\,{}_1F_1\left(2;1;-\frac{1}{2}y^2\right), y > 0 \tag{4.15}$$

Thus, application of the Fourier transformed standard MHW to the potential of a monopole resulted in

$$\left[\frac{-1}{2\pi}\,\Gamma(2)y^{1/2}\,{}_1F_1\left(2;1;-\frac{1}{2}y^2\right)\right]-\left[\frac{-1}{4\pi}\Gamma(1)y^{1/2}\,{}_1F_1\left(1;1;-\frac{1}{2}y^2\right)\right], y > 0 \tag{4.16}$$

4.4 Application of the FT(MHW) to the Gravitational Potential

Robert Parker's 1972 paper, "The Rapid Calculation of Potential Anomalies," demonstrated the effectiveness of Fourier Transforms (FT) to compute gravitational or magnetic potential anomalies caused by uneven, non-uniform layers of material, in particular where large data sets are available. Parker, applied the FT to the Earth's gravitational potential and calculated an analytical solution. The importance of this finding is the relationship of the gravitational potential anomaly and sea-floor topography. As outlined by the 1997 Sandwell and Smith paper, "Marine Gravity Anomaly from Geosat and ERS 1 Satellite Altimetry," a six-step process demonstrated how satellite altimetry measurements of marine geoid height is inverted into seafloor topography. The FT is not without issue, though. FT basis functions are local in wavenumber but not in space. Seafloor features, however, exhibit spatial locality, meaning that that the amplitude goes to zero away from the object. Thus, the FT of seafloor topography will have a wide spectrum of wavenumber components, requiring computation of many Fourier coefficients, because the components have constant

amplitude from $-\infty$ to $+\infty$. Small changes in the transform will produce changes everywhere in the spatial domain (Vidakovic & Mueller, 1991). As a result, the root-mean-square (RMS) error in the transform will eventually reach a lower limit that is pragmatically unreducible without the use of a different transformation method. Finally, the Gibb's phenomenon is well known to be an issue with the FT, whereas with wavelets, Gibbs is always lower than that of the FT; and, a wavelet can be selected such that this phenomenon does not occur (Rasmussen, 1993). The aim of this paper is to investigate the feasibility of sparser base functions, specifically the Mexican Hat Wavelet (MHW) or Ricker wavelet.

Exhibiting locality in both space and time (Vidakovic & Mueller, 1991), the concept of wavelets derived from the attempt to localize the FT through windowing (Daubechies, 1992). Further, many different function classes are more compactly represented by wavelets than FTs, such as functions with discontinuities and sharp spikes (Vidakovic & Mueller, 1991). Rather than simply apply numerical techniques such as from the MATLAB wavelet toolbox, an attempt to analytically model the Wavelet Transform (WT) of the gravitational potential is made. A few considerations were made to determine which wavelet family should be applied. First, the occurrence of seamounts throughout the ocean was considered due to their localized behavior, e.g. steep incline. The MHW name comes from its resemblance to a Mexican sombrero which is very similar in shape to a seamount. Second, as the likelihood that a pure analytical solution of the wavelet approach is low, other calculation techniques had to be considered. Argueso et al, (2006), were able to use the MHW family to determine point source detection in cosmic microwave background radiation. To do this, they took the FT of the

MHW. This method allowed for an analytical solution due to the relatively simpler FT. It was possible to do this, because the MHW is circularly symmetric. A 2-D FT of a function with circular symmetry will result in a Hankel Transform of order zero (Piessens, 2000). As many of these solutions are known, this method is a sound starting point for a solution. For these reasons, this paper examines the MHW over non-circularly symmetric wavelets such as the Haar and Daubechies family.

As with Parker, (1972), the gravitational potential at some position $\mathbf{r}_0$ due to a layer is defined as:

$$U(\vec{\mathbf{r}}_0) = \gamma\rho \int_D dS \int_0^{h(r)} \frac{dz}{|\mathbf{r}_0 - \mathbf{r}|} \tag{4.17}$$

where γ is the Newtonian gravitational constant and ρ, per Parker, is a constant density. Assumptions:

- Define: $z = 0$ to be the mean seafloor within a domain of diameter D << diameter of the earth and is centered at the origin of the $x - y$ plane. Further, $R \equiv D/2$.
- Any influence of gravitational source outside R to be zero (the layer disappears for $|\vec{\mathbf{r}}|$ > R.

(The reader is advised to refer back to figure 2.3 for a depiction of the geometry, if required.) We differ here from Parker by applying the MHW as opposed to the FT.

$$\mathfrak{W}[U(\vec{\mathbf{r}}_0)] = \gamma\rho \int_D dS \int_0^{h(r)} dz \int_{-\infty}^{\infty} ({r_0}^2 - 1) e^{\frac{-r_0^2}{2}} \frac{dS_0}{|\mathbf{r}_0 - \mathbf{r}|} \tag{4.18}$$

As no analytical solution was apparent via traditional integration methods, the choice was made to take the FT of the MHW. Recall equation 4.10 and replace x with r_0:

$$\mathcal{F}[\psi_1(r)] = \int_0^\infty dr_0\, r_0\, J_0(kr_0)\, \frac{-1}{2}\left(\frac{e^{-r_0^2/2(1-r_0^2)}}{2\pi}\right) \tag{4.19}$$

Applying to the gravitational potential with constant density, as with Parker, results in

$$\mathcal{F}[\psi_1(r_0)] =$$

$$\int_0^\infty dr_0\, r\, J_0(kr_0)\, \frac{-1}{2}\left(\frac{e^{-r_0^2/2(1-r_0^2)}}{2\pi}\right) \int_D dxdy \int_0^{h(r)} dz\, \frac{1}{|r_0 - \mathrm{r}|} \tag{4.20}$$

Rearranging we have,

$$\mathcal{F}[\psi_1(r_0)] = \frac{-\gamma\rho}{4\pi} \int_D dxdy \int_0^{h(r)} dz \int_0^\infty dr_0\, r_0\, J_0(kr_0)\, \frac{e^{-r_0^2/2(1-r_0^2)}}{|r_0 - \mathrm{r}|} \tag{4.21}$$

Breaking up the last integral into two parts results in

$$\mathcal{F}[\psi_1(r_0)] = \frac{-\gamma\rho}{4\pi} \int_D dxdy \int_0^{h(r)} dz \left[- \int_0^\infty dr_0\, r_0\, J_0(kr_0) \left(\frac{r_0^2 e^{-r_0^2/2}}{|r_0 - \mathrm{r}|}\right) + \right.$$

$$\left. \int_0^\infty dr_0\, r_0\, J_0(kr_0) \left(\frac{e^{-r_0^2/2}}{|r_0 - \mathrm{r}|}\right)\right] \tag{4.22}$$

As we are integrating with respect to r_0, then r may be treated as a constant. As such, the result of the magnitude of (r_0-r) is the absolute value of (r_0-r).

From (Debnath, 1995), Parseval's Relation for Hankel transforms states

$$\int_0^\infty F_v(s)\, G_v(s) s\, ds = \int_0^\infty r\, g(r)\, f(r)\, dr \tag{4.23}$$

where $F_v(s) = \mathcal{H}a_v\{f(r)\}$ and $G_v(s) = \mathcal{H}a_v\{g(r)\}$, (4.24-4.25)

Where script "H" notes the Hankel transform. Utilizing table 12.2 of Bracewell (1965) and Parseval's Relation, equation 4.22 becomes slightly less daunting.

Note: the Hankel Transform of 1/r is 1/k. Thus, it is true that the Hankel Transform of $\frac{1}{abs(r_0 - r)}$ is $\frac{1}{abs(k-r)}$.

Further, from Bracewell table 12.2,

$$F_v(k) = \mathcal{H}a_v\left\{r_0^2 e^{-r_0^2/2}\right\} = 2(2-k^2)e^{-k^2/2} \tag{4.26}$$

$$G_v(k) = \mathcal{H}a_v\left\{\frac{1}{|(r_0-r)|}\right\} = \frac{1}{|(k-r)|} \tag{4.27}$$

$$Q_v(k) = \mathcal{H}a_v\left\{e^{-r_0^2/2}\right\} = e^{-k^2/2} \tag{4.28}$$

Applying Parseval's Relation:

$$-\int_0^\infty dr_0\, r_0 J_0(kr_0)\left(\frac{r_0^2 e^{-r_0^2/2}}{abs(r_0-\mathrm{r})}\right) + \int_0^\infty dr_0\, r_0 J_0(kr_0)\left(\frac{e^{-r_0^2/2}}{abs(r_0-\mathrm{r})}\right) = -\int_0^\infty \frac{2(2-k^2)e^{-k^2/2}}{abs(k-\mathrm{r})}\,kdk + \int_0^\infty \frac{e^{-k^2/2}}{abs(k-\mathrm{r})}\,kdk \tag{4.29}$$

As noted by Papoulis (1965), it is well known that the more general form of the Gaussian Integral

$$\int_{-\infty}^{\infty} e^{-ax^2}\,dx = \sqrt{\frac{\pi}{a}} \tag{4.30}$$

Similarly from (C. P. Nicholas, 1950), we can show that

$$\int_0^{\infty} e^{-x^2}\,dx = \frac{\sqrt{\pi}}{2} \tag{4.31}$$

The proof by Nichols is shown in Appendix E.

Alternatively, the Gaussian function is an even function

$$f(x) = e^{-x^2} \tag{4.32}$$

That is, f(x) = f(-x), or f(x) – f(-x) = 0.

So, we can show that indeed

$$\int_{-\infty}^{\infty} e^{-x^2}\,dx = 2\int_0^{\infty} e^{-x^2}\,dx = \sqrt{\pi} \tag{4.33}$$

And thus it would follow that

$$\int_{-\infty}^{\infty} e^{-ax^2}\,dx = 2\int_{0}^{\infty} e^{-ax^2}\,dx = \sqrt{\frac{\pi}{a}} \tag{4.34}$$

To solve the more general form of the Gaussian integral (equation 4.35 below), differentiation under the integral is applied with respect to the constant "a".

We will set n=1 and a=1/2 for equation 4.35,

$$\int_{0}^{\infty} x^{2n} e^{-ax^2} dx = \left(-\frac{d}{da}\right)\int_{0}^{\infty} e^{-ax^2} dx \tag{4.35}$$

Recall from equation 4.32, the solution to the Gaussian integral from zero to infinity equals the square root of pi over "a" times one-half. So, we have

$$\int_{0}^{\infty} x^{2} e^{-ax^2} dx = \left(-\frac{d}{da}\right)\left(\frac{1}{2}\sqrt{\frac{\pi}{a}}\right) = \frac{\sqrt{2\pi}}{2} \tag{4.36}$$

Equivalently from (Abramowitz, 1964) or (Spiegel, 1968),

$$\int_{0}^{\infty} x^{2n} e^{-x^2/a^2}\,dx = \sqrt{\pi}\frac{(2n)!}{n!}\left(\frac{a}{2}\right)^{2n+1} \tag{4.37}$$

And with n=1 and $a = \sqrt{2}$, the same solution from equation 4.36 is reached.

$$\int_{0}^{\infty} x^{2} e^{-x^2/\sqrt{2}^2} dx = \frac{\sqrt{2\pi}}{2} \tag{4.38}$$

4.4.1 *Case 1: r=0*

For r=0 and $k \in \mathbb{R}\ and\ k > 0$, $\frac{k}{abs(k-r)} = 1$. That is, the source point resides on the z-axis (see figure 1). Thus,

$$-2\int_{0}^{\infty} 2(2-k^2)e^{-k^2/2}\,dk + \int_{0}^{\infty} e^{-k^2/2}\,dk =$$

$$-4\int_{0}^{\infty} e^{-k^2/2}\,dk + 2\int_{0}^{\infty} k^2 e^{-k^2/2}\,dk + \int_{0}^{\infty} e^{-k^2/2}\,dk = \left(-\frac{\sqrt{2\pi}}{2}\right) \tag{4.39}$$

Thus, with the integrals converging to a numerical answer, equation 4.22 resolves to:

$$\mathcal{F}[\psi_1(r_0)] = \frac{\gamma\rho(\sqrt{2\pi})}{8\pi}\int_D dxdy\int_0^{h(r)} dz \tag{4.40}$$

Evaluating the integral with respect to z thus results in

$$\mathcal{F}[\psi_1(r_0)] = \frac{\gamma\rho\, h(r)(\sqrt{2\pi})}{8\pi}\int_D dxdy \tag{4.41}$$

The power of the FT of the MHW thus allows for the convergence of otherwise difficult integrals to a simple integral calculation of the wavelet transform of the gravitational potential.

Prior to attempting a solution to the right-hand-side of equation 4.29, either analytically or numerically, we can study its behavior by varying "r."

4.4.2 *Case 2: r = k*

$$\int_0^\infty \frac{e^{-k^2}k^2}{abs(k-r)}\cdot k\, dk = \int_0^\infty \frac{e^{-k^2}}{abs(k-r)}\cdot k\, dk = undefined \tag{4.42}$$

4.4.3 *Case 3: r sufficiently larger than k*

$$\int_0^\infty \frac{e^{-k^2}k^2}{abs(k-r)}\cdot k\, dk = \int_0^\infty \frac{e^{-k^2}}{abs(k-r)}\cdot k\, dk = 0 \tag{4.43}$$

Equation 4.43 vanishes as n is odd and the function is an odd function (Conrad). We may thus assume that the behavior of equation 4.29 will give results for only certain values of "r."

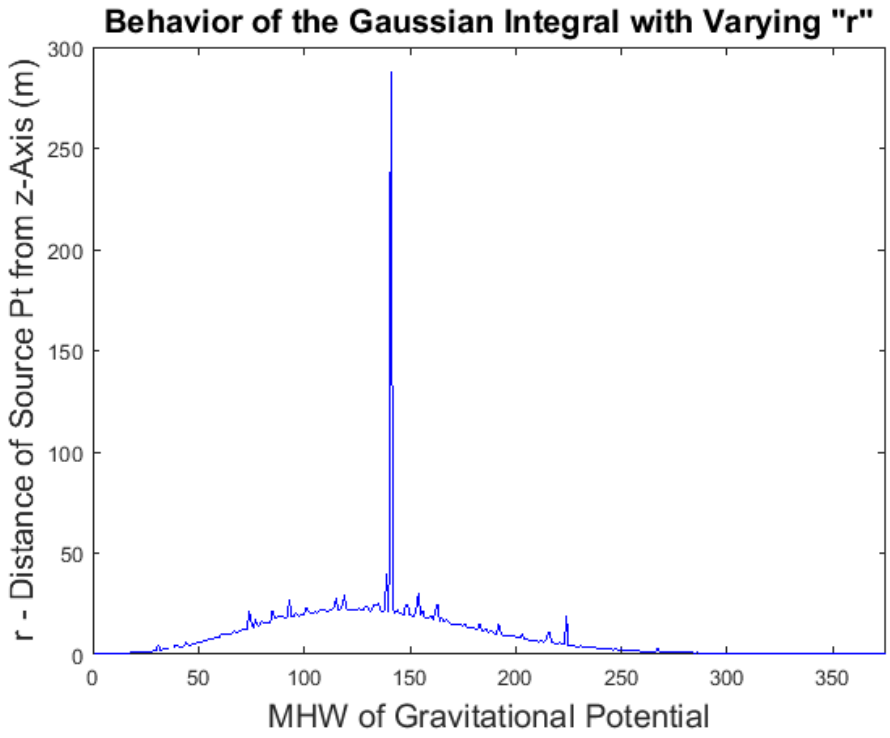

Figure 4.10 Behavior of equation 28 as “r” varies.

As is seen in figure 4.10, our assumption of the behavior of the general case for equation 4.35 is valid. There is only a small range of values of “r” that yield a value greater than zero and that a discontinuity exists where k=r. Now looking at the behavior of the full set of integrals on the right hand side of equation 4.29 with respect to “r”, we see that this trend holds. See figure 4.11 below.

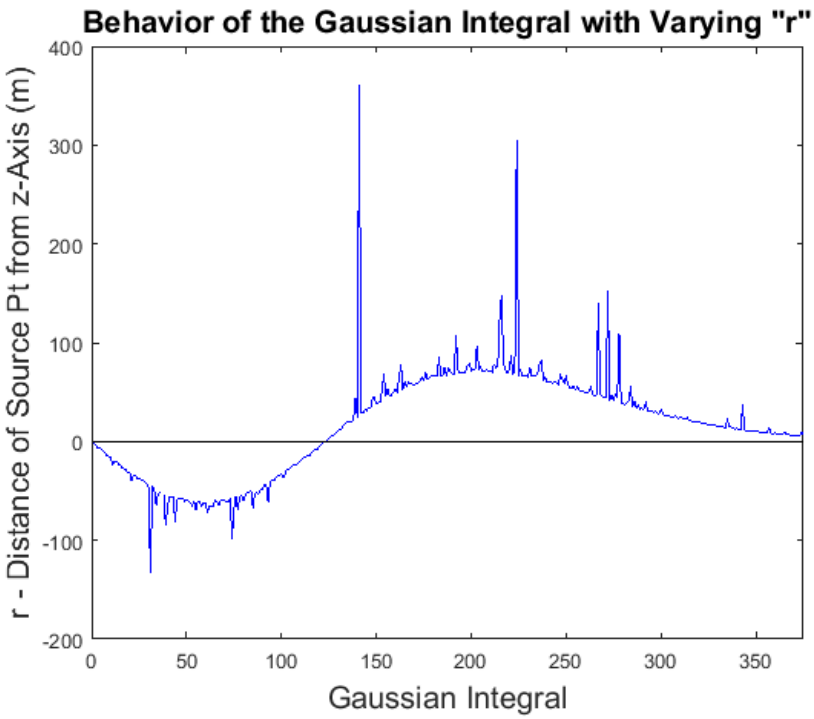

Figure 4.11 Behavior of equation 15 with respect to "r."

4.4.4 *Use the FT(MHW) to show end-to-end Prediction for Case r=0:*

As with the Fourier solution that shows end-to-end prediction of bathymetry, we will similarly follow the procedure, however, with the FT of the MHW.

Recall from Moritz:

$$\Delta g = -\frac{\partial u(x,0)}{\partial z} \text{ and } \frac{\partial \Delta g}{\partial z} + g_0\left[\frac{\partial \eta(x)}{\partial x} + \frac{\partial \xi(x)}{\partial y}\right] \tag{4.44}$$

Now, define both $\eta(x)$ and $\xi(x)$ utilizing equations (A3 and A4) of Sandwell and Smith (1997).

$$\eta(x) \cong -\frac{1}{g_0}\frac{\partial\left(\gamma\rho \int_D dxdy \int_0^{h(r)} dz \frac{1}{|\vec{\mathbf{r}}_\mathbf{0}-\vec{\mathbf{r}}|}\right)}{\partial x} = \cong \frac{\gamma\rho\, h(r)(\sqrt{2\pi})}{8\pi g_0}\int_D dy \tag{4.45}$$

$$\xi(x) \cong -\frac{1}{g_0}\frac{\partial\left(\gamma\rho \int_D dxdy \int_0^{h(r)} dz \frac{1}{|\vec{\mathbf{r}}_\mathbf{0}-\vec{\mathbf{r}}|}\right)}{\partial y} = \cong \frac{\gamma\rho\, h(r)(\sqrt{2\pi})}{8\pi g_0}\int_D dx \tag{4.46}$$

Recall from Sandwell and Smith (1997) that

$$\frac{\partial}{\partial x}\left|\vec{k}\right| = \frac{\partial}{\partial x}\left(k_x^2 + k_y^2\right)^{1/2} = \frac{1}{2}\left(k_x^2 + k_y^2\right)^{1/2} * 2k_x = \frac{k_x}{|\vec{k}|} \tag{4.47}$$

Similarly, $\frac{\partial}{\partial y}\left|\vec{k}\right| = \frac{k_y}{|\vec{k}|}$ (4.48)

$$\Im[\psi_1(U_0)] = -g_0\left[\frac{\partial\eta(x)}{\partial x} + \frac{\partial\xi(x)}{\partial y}\right] \tag{4.49}$$

Expanding

$$\frac{G\rho\, h(r)\left(\sqrt{2\pi}\right)}{8\pi}\int_D dxdy \;= \frac{g_0\gamma\rho\, h(r)\left(\sqrt{2\pi}\right)}{8\pi|k|}\left[k_x\int_D dy \;+ k_y\int_D dx\right] \tag{4.50}$$

Now cancelling like terms results in

$$\int_D dxdy = \frac{g_0}{|k|}\left[k_x\int_D dy \;+ k_y\int_D dx\right] \tag{4.51}$$

Equation 4.51 thus shows the end-to-end prediction of bathymetry, similar to Sandwell and Smith, however, utilizing the FT of the MHW for the case of r=0.

4.4.5 General Case

As an analytical solution is not plain to see, a numerical integration method is applied in order to determine a general case solution. Due to the Gaussian in the integrands as well other functions, "k" and "k^3", the 2 point Gauss-Hermite Quadrature rule was chosen. The formula is as follows:

$$\int_{-\infty}^{\infty} e^{-x^2} f(x)dx = \sum_{i=1}^{2} w_i f(x_i) \tag{4.52}$$

where,

$$w_i = \frac{2^{n+1}n!\sqrt{\pi}}{\left[H_n'(x_i)\right]^2} \tag{4.53}$$

and

$$H_n(x) = (-1)^n e^{x^2} \frac{d^n}{dx^n}\left(e^{-x^2}\right) \text{ and } H_n' = \frac{d}{dx}\left(H_n(x)\right) \quad (4.54, 4.55)$$

In order to accommodate for the addition of the constant (1/2) in the exponential, equation 4.53 is modified per equation 4.30 to be

$$w_i = \frac{2^{n+1} n! \sqrt{\frac{\pi}{2}}}{\left[H_n'(x_i)\right]^2} \quad (4.56)$$

Further, as we are integrating from 0 to infinity but the Gauss-Hermite formula is from negative infinity to positive infinity, a factor of ½ is added to the computed solution. This is valid as mentioned previously because the Gaussian function is even.

Using equation 4.47, we solve for $H_2(x)$:

$$H_2(x) = e^{x^2/2} \frac{d^2}{dx^2}\left(e^{-x^2/2}\right) = x^2 - 1 \quad (4.57)$$

Setting $H_2(x) = 0$, $x_k = \pm 1$. Now we solve for w_i:

$$w_i = \frac{2^{2+1}\, 2!\sqrt{\pi}}{\left[H_n'(x_i)\right]^2} \quad (4.58)$$

where

$$H_n' = \frac{d}{dx}[x^2 - 1] = 2x \quad (4.59)$$

Thus,

$$H_n'(x_i) = 2(\pm 1) = \pm 2 \quad (4.60)$$

The solution to equation 4.58 is thus,

$$w_i = \frac{2^{2+1}\, 2!\sqrt{\pi}}{[2]^2} = 4\sqrt{\frac{\pi}{2}} \quad (4.61)$$

$$w_1\left(f(x_1) + f(x_2)\right) \quad (4.62)$$

We substitute x_k = plus and minus 1, respectively into equation 4.62 and multiply the result by w_i, After changing variables from x to k,

$$\int_{-\infty}^{\infty} e^{-k^2/2}\ \frac{k}{abs(k-r)}\,dk \cong 4\sqrt{\frac{\pi}{2}}\left(\frac{1}{abs(1-r)} - \frac{1}{abs(-1-r)}\right) \tag{4.63}$$

We similarly obtain the same result utilizing the computed w_i and H_n for the integral below

$$\int_{-\infty}^{\infty} e^{-k^2/2}\ \frac{k^3}{abs(k-r)}\,dk \tag{4.64}$$

We now have an estimate to the RHS of equation 4.29 as

$$-2\sqrt{\frac{\pi}{2}}\left(\frac{1}{abs(1-r)} - \frac{1}{abs(-1-r)}\right), for\ k \in \mathbb{R}\ and\ k > 0 \tag{4.65}$$

4.4.5.1 *Use the FT(MHW) to show end-to-end Prediction for the General Case:*

For the general case with the conditions of equation 4.65, equation 4.22 becomes:

$$\mathcal{F}[\psi_1(r_0)] = \frac{\gamma\rho\left(\frac{1}{abs(1-r)} - \frac{1}{abs(-1-r)}\right)h(r)}{2\pi}\sqrt{\frac{\pi}{2}}\int_D dxdy \tag{4.66}$$

As such,

$$\eta(x) \cong -\frac{1}{g_0}\frac{\partial\left(\gamma\rho\int_D dxdy\int_0^{h(r)} dz\frac{1}{|\vec{\mathbf{r}}_\mathbf{0}-\vec{\mathbf{r}}|}\right)}{\partial x} =$$

$$\frac{-\gamma\rho\left(\frac{1}{abs(1-r)} - \frac{1}{abs(-1-r)}\right)h(r)}{2\pi g_0}\sqrt{\frac{\pi}{2}}\int_D dy \tag{4.67}$$

$$\xi(x) \cong -\frac{1}{g_0}\frac{\partial\left(\gamma\rho\int_D dxdy\int_0^{h(r)} dz\frac{1}{|\vec{\mathbf{r}}_\mathbf{0}-\vec{\mathbf{r}}|}\right)}{\partial y} =$$

$$\frac{-\gamma\rho\left(\frac{1}{abs(1-r)} - \frac{1}{abs(-1-r)}\right)h(r)}{2\pi g_0}\sqrt{\frac{\pi}{2}}\int_D dx \tag{4.68}$$

and equation 4.51 remains: $\int_D dxdy = \frac{g_0}{|k|}\left[k_x\int_D dy\ + k_y\int_D dx\right]$

4.5 Simple numerical examples: The potentials for the monopole and cone.

As a proof of concept for the utility of the MHW versus the FT, two simple potentials, for the monopole and cone, were numerically transformed with each method. Their RMSE was then computed and compared. For the FT, a windowed FT was again used in order to compare step by step with the wavelets. Further, a few other wavelets were also used to transform the potentials, namely db1 (discrete) and the Paul wavelet (continuous). The results were similar to those determined for the step function (Figure 4.1).

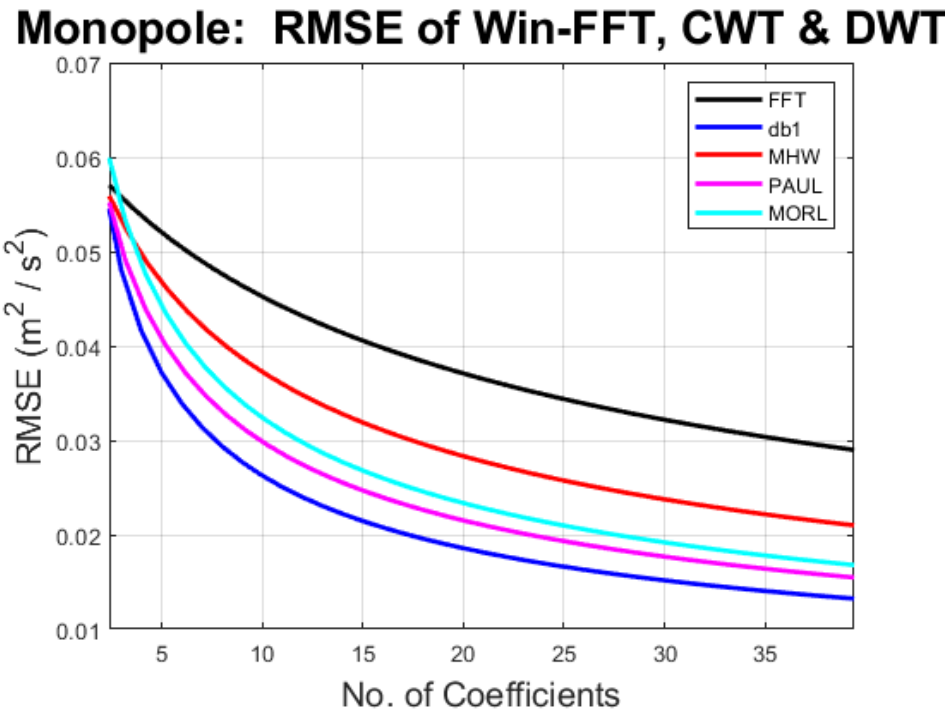

Figure 4.12 Comparison of computed RMSEs for the monopole potential.

Again, the wavelet transforms significantly outperformed the FT. Each of the three wavelets used, red (MHW), fuchsia (Paul) and blue (db1) were able to lower RMSE much faster with a smaller number of coefficients used. Similarly for the cone potential, these three wavelet transforms outperformed the FT. In this case, however, the wavelets

did not have an appreciable difference between their respective RMSEs. Figure 4.13 depicts the geometry of the cone and 4.14 shows the comparison of the four transforms.

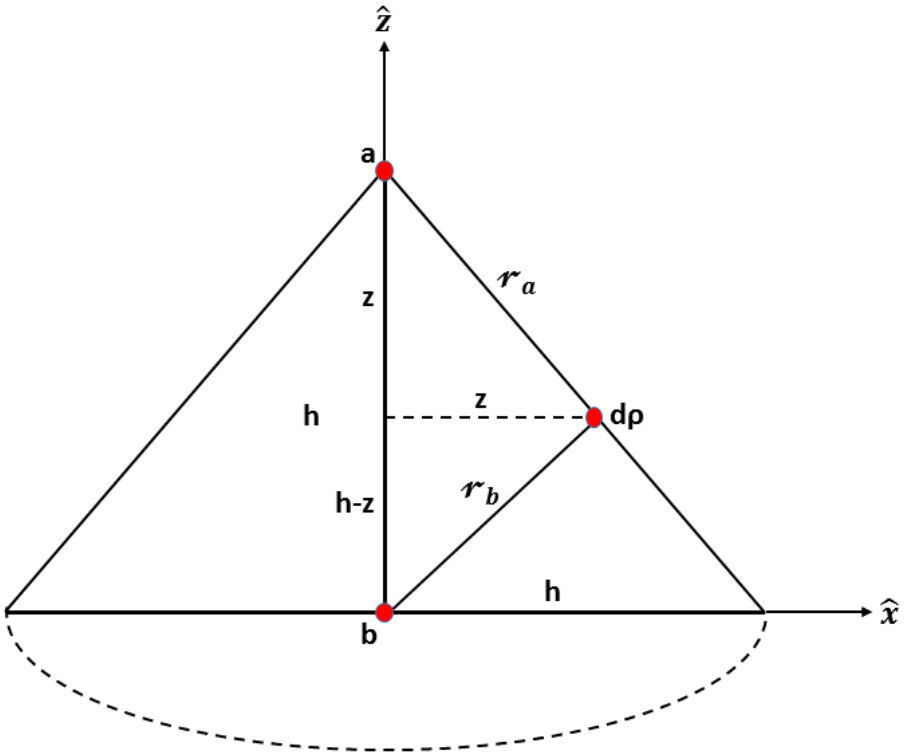

Figure 4.13 Geometry of a Cone

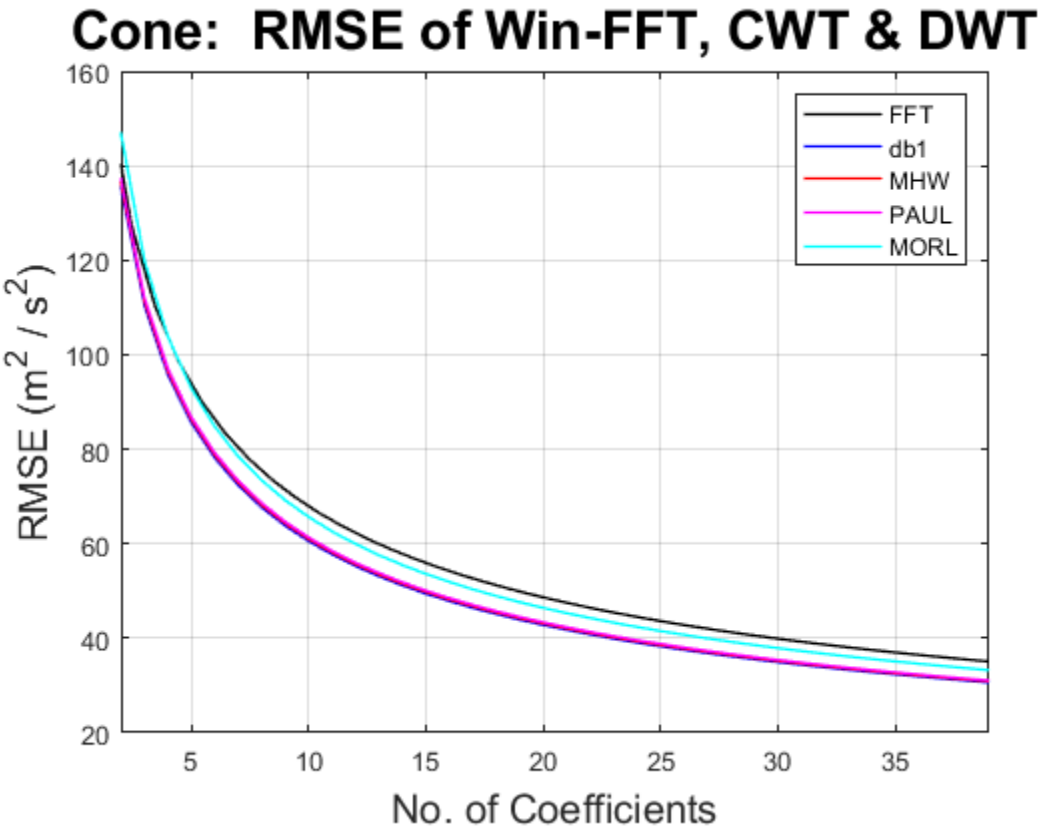

Figure 4.14 Comparison of computed RMSEs for the potential of a cone.

4.6 Numerical Solution to the Morlet wavelet transform applied to the Newtonian Potential

$$\psi(x_0) = \pi^{-1/4}\, e^{is\omega_0^1 x} e^{-x^2/2s^2} \tag{4.69}$$

where ω_0^1 is frequency. This value is a constant and the default value used by Mathworks, is set to 6. The value was coded as a soft value, however, the recommended default was used in the numerical solution code. Recall now equation 2.37:

$$\mathcal{F}\,[U(\vec{\mathbf{r}}_0)] = \gamma\rho \int_D dS \int_0^{h(\vec{\mathbf{r}})} dz \int_X \frac{e^{i\vec{k}\cdot((w_0+r)\hat{r}}}{(w_0^2+a_0^2)^{1/2}} w_0 dw_0 d\vartheta$$

The same equation is utilized, however, the Morlet wavelet is applied and thus the numerator in the final integral is appropriately replaced in accordance with equation 4.69.

$$\mathrm{W}\,[U(\vec{\mathbf{r}}_0)] \;= \gamma\rho \int_D dS \int_0^{h(\vec{\mathbf{r}})} dz \int_X \frac{\pi^{-1/4}\, e^{is\omega_0^1 x} e^{-x^2/2s^2}}{(w_0^2+{a_0}^2)^{1/2}} w_0 dw_0 d\vartheta \qquad (4.70)$$

Integrating with respect to υ first, removing the pi constant to outside the remaining integrals and combing the two exponentials results in:

$$\mathrm{W}\,[U(\vec{\mathbf{r}}_0)] \;= \frac{2\pi\gamma\rho}{\pi^{-1/4}} \int_D dS \int_0^{h(\vec{\mathbf{r}})} dz \int_X \frac{e^{is\omega_0^1 x - x^2/2s^2}}{(w_0^2+a_0^2)^{1/2}} w_0 dw_0 \qquad (4.71)$$

The variable 'x' is now replaced with the term$(w_0 + r)\hat{r}$, yielding

$$\mathrm{W}\,[U(\vec{\mathbf{r}}_0)] \;= \frac{2\pi\gamma\rho}{\pi^{-1/4}} \int_D dS \int_0^{h(\vec{\mathbf{r}})} dz \int_X \frac{e^{is\omega_0^1 (w_0+r)\hat{r} - (w_0+r)\hat{r}^2/2s^2}}{(w_0^2+a_0^2)^{1/2}} w_0 dw_0 \quad (4.72)$$

Rearranging the integrals in order to integrate with respect z, ('a') gives

$$\mathrm{W}\,[U(\vec{\mathbf{r}}_0)] \;= \frac{2\pi\gamma\rho}{\pi^{-1/4}} \int_D dS \int_X \int_0^{h(\vec{\mathbf{r}})} dz \frac{e^{is\omega_0^1 (w_0+r)\hat{r} - (w_0+r)\hat{r}^2/2s^2}}{(w_0^2+a_0^2)^{1/2}} w_0 dw_0 \quad (4.73)$$

Recall that $a_0 = z_0 - z$. The term in the denominator was integrated with respect to z utilizing the online tool, Wolfram Alpha. The result is:

$$\int_0^{h(\vec{r})} \frac{1}{(w_0^2+a_0^2)^{1/2}} da = ln\left(\sqrt{w_0^2 + a_0^2} + a_0\right)\Big|_0^{h(\vec{\mathbf{r}})} \qquad (4.74)$$

After replacing a0 with z_0-z, and applying the limits we have:

$$\mathrm{W}\,[U(\vec{\mathbf{r}}_0)] \;= \frac{2\pi\gamma\rho}{\pi^{-1/4}} \int_D dS \int_X \left(e^{is\omega_0^1 (w_0+r)\hat{r} - (w_0+r)\hat{r}^2/2s^2}\right) ln\left(\sqrt{w_0^2 + (z_0 - h(\vec{\mathbf{r}}))^2} + z_0 - h(\vec{\mathbf{r}})\right) + ln\left(\sqrt{w_0^2 + {z_0}^2} + z_0\right) w_0 dw_0 \qquad (4.73)$$

With no obvious analytical solution to the integral with respect to w_0, a numerical approach was made utilizing the trapezoidal quadrature rule, per Phillips and Taylor, 1996. Although, this particular quadrature technique is not the most accurate (other

methods may achieve a higher degree of accuracy), its simplicity in application made it a good choice to apply to such a complex problem. Further, as a very large number of terms can be made in a loop in MATLAB, without much impact on calculation time, any potential error is rapidly mitigated. The following solution was entered into a MATLAB routine, with the number of terms used based on the size of the dataset, typically greater than 80.

$$\mathrm{W}\left[U(\vec{\mathbf{r}}_0)\right] = \frac{2\pi\gamma\rho}{\pi^{-1/4}} \int_D dS =$$

$$\frac{1}{2}\left[\left((-w_0)e^{is\omega_0^1(w_0+r)\hat{r} - (w_0+r)\hat{r}^2/2s^2}\right) ln\left(\sqrt{(-w_0)^2 + (z_0 - h(\vec{\mathbf{r}}))^2} + z_0 - h(\vec{\mathbf{r}})\right) +\right.$$

$$ln\left(\sqrt{(-w_0)^2 + {z_0}^2} + z_0\right) +$$

$$\left((w_0)e^{is\omega_0^1(w_0+r)\hat{r} - (w_0+r)\hat{r}^2/2s^2}\right) ln\left(\sqrt{(w_0)^2 + (z_0 - h(\vec{\mathbf{r}}))^2} + z_0 - h(\vec{\mathbf{r}})\right) +$$

$$ln\left(\sqrt{(w_0)^2 + {z_0}^2} + z_0\right) +$$

$$2\sum_{n=-w_0+1}^{w_0-1}\left((-w_0)e^{is\omega_0^1(w_0+r)\hat{r} - (w_0+r)\hat{r}^2/2s^2}\right) ln\left(\sqrt{(-w_0)^2 + (z_0 - h(\vec{\mathbf{r}}))^2} + z_0 -\right.$$

$$\left. h(\vec{\mathbf{r}})\right) + ln\left(\sqrt{(-w_0)^2 + {z_0}^2} + z_0\right)\Bigg] \tag{4.74}$$

where "s" is scale.

4.7 Numerical Solution to the Paul wavelet transform applied to the Newtonian Potential

From Torrence and Compo, 1998, we define the Paul wavelet basis function, including scale here as:

$$\psi(x_0) = \frac{2^m i^m m!}{\sqrt{\pi(2m)!}}(1 - ix)^{-(m+1)} \tag{4.75}$$

where the variable m has a MATLAB default value of 4. This value was soft-coded into the script, however the default value was used. Moving ahead to a similar position as equation 4.71, albeit with the new wavelet, and the z-integral already solved for (same as before) we have

$$\mathrm{W}\,[U(\vec{\mathbf{r}}_0)] = 2\pi\left(\frac{2^m i^m m!}{\sqrt{\pi(2m)!}}\right)\gamma\rho\int_D dS\int_X \frac{(1-i(w_0+\curlyvee)\curlyvee)^{-(m+1)}}{(w_0^2+a_0^2)^{1/2}} ln\left(\sqrt{w_0^2 + (z_0 - h(\vec{\mathbf{r}}))^2} + z_0 - h(\vec{\mathbf{r}})\right) + ln\left(\sqrt{w_0^2 + {z_0}^2} + z_0\right) w_0 dw_0 \tag{4.76}$$

Applying the trapezoidal quadrature rule to integrate with respect to w_0,

$$\mathrm{W}\,[U(\vec{\mathbf{r}}_0)] = 2\pi\left(\frac{2^m i^m m!}{\sqrt{\pi(2m)!}}\right)\gamma\rho\int_D dS\,\frac{1}{2}\left[\left((-w_0)\left(1 - i\big((-w_0) + \curlyvee\big)\right)^{-(m+1)}\right) ln\left(\sqrt{(-w_0)^2 + \left(z_0 - h(\vec{\mathbf{r}})\right)^2} + z_0 - h(\vec{\mathbf{r}})\right) + ln\big(\sqrt{(-w_0)^2 + {z_0}^2} + z_0\big) + \left((w_0)\left(1 - i\big((-w_0) + \curlyvee\big)\right)^{-(m+1)}\right) ln\left(\sqrt{(w_0)^2 + \left(z_0 - h(\vec{\mathbf{r}})\right)^2} + z_0 - h(\vec{\mathbf{r}})\right) + ln\big(\sqrt{(w_0)^2 + {z_0}^2} + z_0\big) + 2\sum_{n=-w_0+1}^{w_0-1}\left((-w_0)\left(1 - i\big((-w_0) + \curlyvee\big)\right)^{-(m+1)}\right) ln\left(\sqrt{(-w_0)^2 + \left(z_0 - h(\vec{\mathbf{r}})\right)^2} + z_0 - h(\vec{\mathbf{r}})\right) + ln\big(\sqrt{(-w_0)^2 + {z_0}^2} + z_0\big)\right] * s \tag{4.77}$$

4.8 Derivation of the Derivative Theorem for the Mexican Hat, Paul and Morlet Wavelets

Note: The Mexican Hat and Morlet are both Gaussian based, while the Paul wavelet is not.

Following the proof for the derivative theorem for Fourier Transforms, as outlined by Bracewell (1965) (see Appendix G), we begin the proof by making the statement that for a function f(x) there exists a wavelet transform W(a,b). The derivative of the function, f‘(x) must also have a transform. From Starck et. al. 2015, we begin with the inverse wavelet transform:

$$f(x) = \frac{1}{C_\chi}\int_0^\infty \int_{-\infty}^\infty \frac{1}{\sqrt{a}} W(a,b)\, \chi\left(\frac{x-b}{a}\right)\frac{dadb}{a^2} \tag{4.78}$$

where χ is the wavelet function to be considered and Cχ is constant given by formula 4.79 below.

$$C_\chi = \int_0^\infty \frac{\widehat{\psi}^*(\nu)\widehat{\chi}(\nu)}{\nu} d\nu = \int_{-\infty}^0 \frac{\widehat{\psi}^*(\nu)\widehat{\chi}(\nu)}{\nu} d\nu \tag{4.79}$$

We begin with the Mexican Hat wavelet.

$$f(x) = \frac{1}{C_\chi}\int_0^\infty \int_{-\infty}^\infty \frac{1}{\sqrt{a}} W(a,b)\left(1-\left(\frac{x-b}{a}\right)^2\right) e^{\frac{-(x-b)^2}{2a^2}}\frac{dadb}{a^2} \tag{4.80}$$

We then take the derivative of both sides of the equation.

$$f'(x) = \frac{1}{C_\chi}\int_0^\infty \int_{-\infty}^\infty \frac{1}{\sqrt{a}} W(a,b)\frac{d}{dx}\left[\left(1-\left(\frac{x-b}{a}\right)^2\right) e^{\frac{-(x-b)^2}{2a^2}}\right]\frac{dadb}{a^2} \tag{4.81}$$

After differentiation of the term in brackets and re-arrangement, we get

$$f'(x) = \frac{1}{C_\chi}\int_0^\infty \int_{-\infty}^\infty \frac{1}{\sqrt{a}} W(a,b)\, \chi\left(\frac{x-b}{a}\right)\left[\frac{(x-b)}{a^2} - \frac{2(x-b)}{(a^2-(x-b)^2)}\right]\frac{dadb}{a^2} \tag{4.82}$$

X is the analyzing wavelet that was just differentiated. As the new term, in brackets, is actually in the form ψ(x-b/a), it cannot be removed from the integral. As such, the

inverse wavelet transform of the derivative of the function utilizing the Mexican Hat wavelet does not have an analytical solution. A numerical approach must be made. Next we will similarly evaluate for the Morlet wavelet defined by Torrence and Compo, (1998).

$$f(x) = \frac{1}{C_\chi}\int_0^\infty \int_{-\infty}^\infty \frac{1}{\sqrt{a}} W(a,b)\left(e^{i\omega_0\frac{(x-b)}{a}} e^{\frac{-(x-b)^2}{2a^2}}\right)\frac{dadb}{a^2} \tag{4.83}$$

We then take the derivative of both sides of the equation.

$$f'(x) = \frac{1}{C_\chi}\int_0^\infty \int_{-\infty}^\infty \frac{1}{\sqrt{a}} W(a,b)\frac{d}{dx}\left(e^{i\omega_0\frac{(x-b)}{a}} e^{\frac{-(x-b)^2}{2a^2}}\right)\frac{dadb}{a^2} \tag{4.84}$$

After differentiation of the term in brackets and re-arrangement, we get

$$f'(x) = \frac{1}{C_\chi}\int_0^\infty \int_{-\infty}^\infty \frac{1}{\sqrt{a}} W(a,b)\left(e^{is\omega_0\frac{(x-b)}{a}} e^{\frac{-(x-b)^2}{2a^2}}\right)\left(\frac{(x-b)}{a^2} + \frac{is\omega_0 x}{a}\right)\frac{dadb}{a^2} \tag{4.85}$$

Rearranging again,

$$f'(x) = \frac{1}{C_\chi}\int_0^\infty \int_{-\infty}^\infty \frac{1}{\sqrt{a}} W(a,b)\,\chi\left(\frac{x-b}{a}\right)\left(\frac{(x-b)}{a^2} + \frac{is\omega_0 x}{a}\right)\frac{dadb}{a^2} \tag{4.86}$$

Finally, we will evaluate for the Paul wavelet also defined by Torrence and Compo, (1998).

$$f(x) = \frac{1}{C_\chi}\int_0^\infty \int_{-\infty}^\infty \frac{1}{\sqrt{a}} W(a,b)\left[\frac{2^m i^m m!}{\sqrt{\pi(2m)!}}\left(1 - i\frac{(x-b)}{a}\right)^{-(m+1)}\right]\frac{dadb}{a^2} \tag{4.87}$$

We then take the derivative of both sides of the equation.

$$f'(x) = \frac{1}{C_\chi}\int_0^\infty \int_{-\infty}^\infty \frac{1}{\sqrt{a}} W(a,b)\frac{d}{dx}\left[\frac{2^m i^m m!}{\sqrt{\pi(2m)!}}\left(1 - i\frac{(x-b)}{a}\right)^{-(m+1)}\right]\frac{dadb}{a^2} \tag{4.88}$$

After differentiation of the term in brackets and re-arrangement, we get

$$f'(x) = \frac{1}{C_\chi}\int_0^\infty \int_{-\infty}^\infty \frac{1}{\sqrt{a}} W(a,b)\left[\frac{2^m i^m m!}{\sqrt{\pi(2m)!}}(1 - ix)^{-(m+1)}\right]\left(\frac{i(m+1)}{1-ix}\right)\frac{dadb}{a^2} \tag{4.89}$$

Rearranging again,

$$f'(x) = \frac{1}{C_\chi}\int_0^\infty \int_{-\infty}^\infty \frac{1}{\sqrt{a}} W(a,b)\chi\left(\frac{x-b}{a}\right)\left(\frac{i(m+1)}{a-i(x-b)}\right)\frac{dadb}{a^2} \qquad (4.90)$$

Similar to the result for the derivative of f(x) utilizing the Mexican Hat wavelet, the additional terms for the Morlet and Paul wavelets are in the form of ψ(x-b/a). Thus, again an analytical solution cannot be made and a numerical approach must considered. It is also important to note, however, that in order for the inverse wavelet transform to exist, an admissibility condition must first be met (Starck et al, 2015). That is, Cχ must be finite. Per Starck, this means that the mean of the wavelet must be zero or similarly presented,

$$\hat{\psi}(0) = 0 \qquad (4.91)$$

This condition was met for all three wavelets examined here.

4.9 Comparison of results between continuous wavelets and the FT

For the comparison of the two types of transforms, data from the Columbia University, Multi-ridge Synthesis Project was used. The data set provided has units in meters. The data covered the well-known area of the Southern East Pacific Rise due to the many seamounts located there. As has been stated already, wavelets are local and FTs are not. Whereas wavelet reconstructions will examine only those coefficients specified for a specific window, the FT will attempt to reconstruct the whole signal, making a comparison of the two reconstructions difficult. Daubechies (1992) noted that the concept of wavelets came from windowing the FT; however, windowing allows for someone to examine the localized power spectral density of the

signal. It does not help with signal reconstruction as the window chosen is multiplied with the signal and thereby results in a function quite different from the signal in question. In order to best compare the reconstructions on a term-by-term basis the following procedure was established.

1. Compute the coefficients for a signal utilizing each transform.
2. Reconstruct the signal term-by-term creating a matrix where each successive row contains one more coefficient than the previous.
3. Pad each row with zeros so that the length of the row is equivalent to the length of the original signal.
4. Compute the root mean square error for each reconstruction row-by-row.

The examination of the reconstruction begins with a 1D slice at latitude -8 degrees South. See figure 4.15.

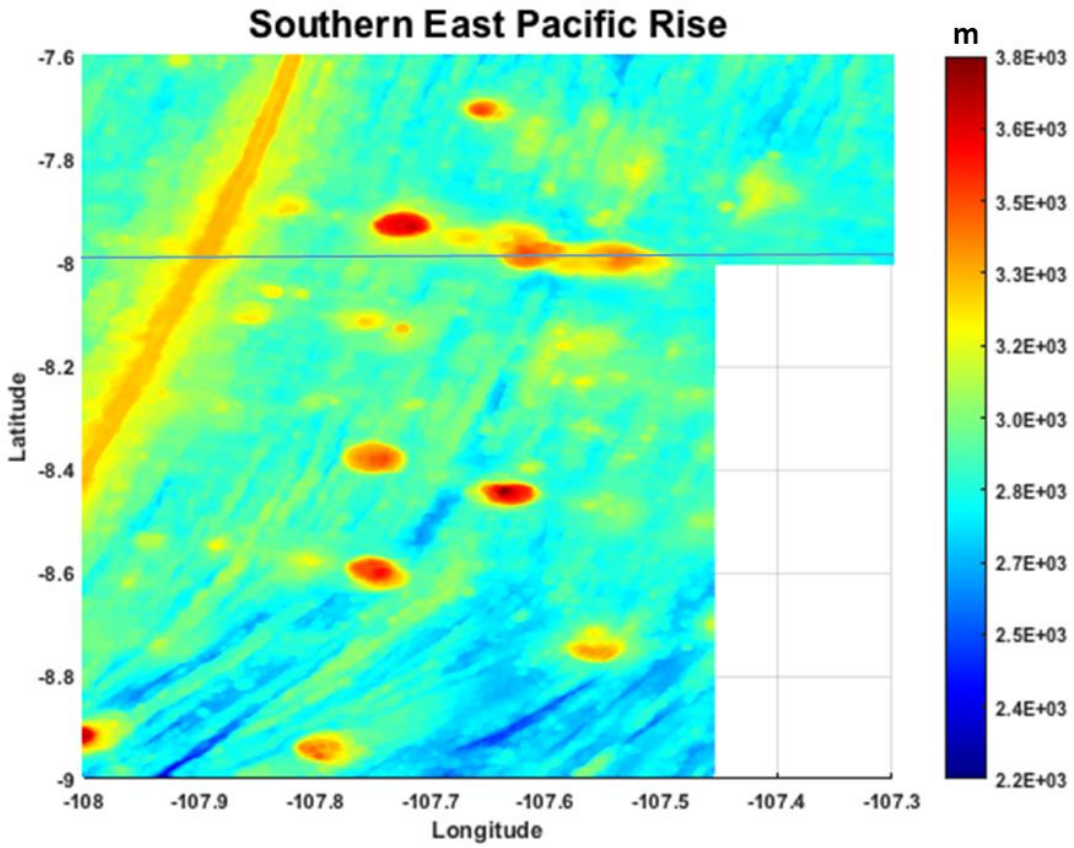

Figure 4.15 Southern East Pacific Rise Topography

The slice of data at -8 degrees latitude runs through two adjacent seamounts. Following the procedure just outlined, reconstructions of the data slice by the FT, MHW, Paul and Morlet wavelet transforms are compared side-by-side. See figure 4.16.

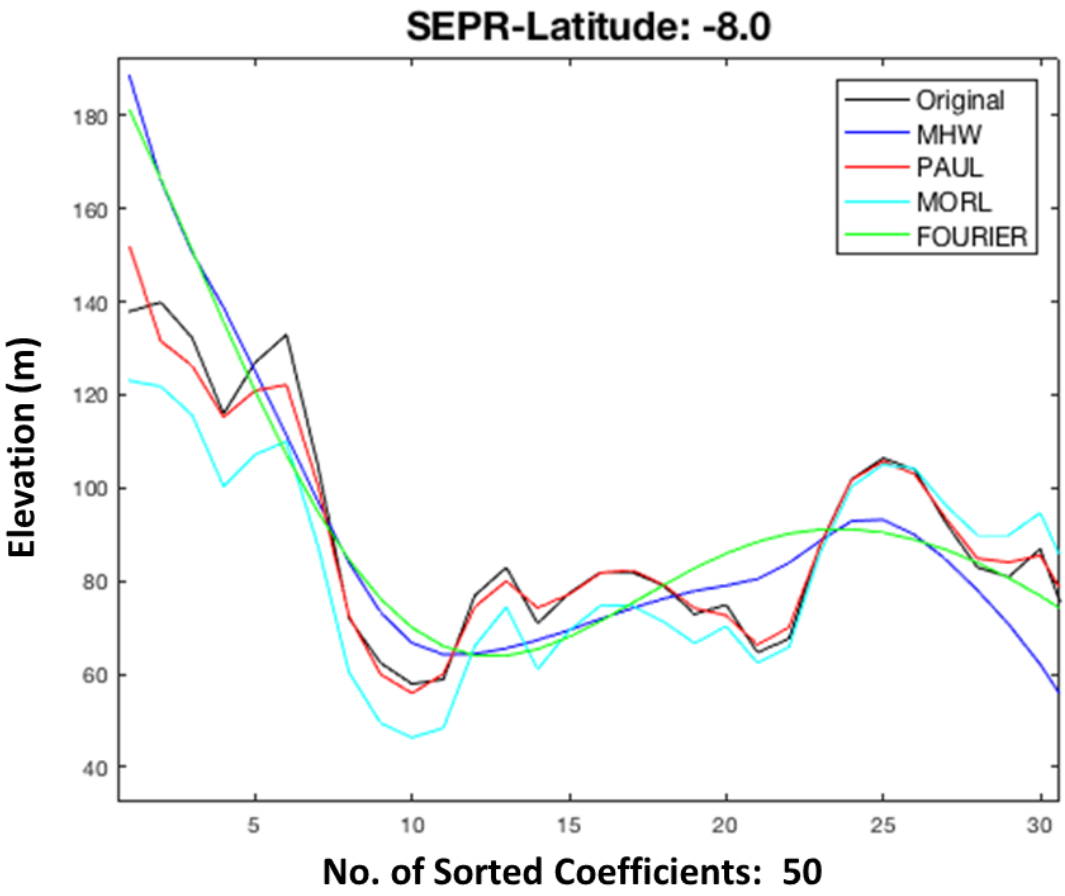

Figure 4.16 1D Signal Reconstruction

Reconstruction of the first 60 terms of the original signal (black line) by the MHW (blue line), Paul wavelet (red line), Morlet wavelet (cyan line) and FT (green line).

Visibly, it is apparent that FT is much smoother than the three wavelet reconstructions. The MHW, although closer in shape to the original signal is much smoother than the Morlet and Paul wavelets. It is important to state that although 60 coefficients are used for each basis function in figure 4.16, that is only a small percentage compared to the over 1500 data points used in the transect. Further, the plot is only showing a portion of

the entire transect. RMSE plots are presented to better discriminate between them (figure 4.17).

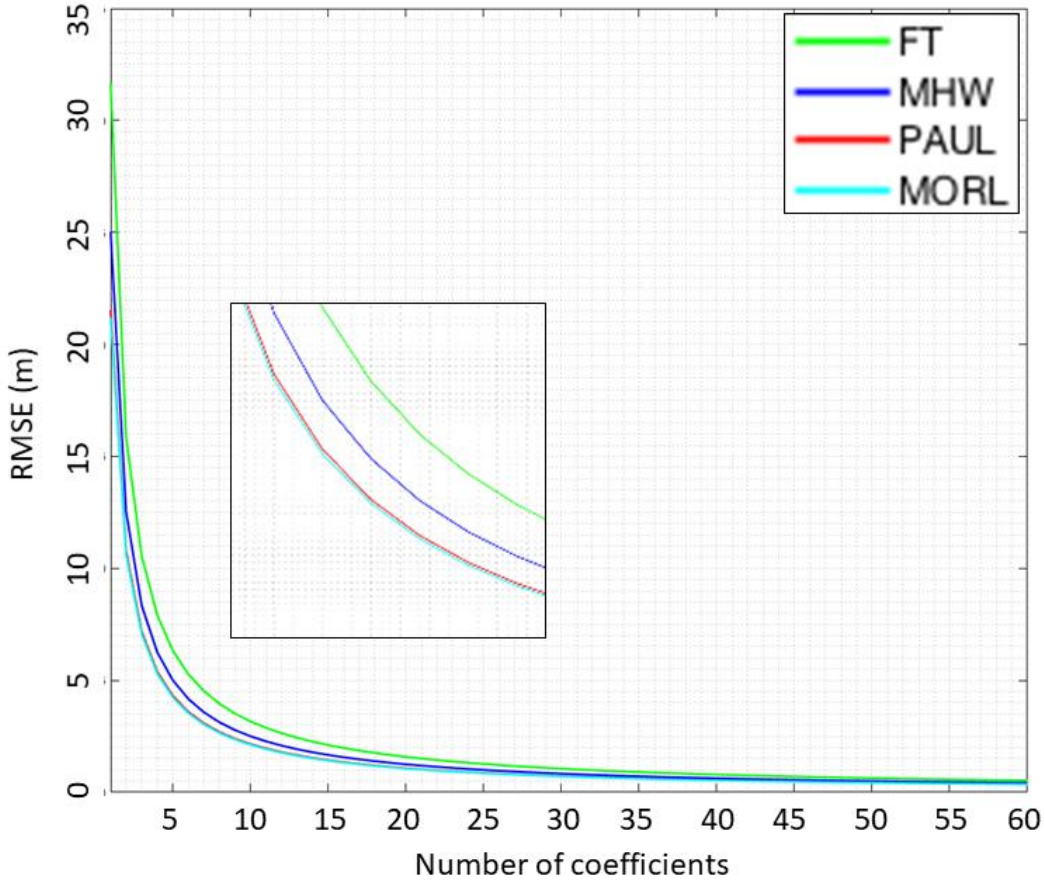

Figure 4.17 Root Mean Square Error of the 1D signal reconstructions

RMSE computed for only the first 60 terms.

Table 4.1 Student t-test values of the Root Mean Square Error

(1D dataset) comparison between each transform.

	Null Hypothesis 0 – Accept 1 – Reject	P (Level of Confidence)	CONFIDENCE INTERVAL LOWER LIMIT	CONFIDENCE INTERVAL UPPER LIMIT
MHW & FT	0	0.4990	-2.0264	0.9926
PAUL & FT	0	0.2772	-2.2216	0.6426
MORLET & FT	0	0.2595	-2.2406	0.6096

Figure 4.17 demonstrates that for the first 60 terms, each of the three tested wavelets outperformed the FT by producing lower RMS error. Per table 4.1, however, a student t-test calculation reveals that there is no statistical difference between the individual transform reconstructions as evidenced by the acceptance of the null-hypothesis (Thomson and Emery, 1998). Nonetheless, the FT is outperformed.

The examination of the transforms continued with a 2D area in the same region. For this test, one specific seamount (-8.45 S, -107.63 E) was isolated. Using the same methodology, a matrix padded with zeros and increasing coefficients was produced and then RMS error was computed.

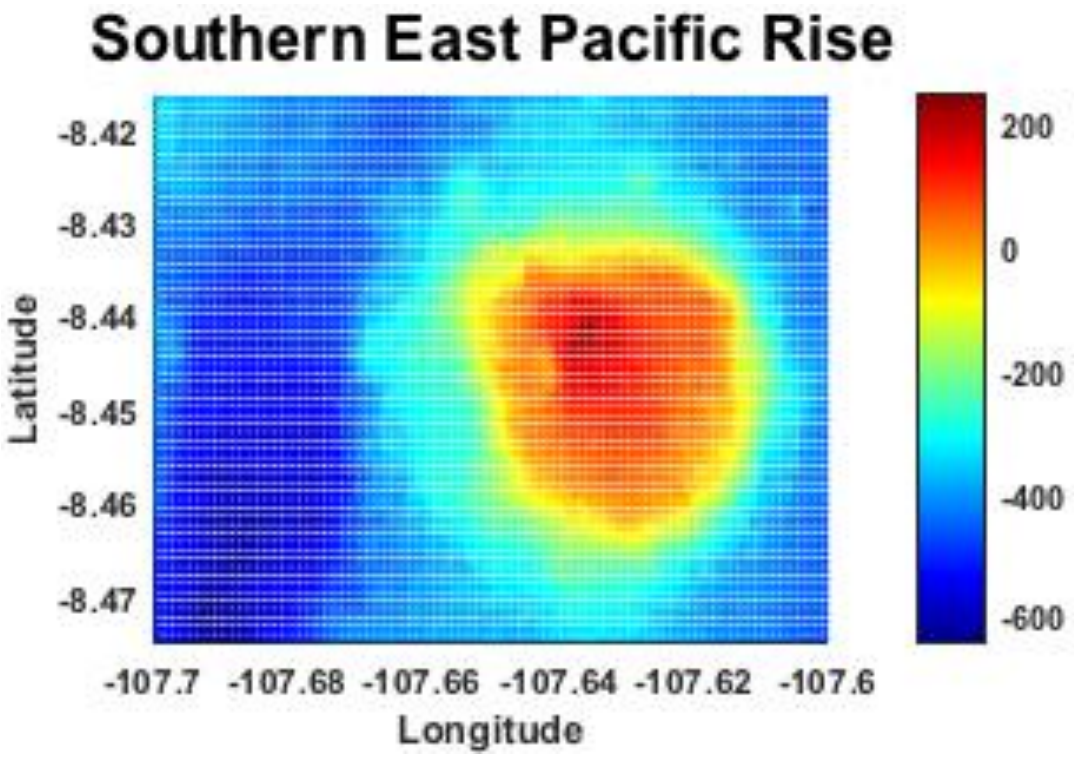

Figure 4.18 Seamount from the SEPR Region.

Untransformed data plot of the seamount in the SEPR region at -8.45 S, -107.63 E. The accompanying color bar represents height in meters, where blue denotes a depression and red elevation, thus zero is the seafloor without feature with units in meters for all similar plots.

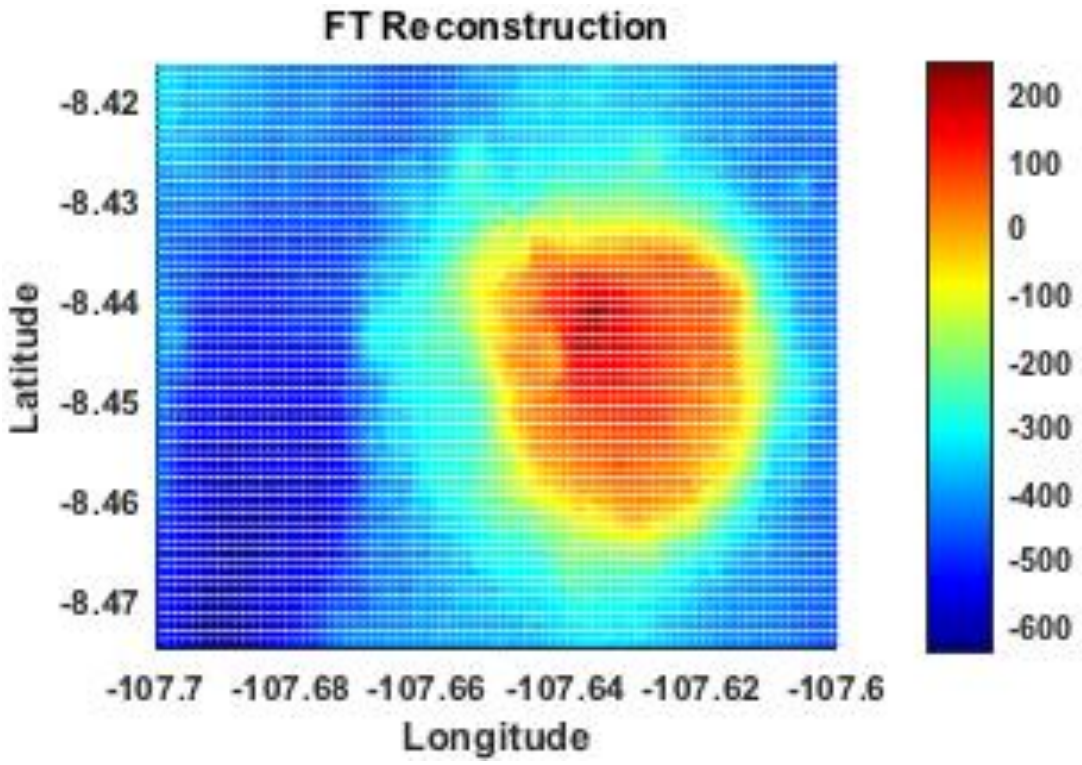

Figure 4.19 FFT reconstruction of the selected seamount.

Note: Units in are in meters.

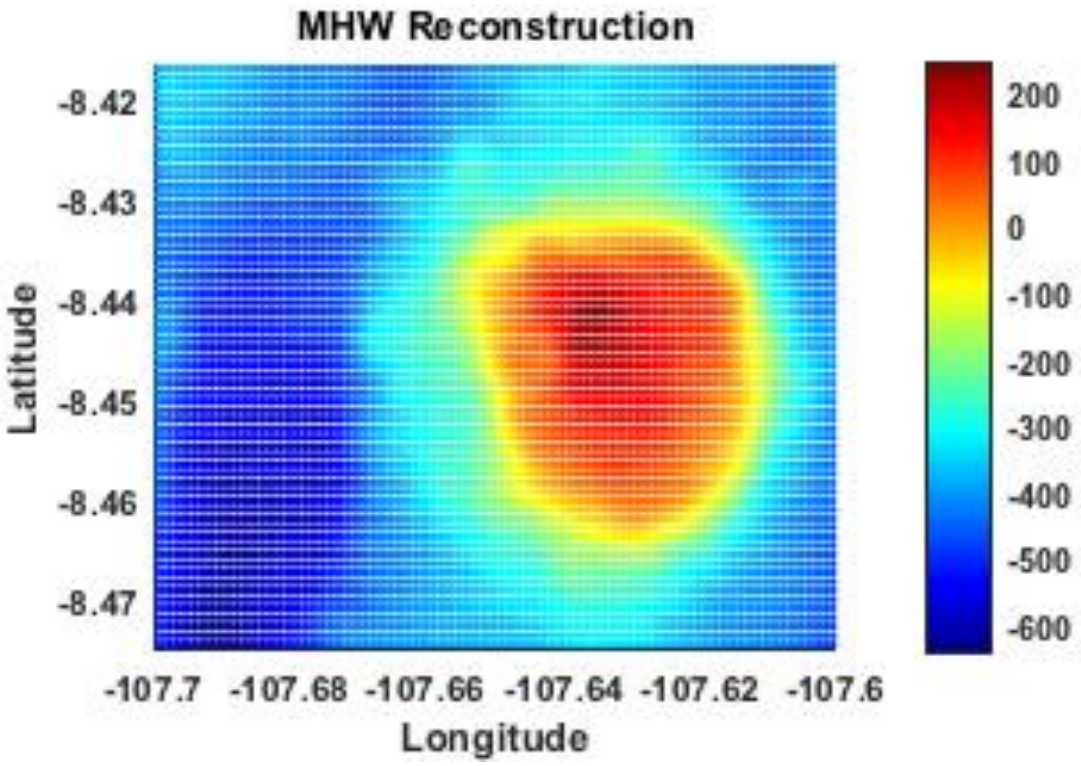

Figure 4.20 MHW reconstruction of the selected seamount.

Note: Units are in meters.

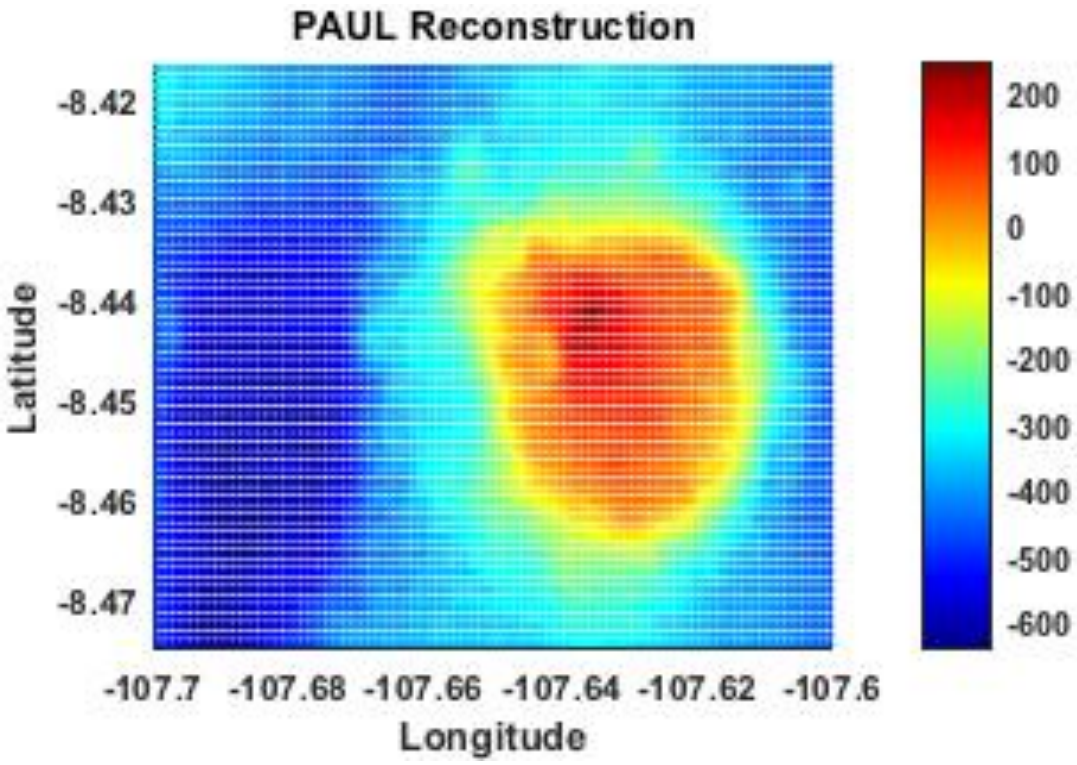

Figure 4.21 Paul reconstruction of the selected seamount.

Note: Units are in meters.

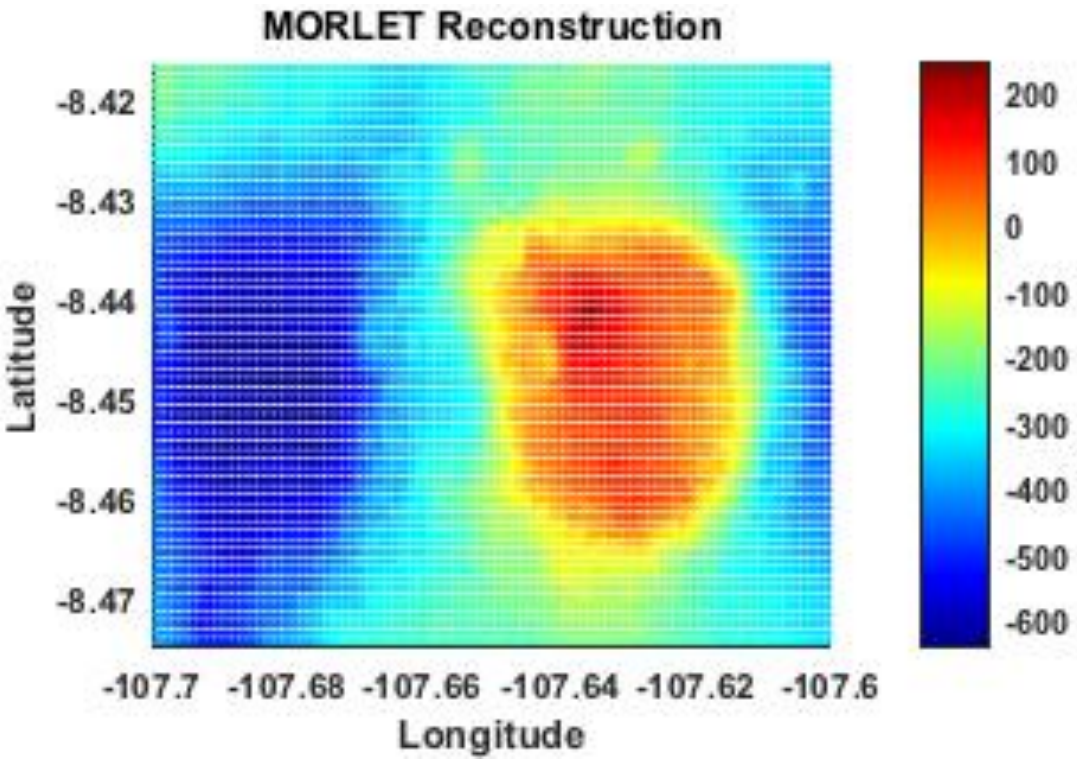

Figure 4.22 Morlet reconstruction of the selected seamount.

Note: Units are in meters.

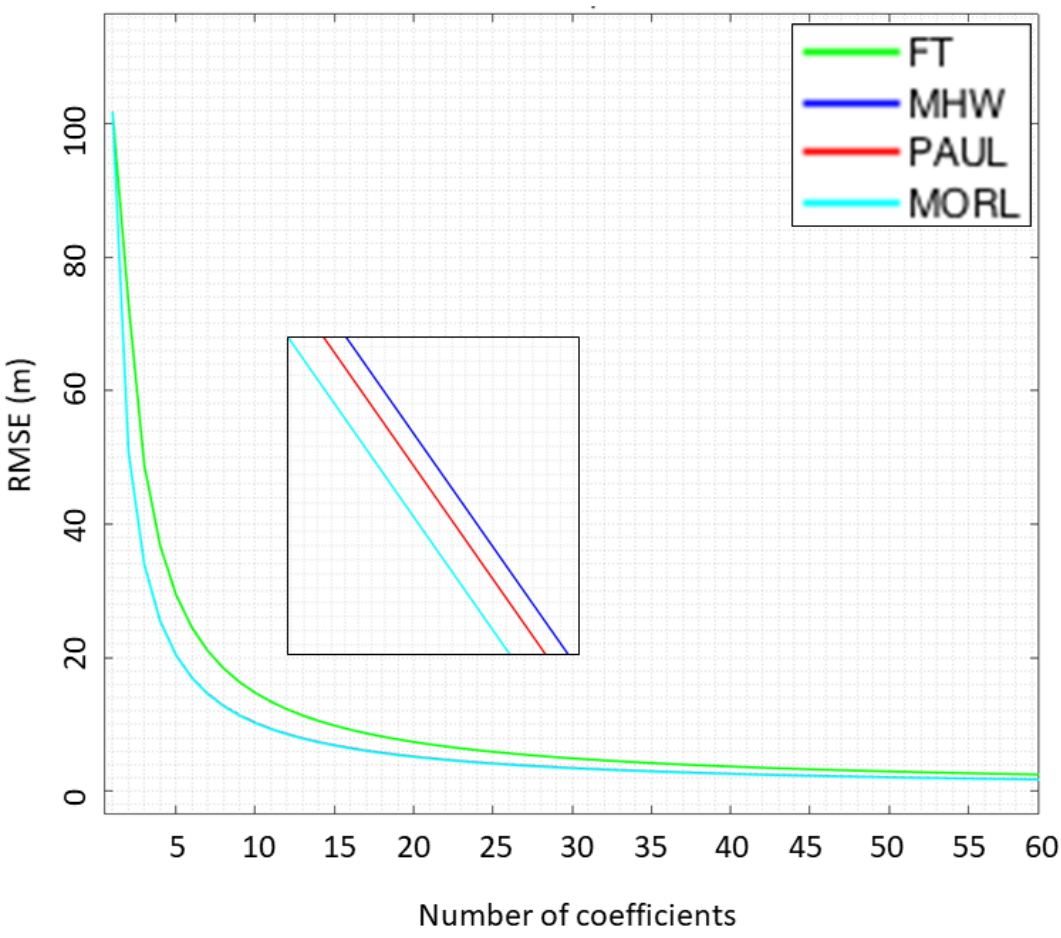

Figure 4.23 Root Mean Square Error of the 2D signal reconstructions.

Note: Only the first 60 terms are used in the computation.

Table 4.2 Student t-test values of the Root Mean Square Error (2D dataset)

	Null Hypothesis 0 – Accept 1 – Reject	**P (Level of Confidence)**	**CONFIDENCE INTERVAL LOWER LIMIT**	**CONFIDENCE INTERVAL UPPER LIMIT**
MHW & FT	0	0.3519	-8.4918	3.0461
PAUL & FT	0	0.3496	-8.5050	3.0331
MORLET & FT	0	0.3461	-8.5252	3.0133

Performances of the transformations varied. Overall, the FT did best in reconstructing the seamount than the wavelets. Within the three wavelets, each performed better than the other in certain parts of the topography, such as the MHW having greater error in the seamount's peak but better resolution elsewhere. The opposite was true for the Paul and Morlet wavelets. However, as is seen in figure 4.23, term-by-term reconstruction errors favored the wavelets. Further, a student t-test again accepted the null-hypothesis, showing little statistical significance between the wavelets and the FT. This completed initial testing of the performance of wavelets and the FT.

4.10 Wavelet and FT calculation of potential anomalies

With initial deconstruction/reconstruction of a signal via wavelets and the FT completed, testing of the wavelet transforms and FT of the gravitational potential commenced. For the FT, the solution from Parker (1973) was used (equation 2.48, here). For the FT[MHW], equation 4.66 was used. Numerical solutions for the MHW, Morlet (equation 4.74) and Paul wavelet (equation 4.77) were applied. It is important to first note that a comparison between a straight numerical approximation of the MHW transformation of the gravitational potential and the closed-form solution (part analytical, part numerical) of the FT[MHW] of the gravitational potential is made. Later, a straight numerical approach to the FT[MHW] is also statistically compared. The particular data set is a 2D area consisting of the same two adjacent seamounts tested in the 1D case. Topographical heights are entered into the formulas and then reconstructed. Figures 4.24-4.29 were computed utilizing all coefficients.

Note

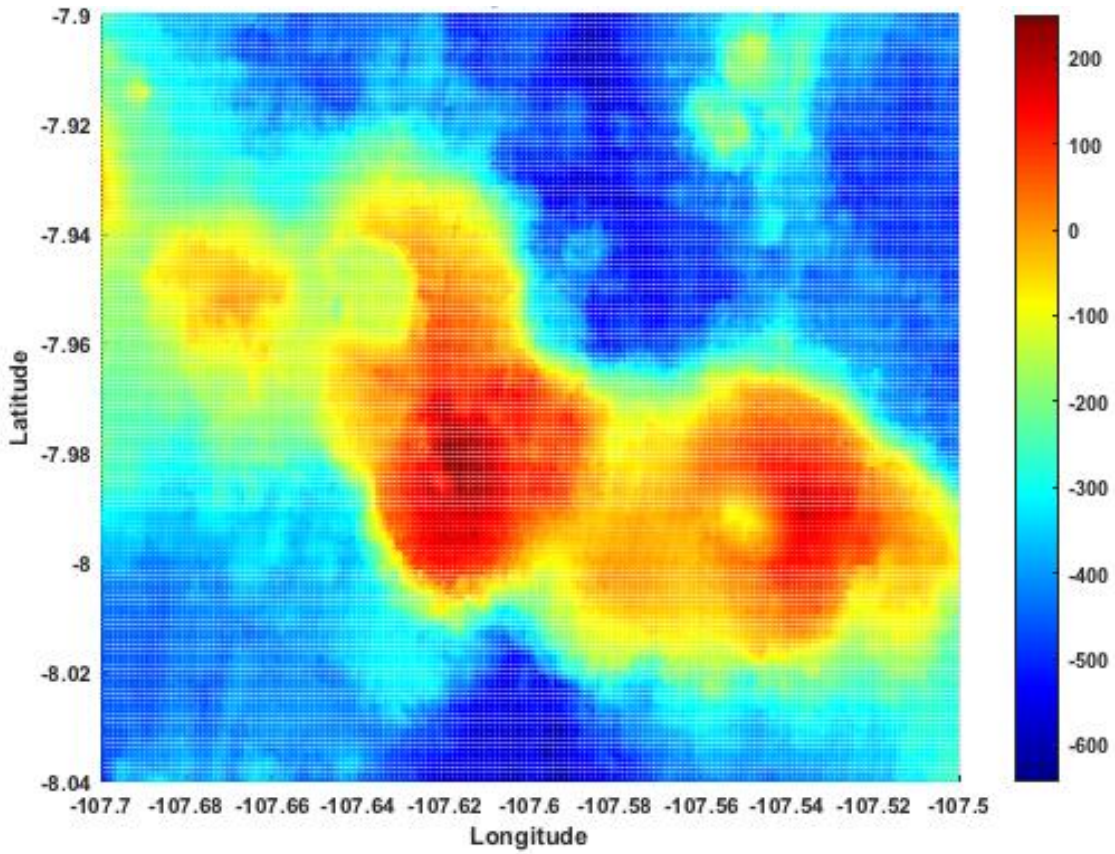

Figure 4.24 Two adjacent seamounts in the SEPR region

Note: Units are in meters.

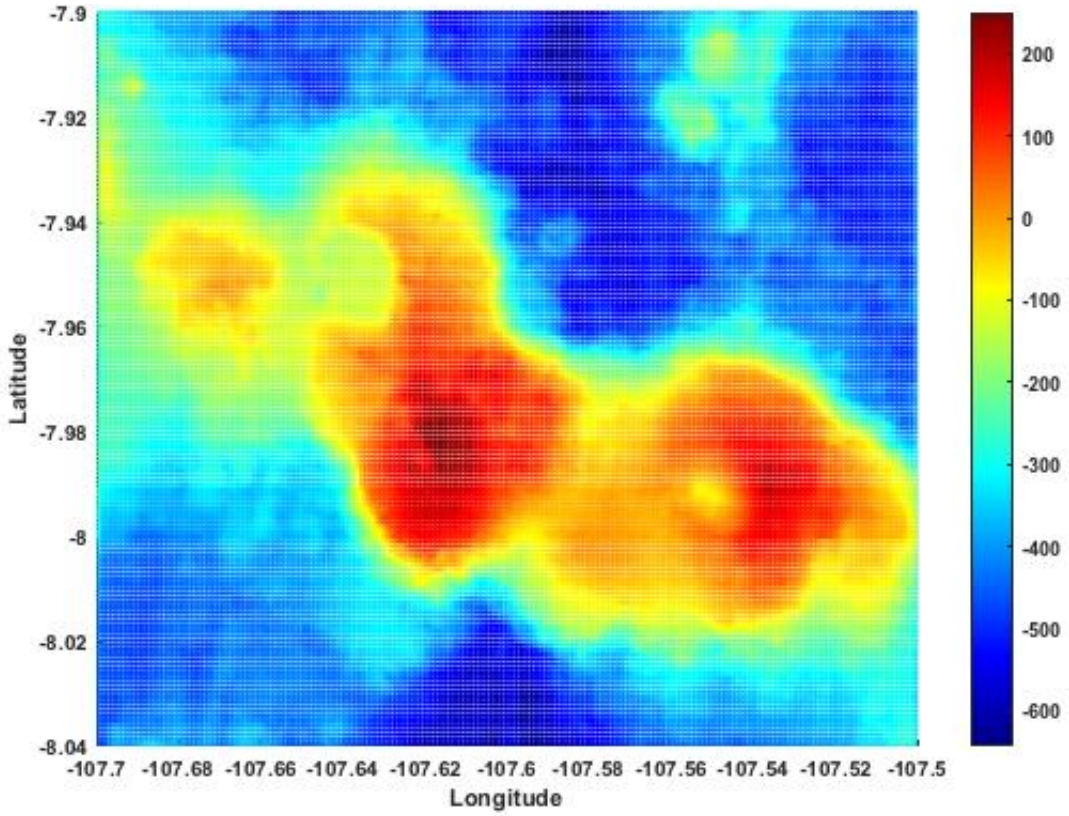

Figure 4.25 FT reconstruction of the seamounts

Note: Units are in meters.

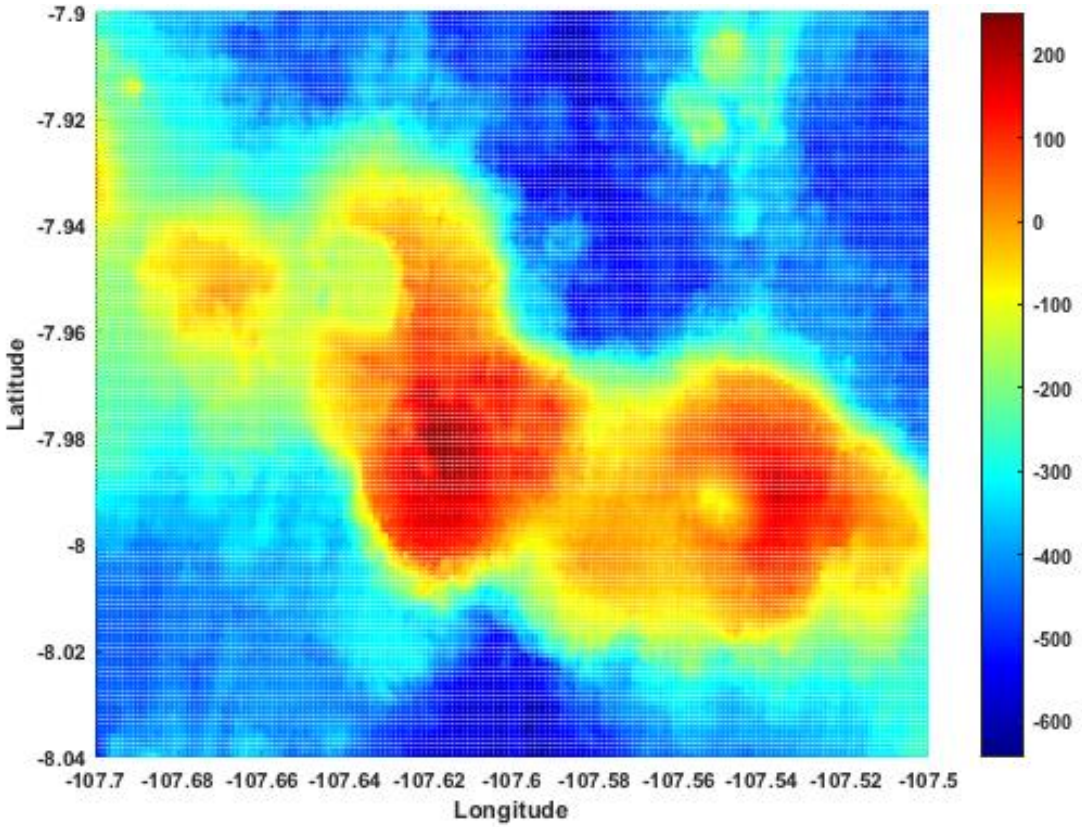

Figure 4.26 MHW reconstruction of the seamounts.

Note: Units are in meters.

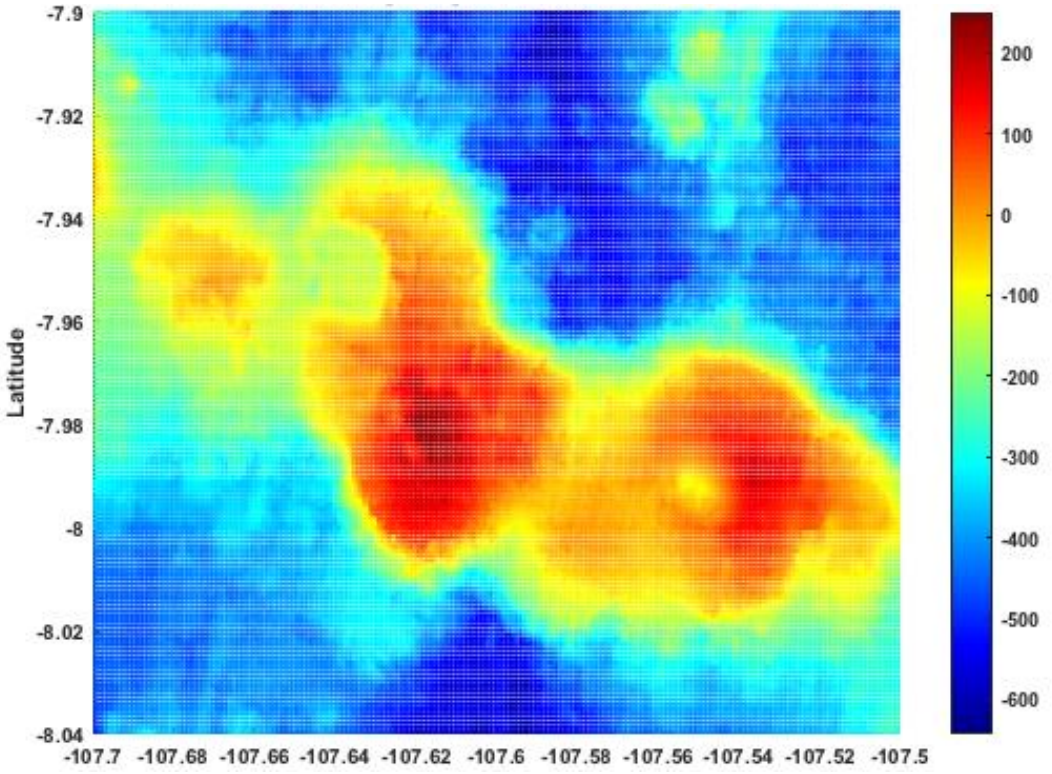

Figure 4.27 FT[MHW] reconstruction of the seamounts

Note: Units are in meters.

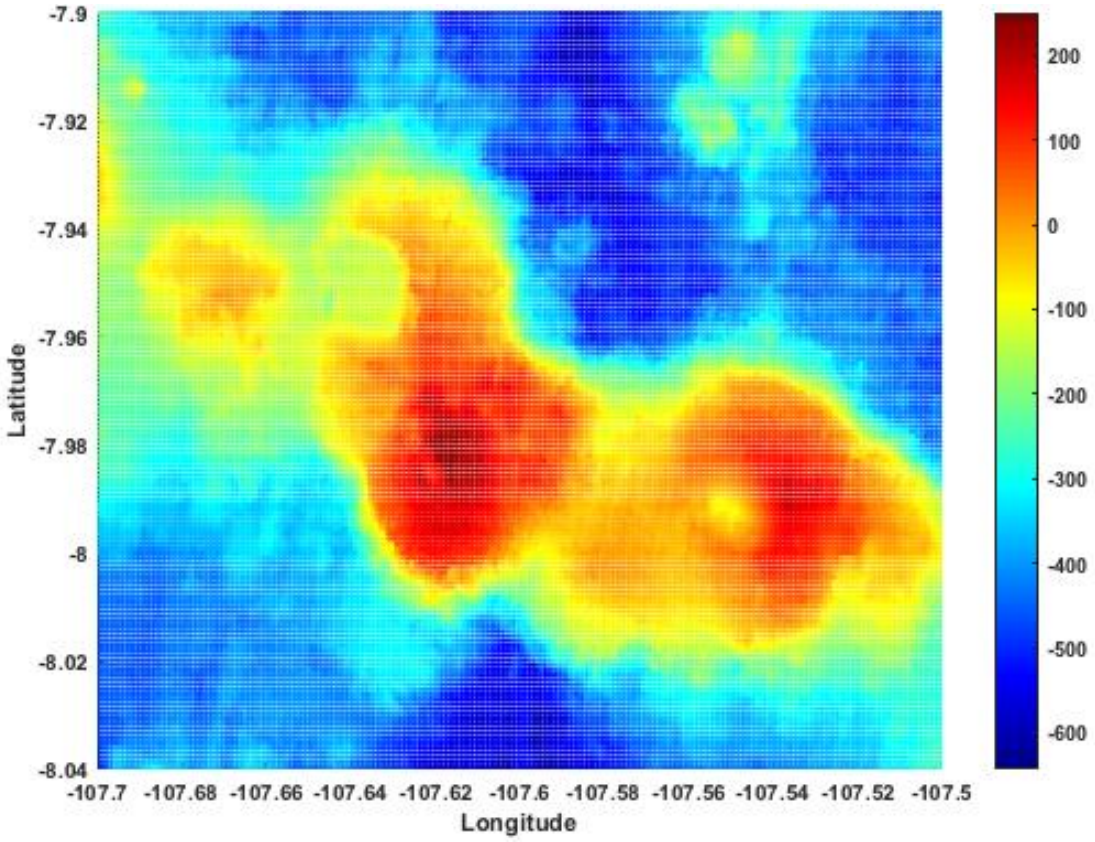

Figure 4.28 Paul reconstruction of the seamounts

Note: Units are in meters.

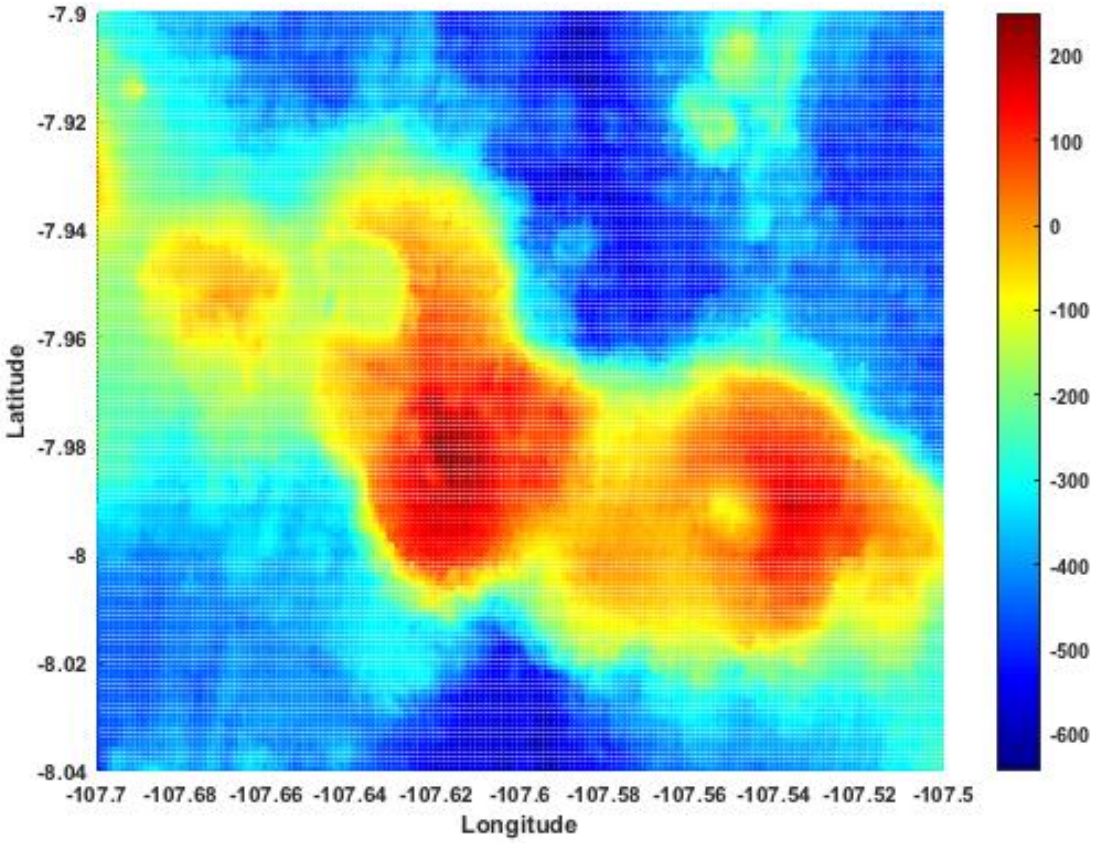

Figure 4.29 Morlet reconstruction of the seamounts

Note: Units are in meters.

Some loss in resolution was detected in the FT reconstruction but not in the wavelets. Overall, the wavelets maintained a slight edge in reconstruction when compared to the original untransformed plot. However, due to the size of the 2D dataset and computational limitations, a term-by-term reconstruction could not be made and thus a RMS error analysis could not be produced either. A simple percent error between the dataset and transformed data has to suffice due to this circumstance.

Note: As the FT[MHW] is a FT, the derivative rule for Fourier transforms should still apply. As such, similar to FT[Δg], FT[MHW][Δg] can be easily computed by simple multiplication of the FT[MHW] of the gravitational potential by the wavenumber k. As such, end-to-end prediction was shown. Similar plots were produced for the FT and FT[MHW] of the gravity anomaly as with the potentials, with no significant difference. The wavenumber "k" was given the arbitrary value of 2 for this case.

4.11 End to End Prediction

Prior to demonstrating end-to-end prediction, we must first compute a key component, "upward continuation." Blakely, 1995, defines upward continuation as the transformation of a potential field determined on one surface to another field further away from all sources. It is important to note that Blakely points out that the transformation of upward continuation acts to attenuate anomalies with respect to wavelength. Great care should be taken to recognize this point, as it is also pointed out by Sandwell and Smith (1997) as one of two key factors that imposes limits on accuracy and resolution of gravity field recovery from satellite altimetry data (ocean depth of ~4 km attenuates short wavelength gravity signals). The other limiting factor according to Sandwell and Smith results from short wavelength noise originating from ocean surface waves. From Blakely, the upward continuation integral is expressed as:

$$U(x,y,z_0-\Delta z)=\frac{\Delta z}{2\pi}\int_{-\infty}^{\infty}\int_{-\infty}^{\infty}\frac{U(x',y',z_0)}{[(x-x')^2+(y-y')^2+\Delta z^2]^{3/2}}dx'dy',\Delta z>0 \qquad (4.92)$$

Blakely then notes that the upward continuation may be expressed as a convolution in two-dimensions.

$$U(x, y, z_0 - \Delta z) = \int_{-\infty}^{\infty} \int_{-\infty}^{\infty} U(x', y', z_0)\, \psi_u(x - x', y - y', \Delta z) dx' dy' \qquad (4.93)$$

where,

$$\psi_u(x, y, \Delta z) = \frac{\Delta z}{2\pi} \frac{1}{(x^2 + y^2 + \Delta z^2)^{3/2}} \qquad (4.94)$$

Blakely then represents the convolution using the following formula:

$$\mathcal{F}[U_u] = \mathcal{F}[U]\mathcal{F}[\psi_u], \qquad (4.95)$$

where ψ_u is the upward-continued field. Per Blakely, the analytical computation of the FT of the upward continuation field is straight forward. A conversion from Cartesian to cylindrical coordinates is made first resulting in:

$$\mathcal{F}[\psi_u] = \frac{-1}{2\pi} \frac{\partial}{\partial \Delta z} \mathcal{F}\left[\frac{1}{r}\right] \qquad (4.96)$$

where 1/r is the monopole and whose FT has already been derived in Bracewell, 1967. We may now express the FT of the upward-continued field as:

$$\mathcal{F}[\psi_u] = e^{-\Delta z|k|}, \Delta z > 0 \qquad (4.97)$$

End-to-end prediction is show in Sandwell and Smith, 1997 appendix A. Here we will follow that procedure albeit in the wavelet domain. From equation 4.95, we may extrapolate the continuous-wavelet transform approach.

$$\mathcal{W}[\psi_u] = \frac{-1}{2\pi} \frac{\partial}{\partial \Delta z} \mathcal{W}\left[\frac{1}{r}\right] \qquad (4.98)$$

The continuous wavelet transform of the monopole, will be set up later for each of the three tested wavelets, MHW, Paul and Morlet wavelets. Similar to Fourier convolution theorem, there exists a similar theorem for continuous wavelets. (Antonio F. Perez-Rendon, 2004) derive and provide the proof of the existence of such a theorem.

$$\hat{g}^{\psi_g}(a, b) = \frac{1}{\sqrt{a}} \left(\hat{f}^{\psi_f} \otimes_2 \hat{h}^{\psi_h}\right)(a, b) \qquad (4.99)$$

where $\hat{f}^{\psi_f} \otimes_2 \hat{h}^{\psi_h}$ denotes the convolution of the second variable of two wavelet transformed functions, $\hat{g}^{\psi_g}(a, b)$ is said convolution, a is scale and b is position (translation). We may now express the continuous wavelet transform of the upward continuation (equivalent to equation 4.95) as:

$$W[U_u] = \frac{1}{\sqrt{a}} W[U] W[\psi_u], \tag{4.100}$$

We previously numerically solved for W[U] using three wavelets; and, a numerical solution will also be required for the wavelet transform of the upward-continued field (equation 4.98). Sandwell and Smith equate the gravity anomaly to the potential's vertical derivative and then define the slope of the geoid in the x-direction (η) and in the y-direction (ξ). The three quantities are related to one another using Laplace's equation. This differential equation may be reduced to an algebraic formula, per Haxby et al. (1983), by taking its Fourier Transform. We may similarly do so with a continuous wavelet transform. From Laplace's equation we have,

$$\frac{\partial \Delta g}{\partial z} = -g_0 \left(\frac{\partial \eta}{\partial x} + \frac{\partial \xi}{\partial y} \right) \tag{4.101}$$

The continuous wavelet transform of equation 4.101 is then (equation A8 from Sandwell and Smith, 1997),

$$\mathcal{W}\left[\frac{\partial \Delta g(a,b,z)}{\partial z} \right] = -g_0 \left[\mathcal{W}\big(\eta(a,b)\big) + \mathcal{W}\big(\xi(a,b)\big) \right] \tag{4.102}$$

Utilizing equation 4.100, we may state

$$\Delta g(a, b, z) = \frac{1}{\sqrt{a}} \Delta g(a, b, 0)\, W[\psi_u] \tag{4.103}$$

In the Fourier domain, we would take the derivative of the Fourier equivalent of equation 4.98, evaluate at z=0 and thus relate the FT of the gravity anomaly to the sum of the

vertical deflection components. To begin this process in the wavelet domain, we will need to first solve for the CWT of the monopole.

4.12 CWT (2D) of the Monopole

4.12.1 Mexican Hat Wavelet

$$\psi_{MHW}\left[\frac{1}{r}\right] = \int_{-\infty}^{\infty}\int_{-\infty}^{\infty} \frac{1}{[x^2+y^2+(z_0-z')^2]^{1/2}}\left(1-\frac{1}{2}\frac{(x^2+y^2)}{\sigma^2}\right) e^{-(x^2+y^2)/2\sigma^2} dxdy \quad (4.104)$$

Note: In order to prevent confusion with scale (a) and an upcoming term (a), scale is represented as the Greek letter sigma. See figure 2.2 for a refresher on the geometry of this problem. After conversion to cylindrical coordinates with the following substitutions, x=acosθ, y=sinθ and $w^2 = (z_0\text{-}z')^2$, we have,

$$\psi_{MHW}\left[\frac{1}{r}\right] = \int_{0}^{2\pi}\int_{0}^{\infty} \frac{1}{\sqrt{a^2+w^2}}\left(1-\frac{1}{2}\frac{(a^2)}{\sigma^2}\right) e^{-a^2/2\sigma^2} a\, dad\theta \quad (4.105)$$

With all thetas going away, the integral from 0 to 2pi results in a 2pi in front of the equation:

$$\psi_{MHW}\left[\frac{1}{r}\right] = 2\pi\int_{0}^{\infty} \frac{1}{\sqrt{a^2+w^2}}\left(1-\frac{1}{2}\frac{(a^2)}{\sigma^2}\right) e^{-a^2/2\sigma^2} a\, da \quad (4.106)$$

Equation 4.101 does not have an apparent analytical solution and must be solved for numerically.

4.12.2 Morlet Wavelet

We will similarly set up the Morlet problem for the monopole.

$$\psi_{Morlet}\left[\frac{1}{r}\right] = \int_{-\infty}^{\infty}\int_{-\infty}^{\infty} \frac{1}{[x^2+y^2+(z_0-z')^2]^{1/2}} \pi^{-1/4}\, e^{i\omega_0(x+y)} e^{-(x^2+y^2)/2\sigma^2} dxdy \quad (4.107)$$

where, ω_0 is frequency with a default value of six in MATLAB. After conversion to cylindrical coordinates, we have

$$\psi_{Morlet}\left[\frac{1}{r}\right] = \int_0^{2\pi}\int_0^{\infty} \frac{1}{\sqrt{a^2+w^2}} \pi^{-1/4}\, e^{i\omega_0 a(cos\theta+sin\theta)} e^{-a^2/2\sigma^2} a\, da d\theta \quad (4.108)$$

Rearranging, we have

$$\psi_{Morlet}\left[\frac{1}{r}\right] = \pi^{-1/4}\int_0^{\infty} \frac{e^{-a^2/2\sigma^2}}{\sqrt{a^2+w^2}} a\, da \left[\int_0^{2\pi} e^{i\omega_0 a(cos\theta+sin\theta)}\, d\theta\right] \quad (4.109)$$

Again, we will have to solve the problem numerically.

4.12.3 Paul Wavelet

We similarly apply this wavelet to the monopole potential.

$$\psi_{Paul}\left[\frac{1}{r}\right] = \int_{-\infty}^{\infty}\int_{-\infty}^{\infty} \frac{1}{[x^2+y^2+(z_0-z')^2]^{1/2}} \frac{2^m i^m m!}{\sqrt{\pi(2m)!}} \big(1-i(x+1)\big)^{-(m+1)} dxdy \quad (4.110)$$

Here, m is the order of the wavelet. MATLAB uses a default value of m=4.

Setting m=4 and converting to cylindrical results in

$$\psi_{Paul}\left[\frac{1}{r}\right] = \frac{384}{\sqrt{\pi\cdot 8!}}\int_0^{2\pi}\int_0^{\infty} \frac{1}{\sqrt{a^2+w^2}} \big(1-ai(cos\theta+sin\theta)\big)^{-5} a\, da d\theta \quad (4.111)$$

Rearranging, we are left with,

$$\psi_{Paul}\left[\frac{1}{r}\right] = \frac{384}{\sqrt{\pi\cdot 8!}}\int_0^{\infty} \frac{a\, da}{\sqrt{a^2+w^2}} \left[\int_0^{2\pi} \big(1-ai(cos\theta+sin\theta)\big)^{-5}\, d\theta\right] \quad (4.112)$$

A numerical solution will need to be computed here as well.

Once the numerical computations of the monopole potential are computed, we may proceed back to equation 4.98 to solve for the wavelet transform of the upward-continued field. Taking the derivative with respect to z of equation 4.103 and then evaluating at z=0

$$-g_0\big[\mathcal{W}\big(\eta(a,b)\big) + \mathcal{W}\big(\xi(a,b)\big)\big] = \frac{1}{\sqrt{a}}\Delta g(a,b,0)\, W[\psi_u] \quad (4.113)$$

Solving for Δg(a,b,0) we get,

$$\Delta g(a,b,0) = \frac{-g_0\sqrt{a}[\mathcal{W}(\eta(a,b))+\mathcal{W}(\xi(a,b))]}{\frac{\partial(\mathcal{W}[\psi_u])}{\partial z}\Big|_{z=0}} \qquad (4.114)$$

We have now algebraically related the continuous-wavelet transform of the gravity anomaly to the sum of the CWT of the two components of vertical deflection. As with Sandwell and Smith, 1997, the computation of gravity anomalies from a dense network of satellite altimeter geoid height profiles may be done through the construction of a grid composed of east-west and north-south vertical deflections. This procedure is outlined in Sandwell and Smith, 1997 Appendix B. We then take the CWT of the grids, compute the addition and multiplications of the right-hand-side of equation 4.114 and then take the inverse CWT, resulting in the gravity anomaly. As noted at the end of Appendix A of Sandwell and Smith, 1997, the long wavelength gravity may be recovered by adding back the spherical harmonic gravity model to the gridded gravity values.

Further, noted midway through their Appendix A, Sandwell and Smith, 1997 state that vertical gravity calculation of their equation A6, (here equation 4.101) does not produce edge effects, whereas the FT of the gravity field could produce significant edge effects. The question here is, will the CWT of the gravity field produce edge effects and if so, will they be equivalent to, larger or smaller?

4.13 Downward Continuation

Taking gravity and inverting it to topography will require a downward continuity calculation. Downward continuity is the continuation of measured data to regions that are closer to the source, assuming that are no sources in the continued region actually

exist, which is helpful as it would act to accentuate source distribution details (Blakely, 1995). Downward continuation, however, is considered to be unstable as it is an unsmoothing operator, as opposed to smoothing from the upward continuation calculation (Blakely, 1995). Per Blakely, the downward continuation is the inverse of the upward continuation and is expressed as:

$$\mathcal{F}[U] = \mathcal{F}[U_u]\mathcal{F}^{-1}[\psi_u] = \mathcal{F}[U_u]e^{+|k|\Delta z} \tag{4.115}$$

It is the exponential, according to Blakely that causes the instability as the shortest wavelengths in the data could be greatly amplified. Despite this risk, numerous downward continuation techniques utilize this method. Per our method of using sparser based functions, in particular wavelets, we can set up an equivalent to equation 4.115 in the wavelet domain by taking the inverse of equation 4.100.

$$W[U] = \frac{1}{\sqrt{a}} W[U_u]W^{-1}[\psi_u], \tag{4.116}$$

4.13.1 Application of Sparser Functions

Although theoretically a formula for downward and upward continuity is presented, the solution to those formulas is not achievable either analytically or numerically due to the integrals of the monopole potentials exploding to infinity very quickly. It is conceivable, though, that a different analytical/numerical approach could be made such as was done with the Mexican Hat wavelet transform applied to the Newtonian potential. That work will be left for future research. As such, downward and upward continuation were both computed in the Fourier domain. A novel methodology was then applied by filtering gravity datasets with wavelets prior to those computations (Maysam Abedi, 2014). Those 2D results are now presented.

The area of interest is a subset of the data seen in figure 4.15 and includes the topography depicted in figures 4.18 and 4.24. The area selected represents an ocean floor with both flat topography and seamounts. However, as the seamounts are not particularly large at only a few hundred meters high, the data was multiplied by a factor of 2.5 in order to enhance the feature heights.

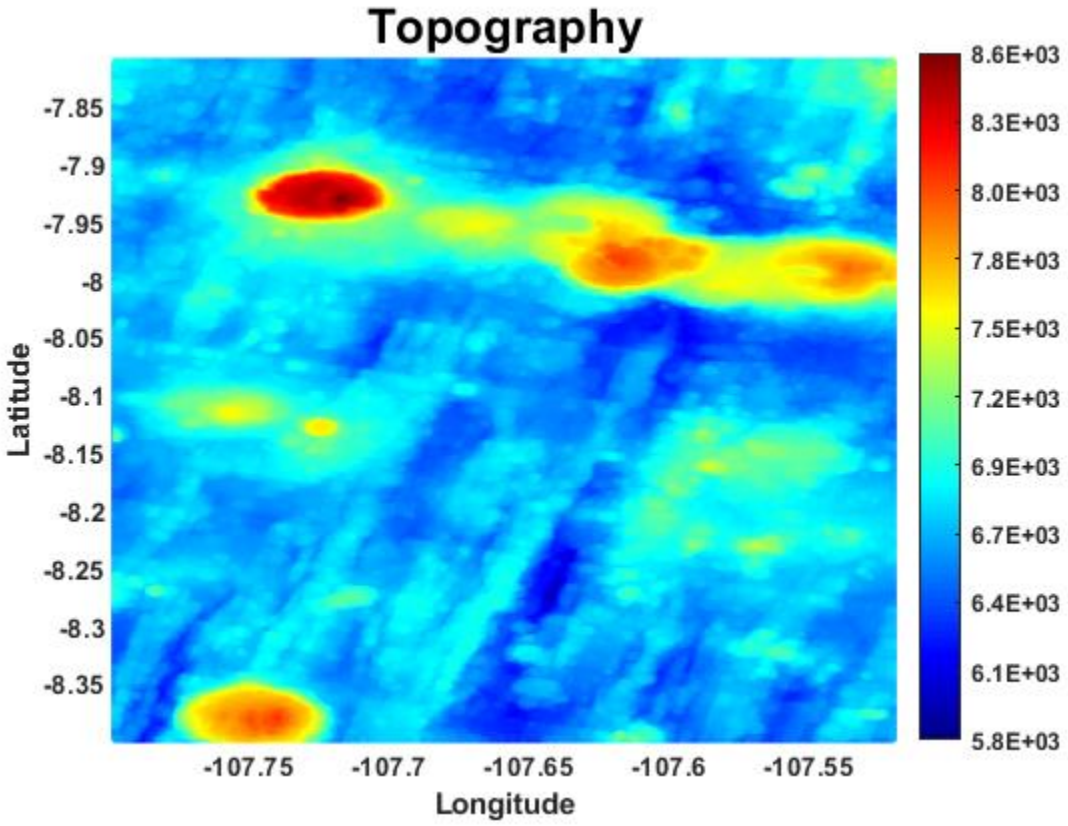

Figure 4.30 Area of study within the SEPR

Note: The accompanying color bar represents height in meters. The seamounts in the upper portion of the plot were previously examined (units in meters).

A study of the whole area represented in figure 4.30 will be examined first followed by a closer look at the two seamounts in the upper right hand corner. The

selected topographical data set is first converted into gravity data following Newton's law via the built in tools of Generic Mapping Tool (GMT) freely available for download from the School of Ocean and Earth Science Technology (SOEST) of the University of Hawaii at the following internet address:

http://gmt.soest.hawaii.edu/

The idea of developing a gravity data set from a highly surveyed and studied region that utilized multibeam SONAR is to obtain as detailed a gravity signal as possible. Once the gravity signal is converted back into topographical data, a clearer picture of the difference between using wavelets and Fourier analysis may be obtained. Conversely, sparse gravity datasets, which is what is collected via satellite over the deep ocean will not be able to produce any discernable differences. Following the Smith and Sandwell "cookbook" for upward and downward continuation, the gravity signal is converted back into topographical data.

For the FFT, this procedure was simple and followed the steps straightaway. For the wavelets, however, these steps needed to be repeated several times. For example, for the dataset shown in figure 4.30, each of the continuous wavelets studied (Mexican Hat, Paul and Morlet) produced thirty-four different scales. MATLAB will determine the number of scales based on the size of the dataset. A larger amount of data results in a higher number of scales. The steps in the cook book, then, were followed 34 times per wavelet, resulting in 34 different solutions, each based on its own scale number. Once all the solutions are collected, MATLAB can inverse transform the individual signals into one solution that moves across all the scales. One of two approached can thus be made. Either look at the inverse wavelet transform across all scales or choose a specific scale.

The choice of choosing a particular scale could reduce error but will require more time in order to determine which works best; and, with increasing number of scales with increasing data set sizes, a method of selecting only a few of the many scales would need to be developed.

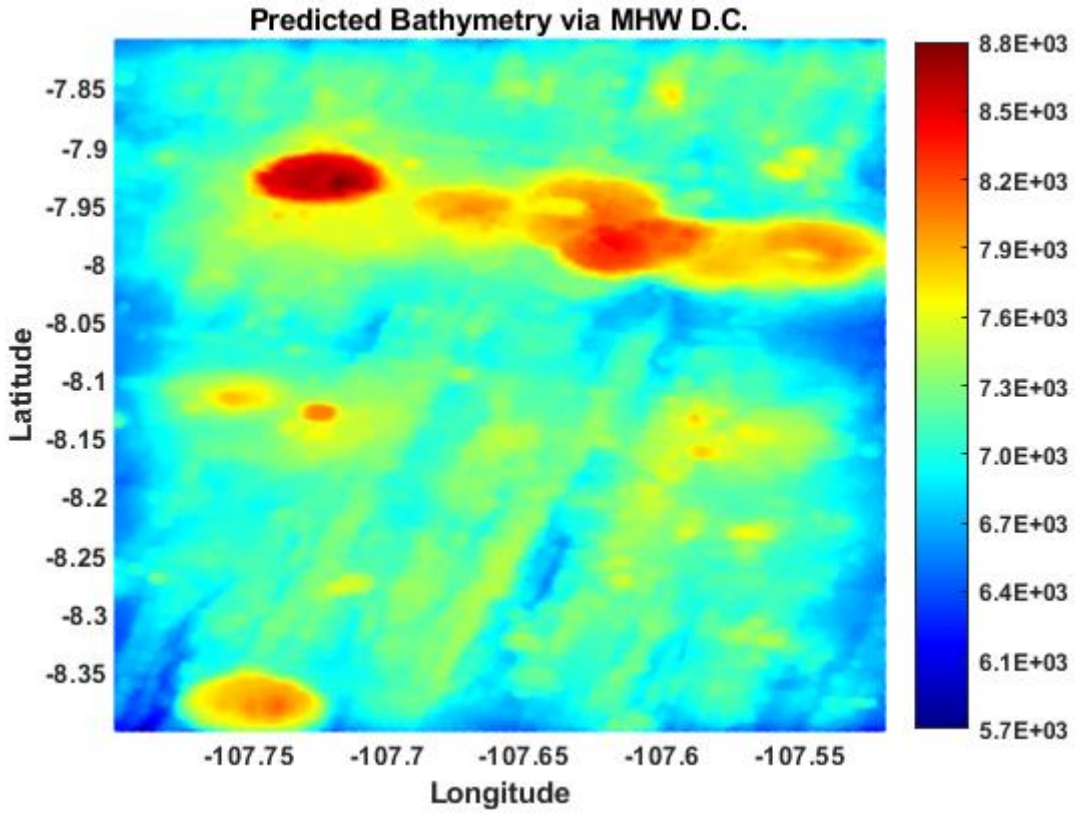

Figure 4.31 MHW predicted bathymetry.

Note: Gravity data wavelet filtered prior to downward continuation (units in meters).

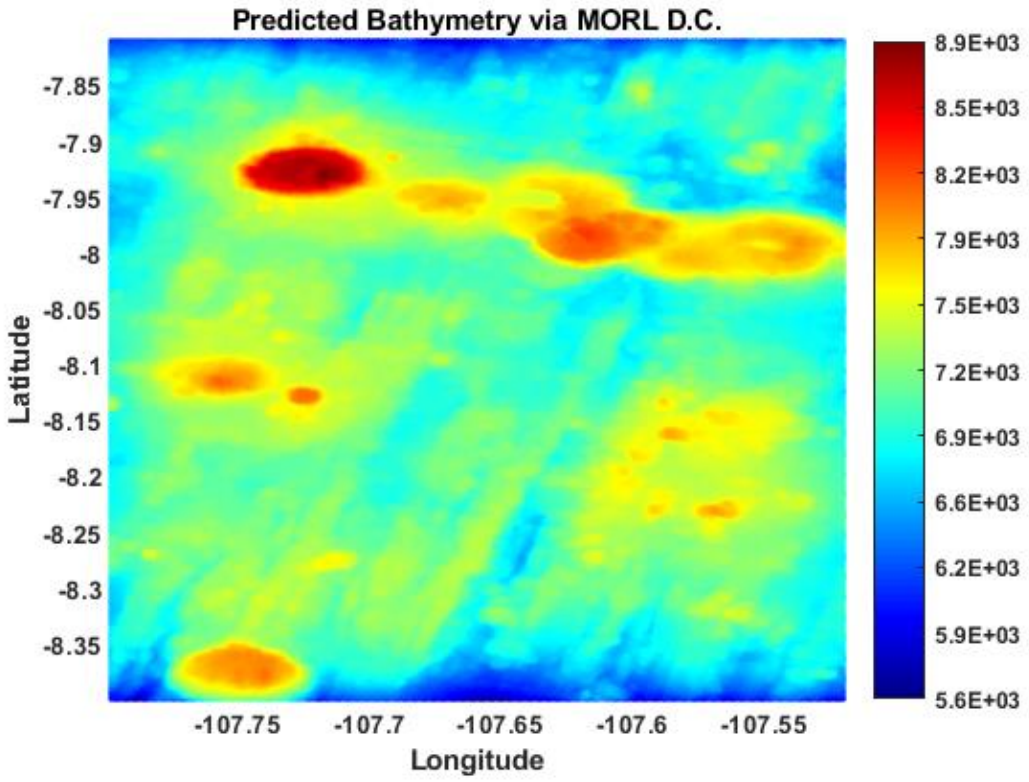

Figure 4.32 Morlet predicted bathymetry.

Note: Gravity data wavelet filtered prior to downward continuation (units in meters).

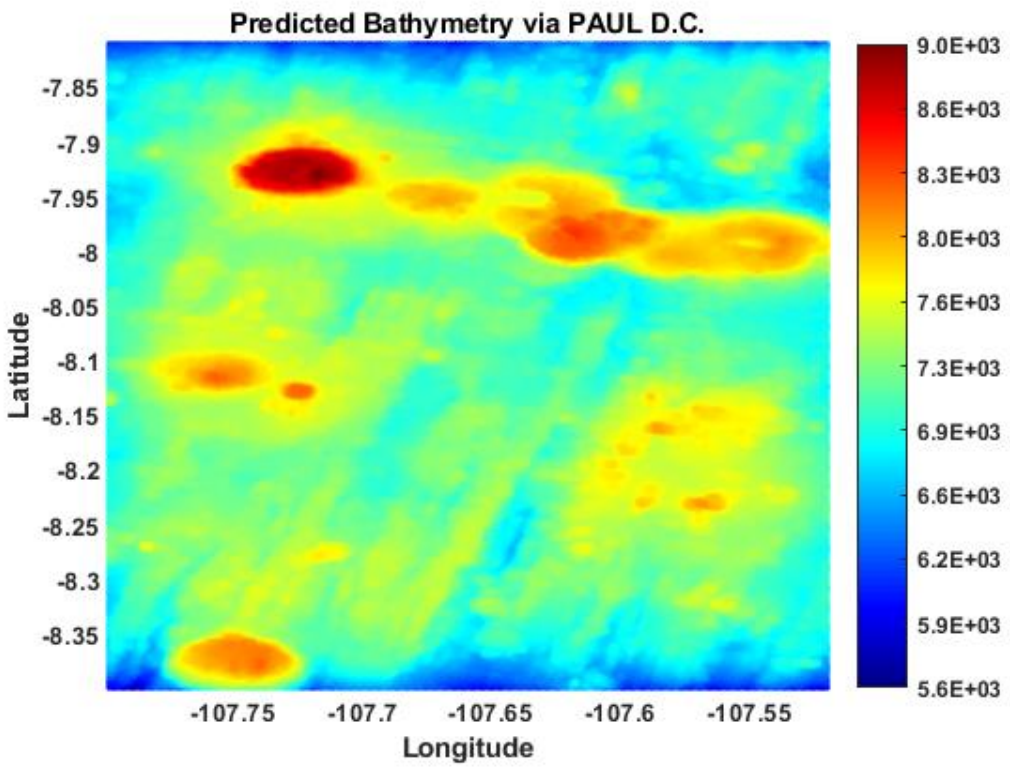

Figure 4.33 Paul predicted bathymetry.

Note: Gravity data wavelet filtered prior to downward continuation (units in meters).

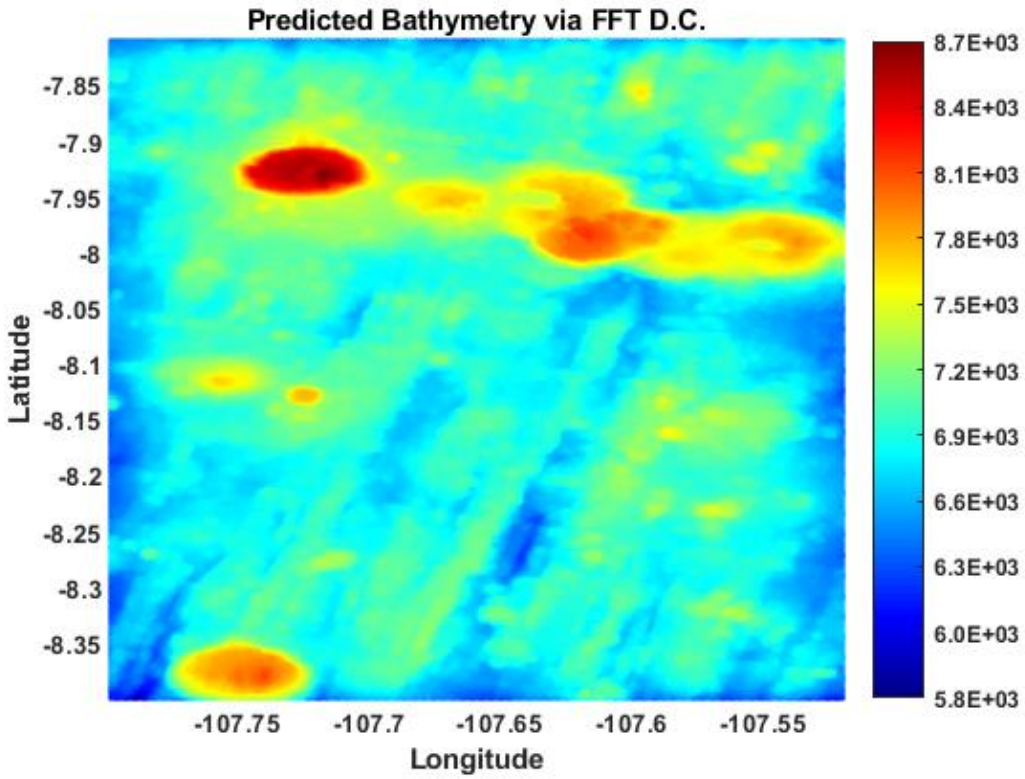

Figure 4.34 FFT predicted bathymetry.

Note: Units in meters.

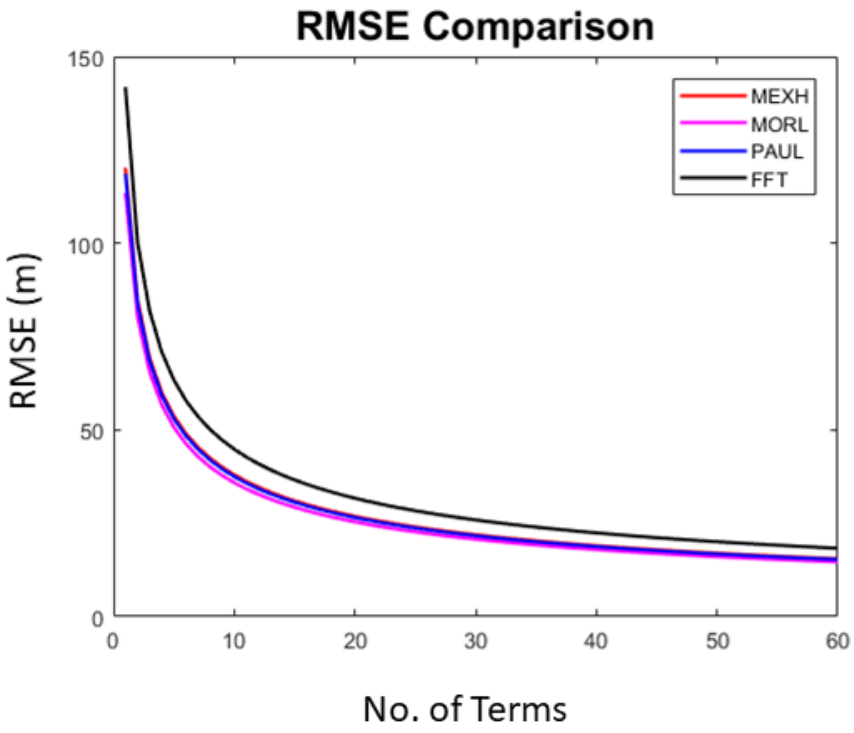

Figure 4.35 Error comparison between tested basis functions

For figures 4.31-4.33, a specific wavelet scale was chosen for each of the tested wavelets. Their error was computed using a standard RMS error formula and then compared to the RMS error of the Fourier solution. Although it is difficult to see any major differences between the solutions, a careful look does reveal subtle improvements in feature details amongst the wavelets over the FFT. Those subtle improvements are further demonstrated in figure 4.35 where RMS error for the wavelets are lower than that of the FFT. Recall that FFTs are great at reproducing flat topography as a flat surface is easily reproduced with a sum of sines and cosines. The region tested (Figure 4.30) has a significant amount of flat terrain with some features in it. The question then is whether the performance of the wavelets will increase or decrease, as compared to the FFT, when

we zoom in on key features of the area, specifically over seamounts where it was hypothesized that wavelets due to their scalability and translation would outperform the FFT.

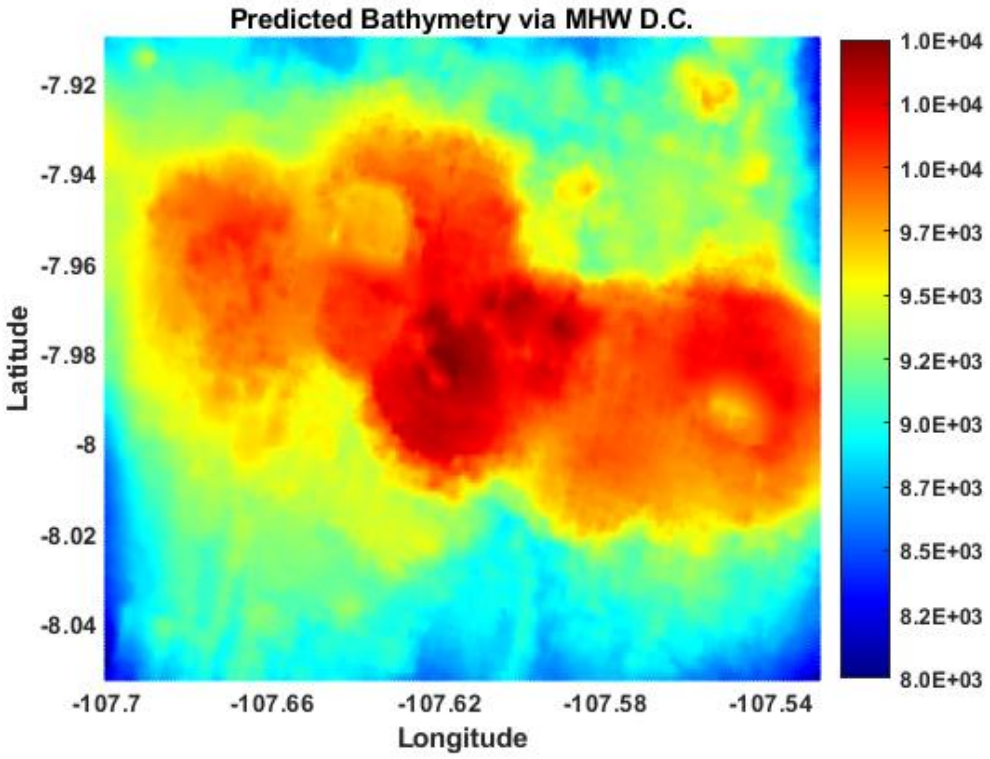

Figure 4.36 MHW predicted bathymetry of two side by side seamounts.

Gravity data wavelet filtered prior to downward continuation (units in meters).

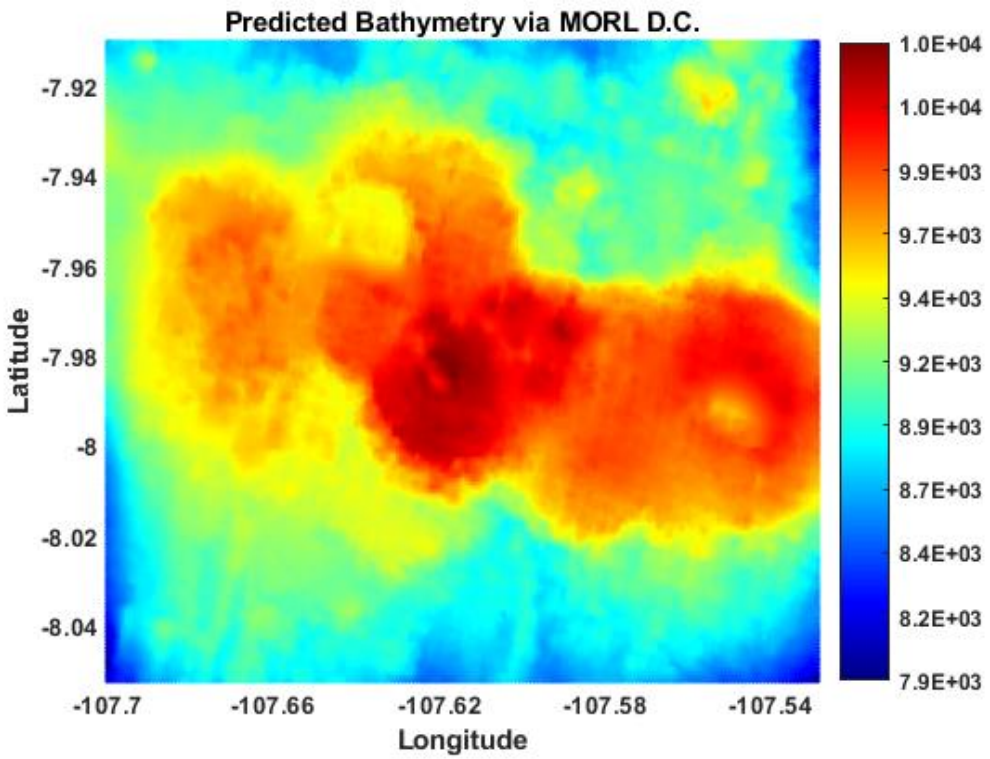

Figure 4.37 Morlet predicted bathymetry of two side by side seamounts.

Note: Gravity data wavelet filtered prior to downward continuation (units in meters).

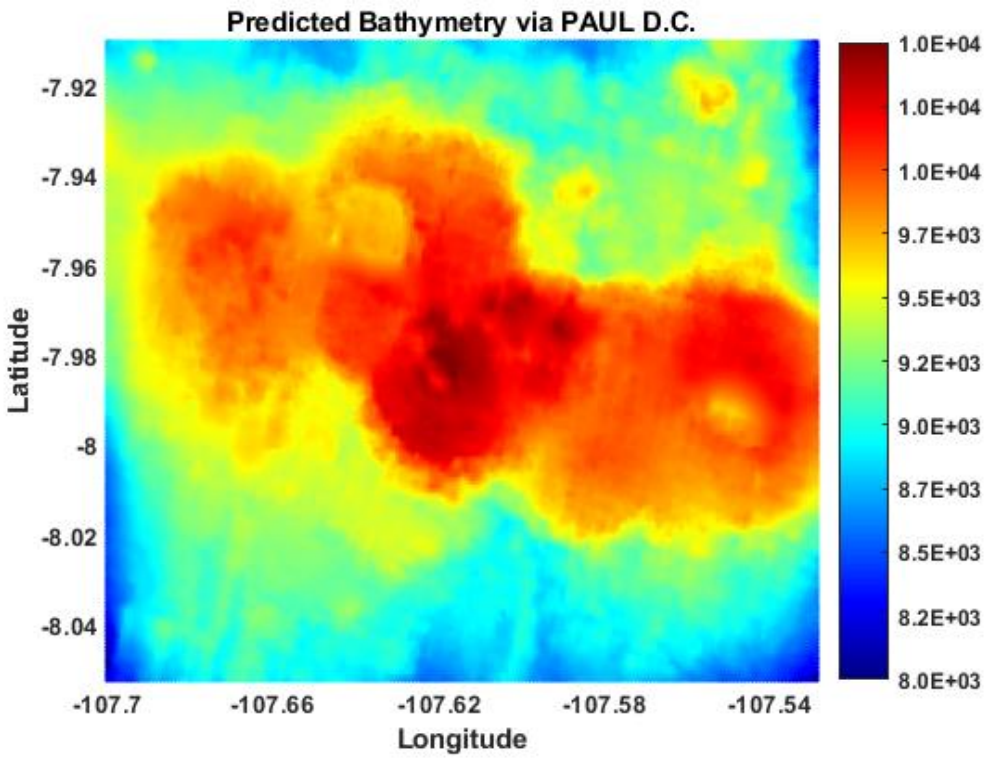

Figure 4.38 Paul predicted bathymetry of two side by side seamounts.

Note: Gravity data wavelet filtered prior to downward continuation (units in meters).

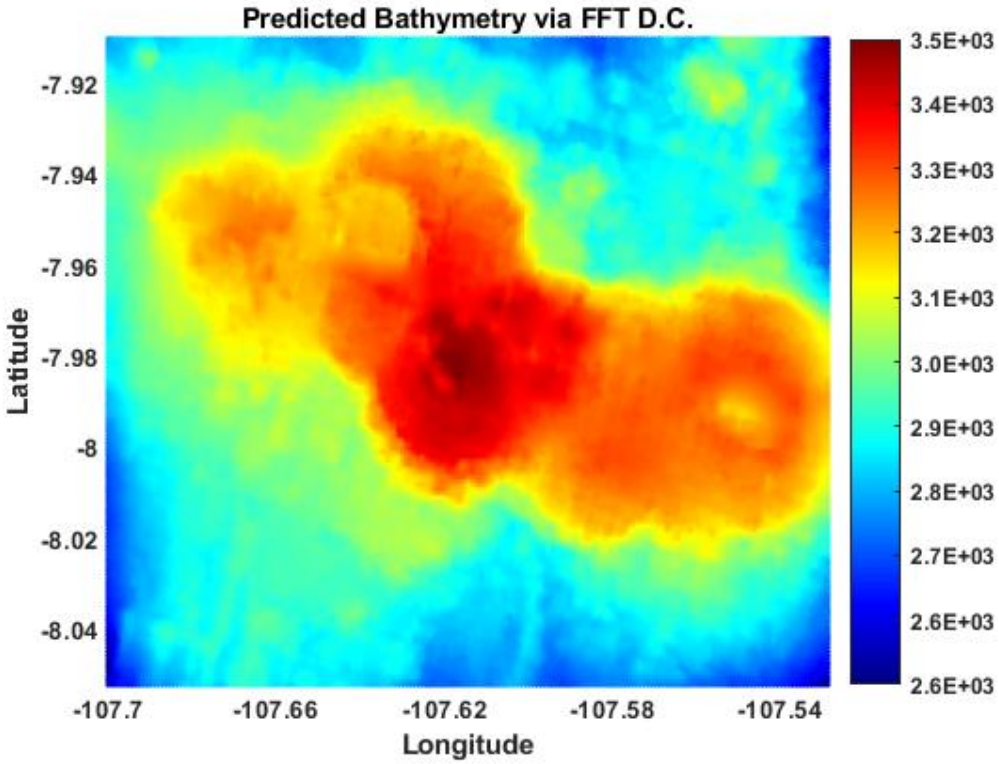

Figure 4.39 FFT predicted bathymetry of two side by side seamounts.

Note; Units are in meters.

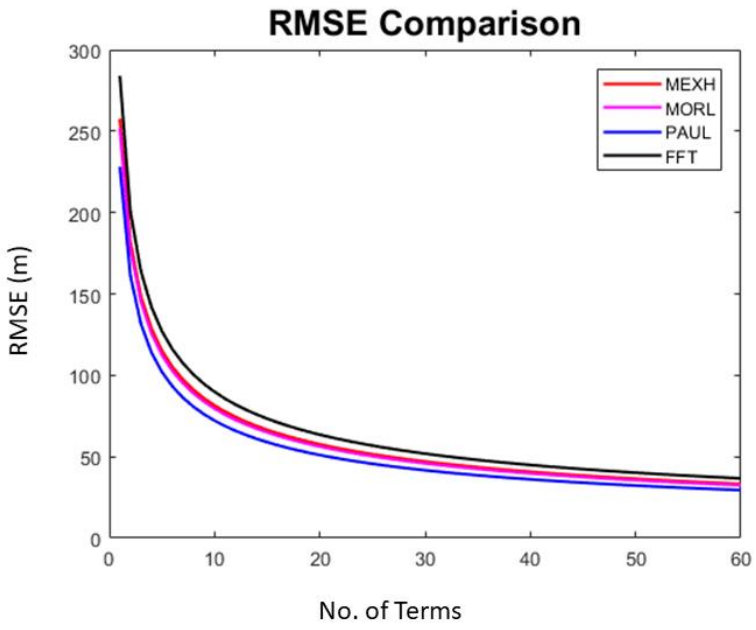

Figure 4.40 Error comparison between tested basis functions.

Similar to the whole area covered in figure 4.30, the wavelets outperformed the FFT predicted bathymetry. Again, major improvements are not easily discernable, but improvements in feature detail were somewhat apparent. The wavelets did produce a lower error than the FFT. However, it would have been expected that the wavelets would have dramatically outperformed the FFT when focusing in on features such as seamounts. A potential reason for the lack of significant improvement is that the features examined are data rich and already pre-filtered using a Fourier transform. It stands to reason that another test of performance would be to utilize a sparser data set. To accomplish this, a simple test was formulated. The already computed predicted bathymetries for each wavelet and the Fourier transform were made sparse by first sorting their predicted topographical heights with ascending values. Note that ascending values are required as the collected data comes from multibeam SONAR, thus the values are for depth giving

lower values to features such as seamounts and higher values for the deeper flatter ocean floor. Once sorted, approximately 95% of the depth values are replaced with zeros. The remaining values are plotted with their respective latitudes and longitudes.

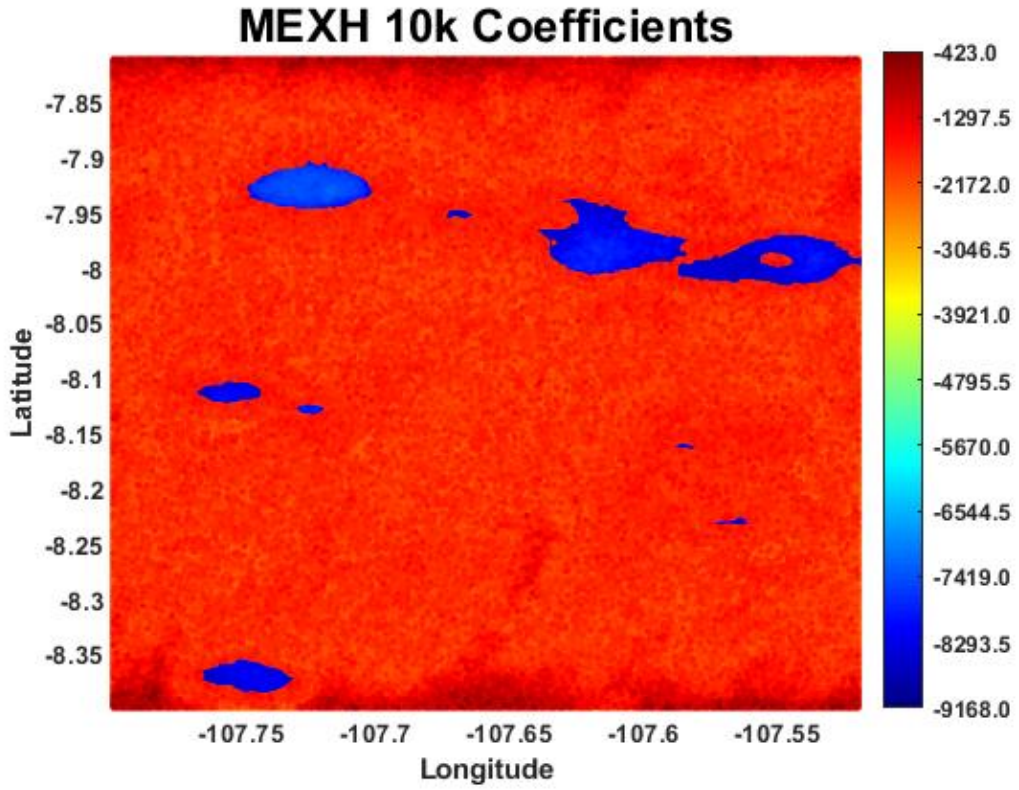

Figure 4.41 MHW solution to the area of interest with only 5% of the terms

.Note: Units are in meters.

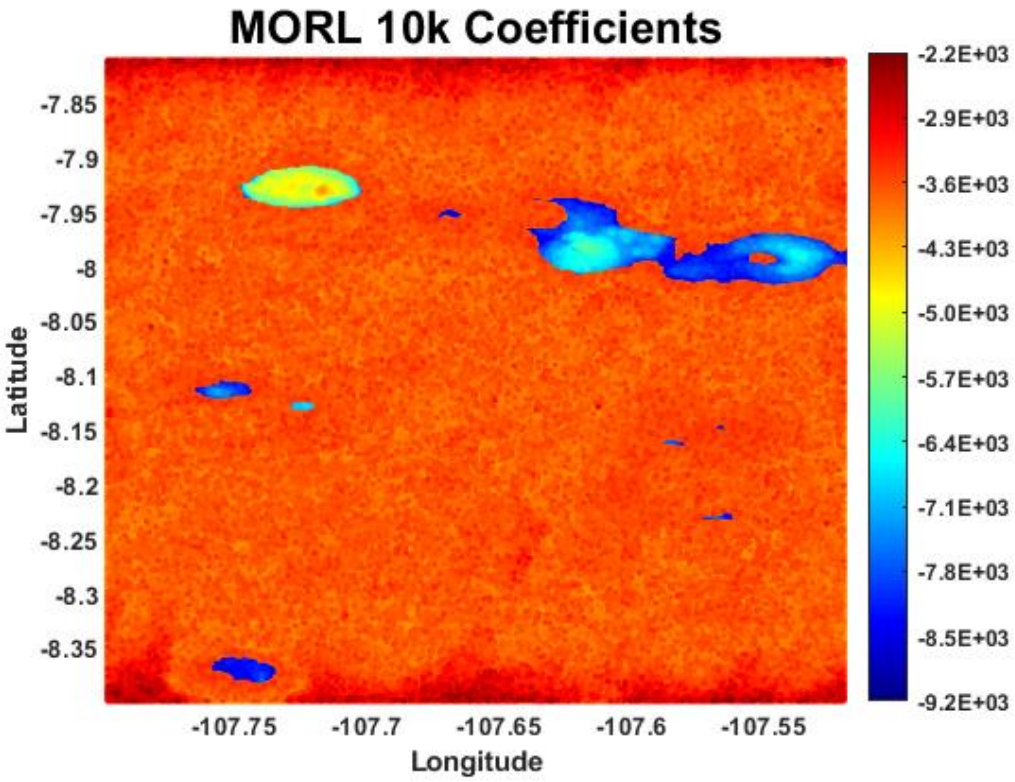

Figure 4.42 Morlet solution to the area of interest with only 5% of the terms

Note: Units are in meters.

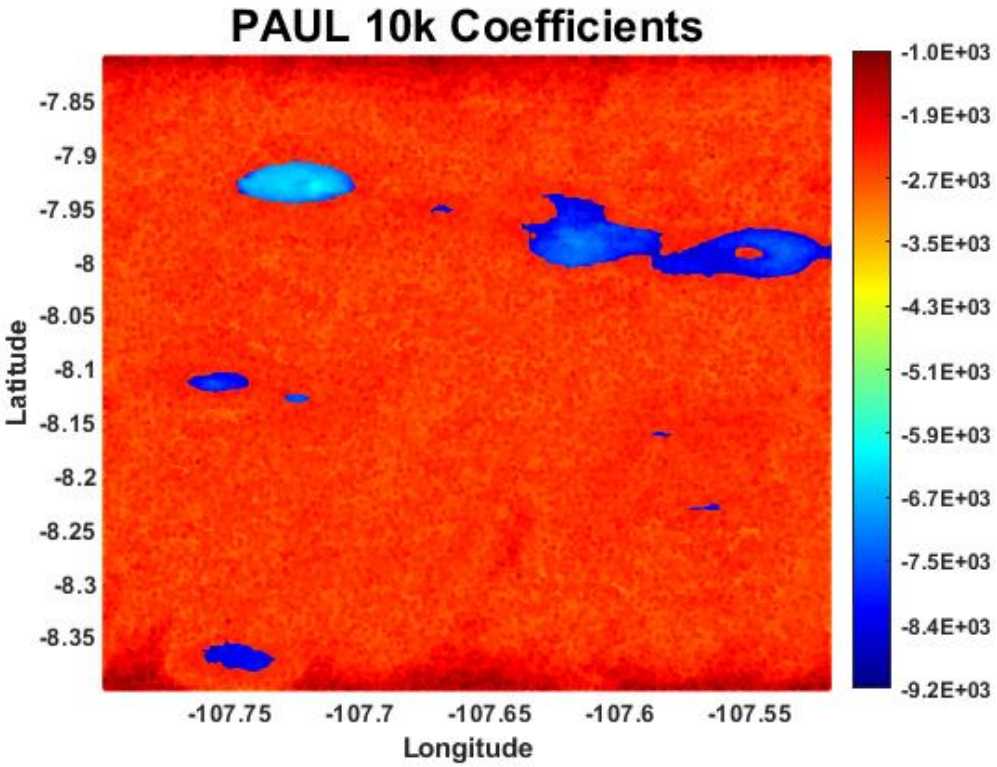

Figure 4.43 Paul solution to the area of interest with only 5% of the terms

Note: Units are in meters.

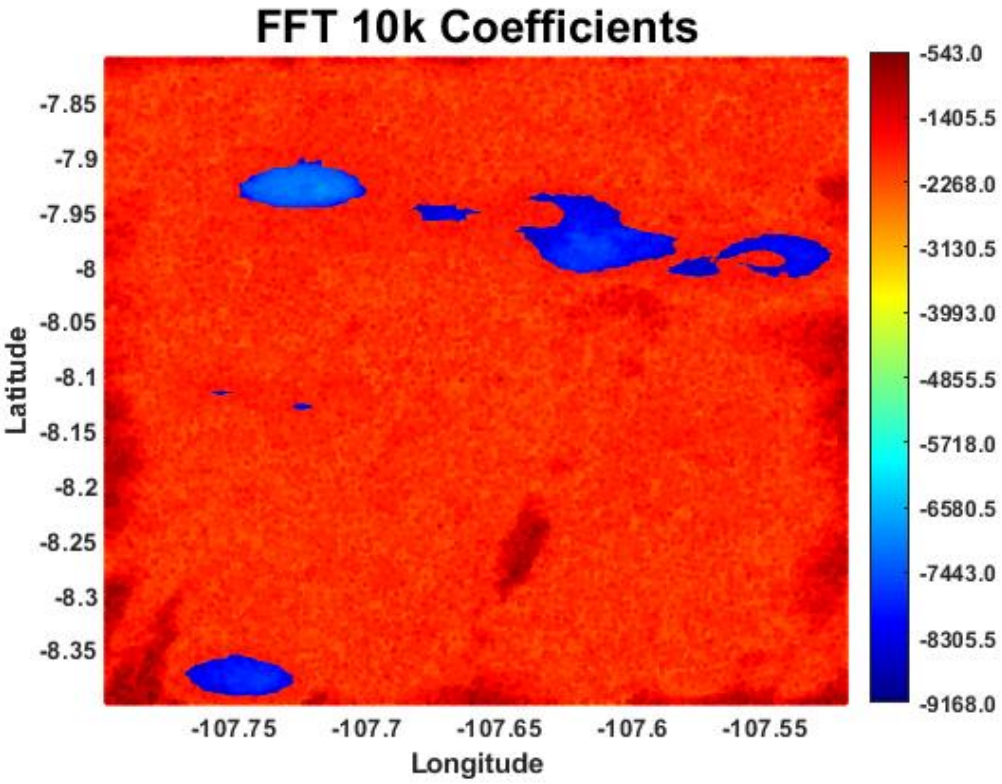

Figure 4.44 Paul solution to the area of interest with only 5% of the terms

Note: Units are in meters.

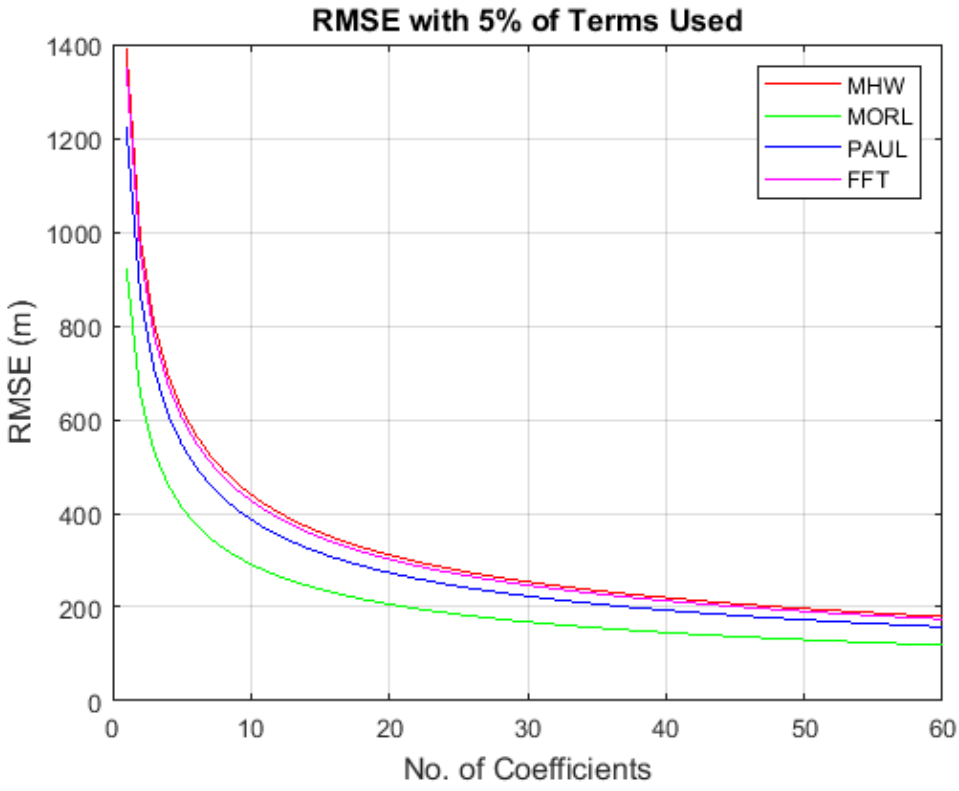

Figure 4.45 Error comparison beween tested basis functions.

Here not only does the Morlet wavelet (figure 4.42) demonstrate an increase in detail for the features as compared to the other wavelets and the FFT, it also has the lowest RMS error of the tested basis functions. The Paul wavelet showed less detail than the Morlet wavelet, and the Mexican Hat showed a statistical insignificant improvement compared to the FFT.

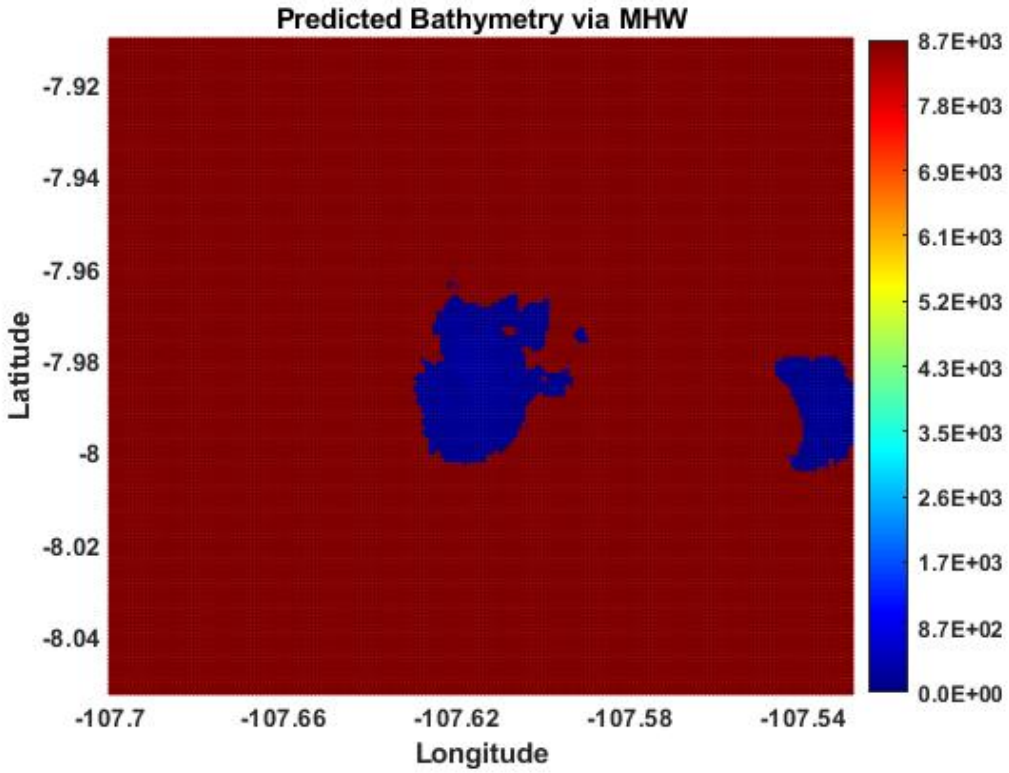

Figure 4.46 MHW solution of two side by side seamounts with only 5% of the terms

Note: Units are in meters.

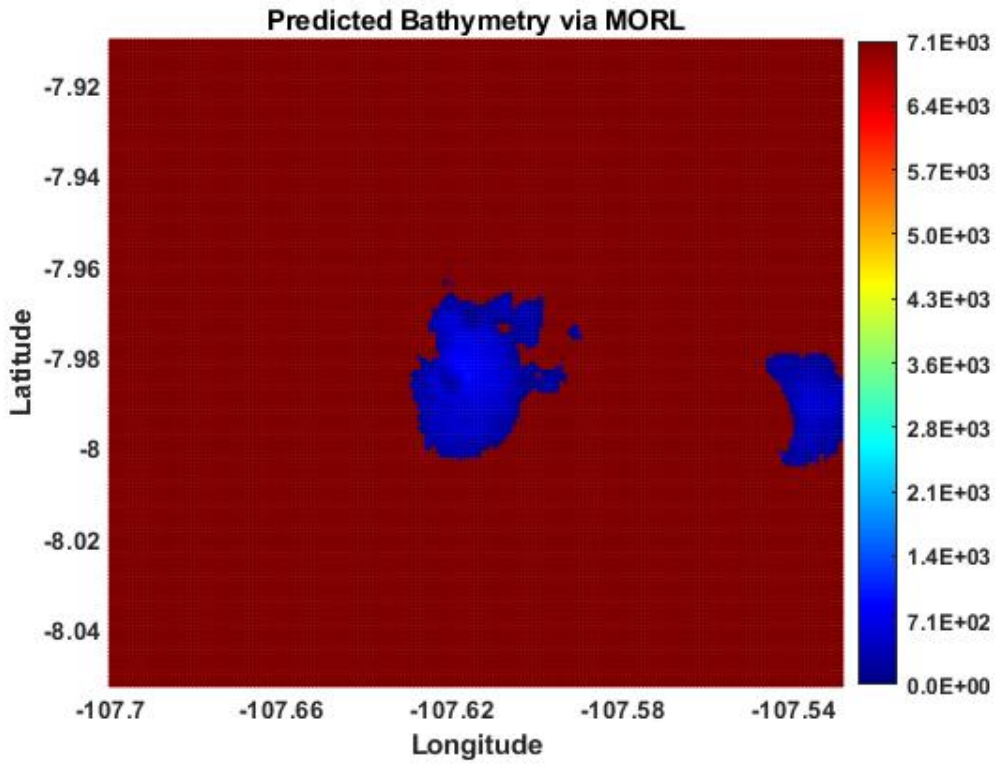

Figure 4.47 Morlet solution of two side by side seamounts with only 5% of the terms

Note: Units are in meters.

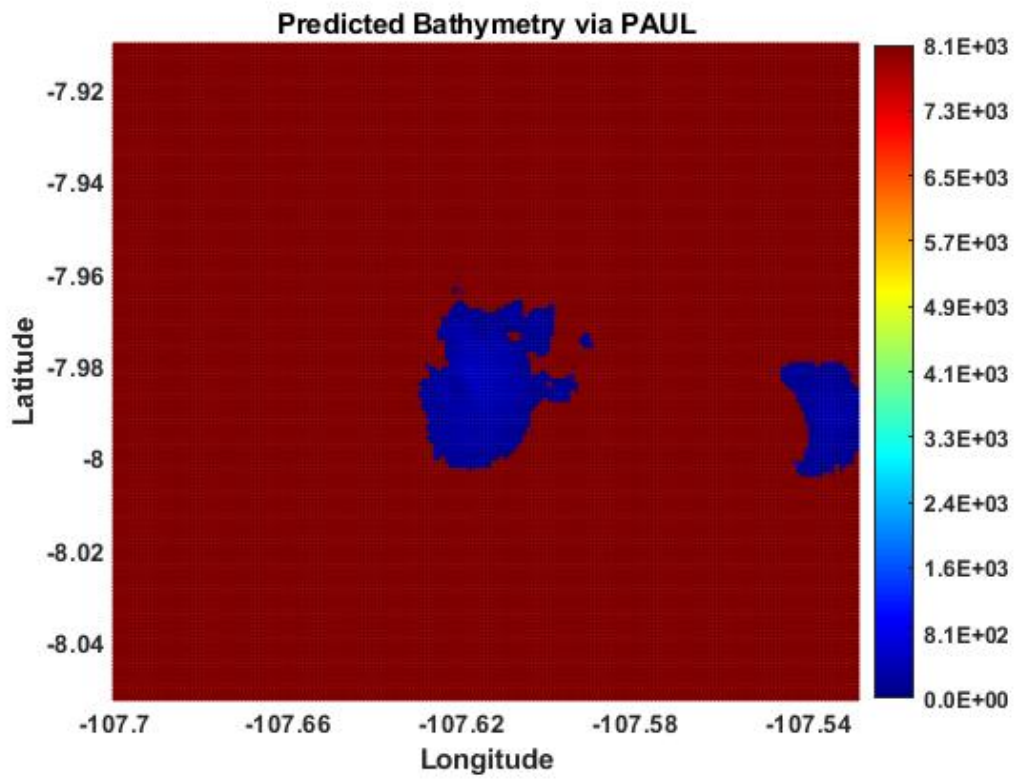

Figure 4.48 Paul solution of two side by side seamounts with only 5% of the terms

Note: Units are in meters.

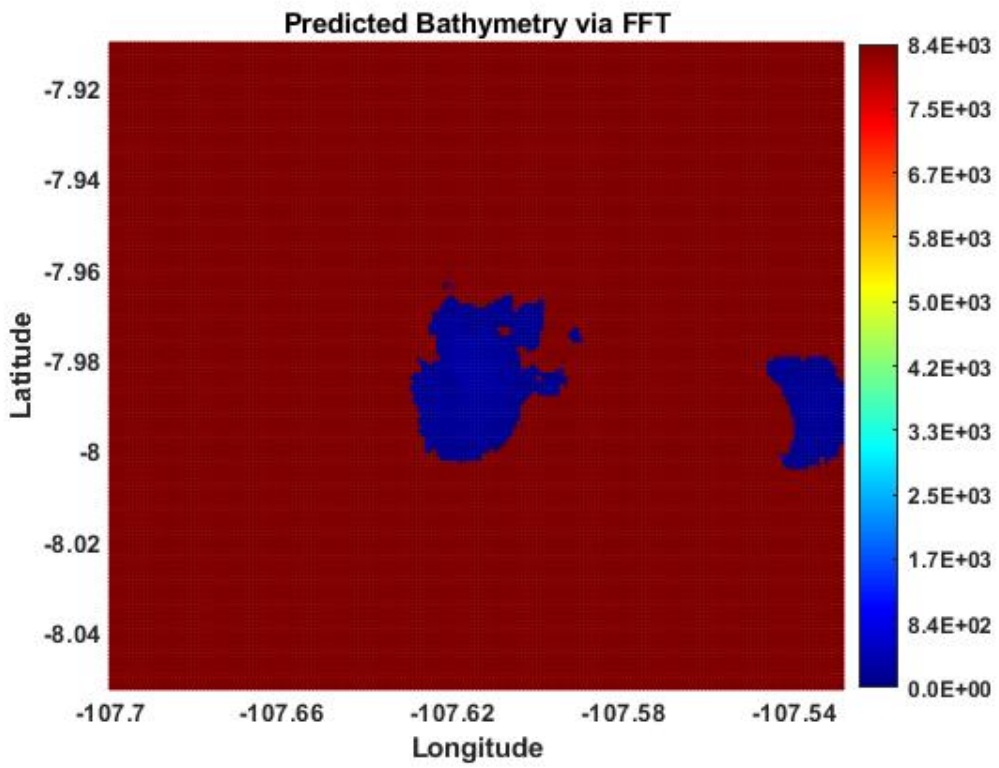

Figure 4.49 FFT solution of two side by side seamounts with only 5% of the terms

Note: Units are in meters.

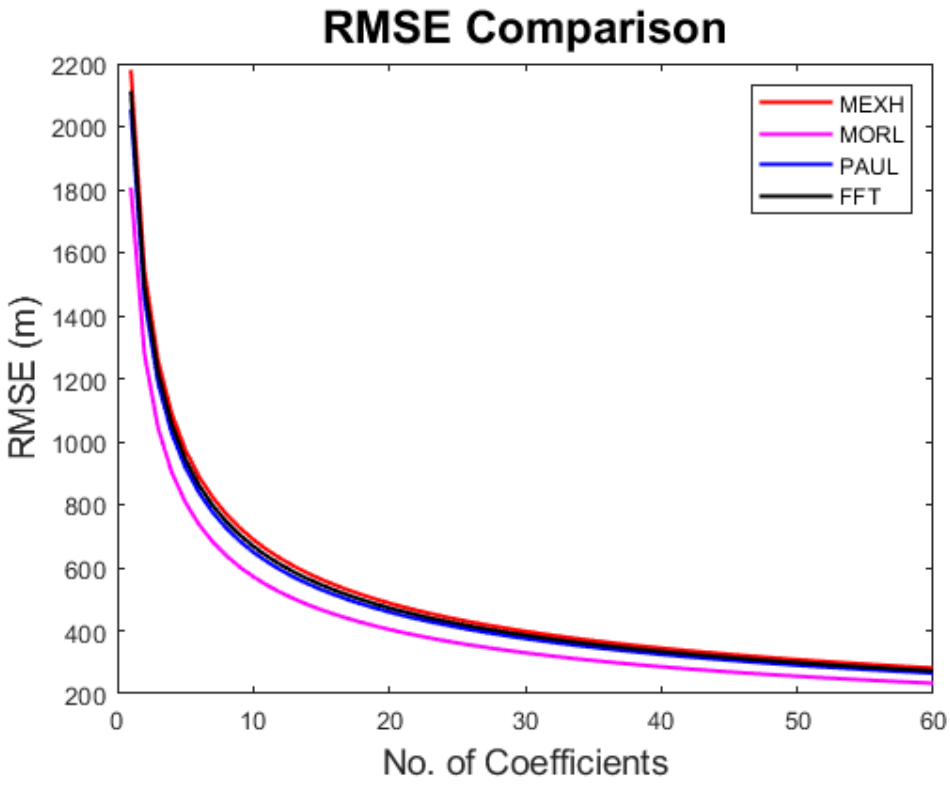

Figure 4.50 Error comparison between tested basis functions.

Figures 4.46 – 4.48 are similar to figures 4.41 – 4.44 but are focused on the two key seamounts in the northeastern corner of the area. Note: the red shown in these figures does not represent a topographical value. Red here, simply shows that there is no data available. As percentages of coefficients were used in the residual calculation, where coefficients were removed, there is a zero value. Very little difference was shown between the different predictions, with the Morlet giving only a slight improvement in feature detail. It is important to state that the observed increase in error for the zoomed in area, as compared to the larger region, is likely due to less data represented as a zero, enhancing the overall average height. Nonetheless, the Morlet wavelet produced a lower RMS error than the other basis functions. Although, there is little statistical difference

between them, the Paul wavelet had the next lowest error and the Mexican Hat wavelet had the greatest error. The reason for the FFT outperforming the Mexican Hat is unknown and was not predicted. A guess as to why that was the case is discussed in the Discussion/Conclusions section.

One last analysis was conducted. Residual plots were made in an effort to determine how well the different basis function types, wavelet vs. FT, reproduced the signals. The earlier tests of simple signals is not a good place to test this as wavelets are local and the FT is global. In essence, a difference test will simply show locality for the wavelets and global reconstruction for the FT in the simple reconstructions. However, for the previous examples, which follow the Sandwell and Smith six-step method, difference plots are great measure of how the basis functions act in producing the bathymetric signal. This is accomplished by plotting the differences for different percentages of terms used. The analysis will begin with 50%, then 25%, 12% and finally 5% of terms. The idea of beginning with a larger number of terms is to demonstrate which of the basis functions does the best job of identifying the key features as terms are removed. We begin with the smaller area concentrating on two seamounts, as previously. With 50% of the terms used, it is visible from the plots below that despite the small statistical difference (noted by the Student t-test results and RMS error plots), visually, the Morlet wavelet gave more detail and allowed for a better reproduction of the seamounts.

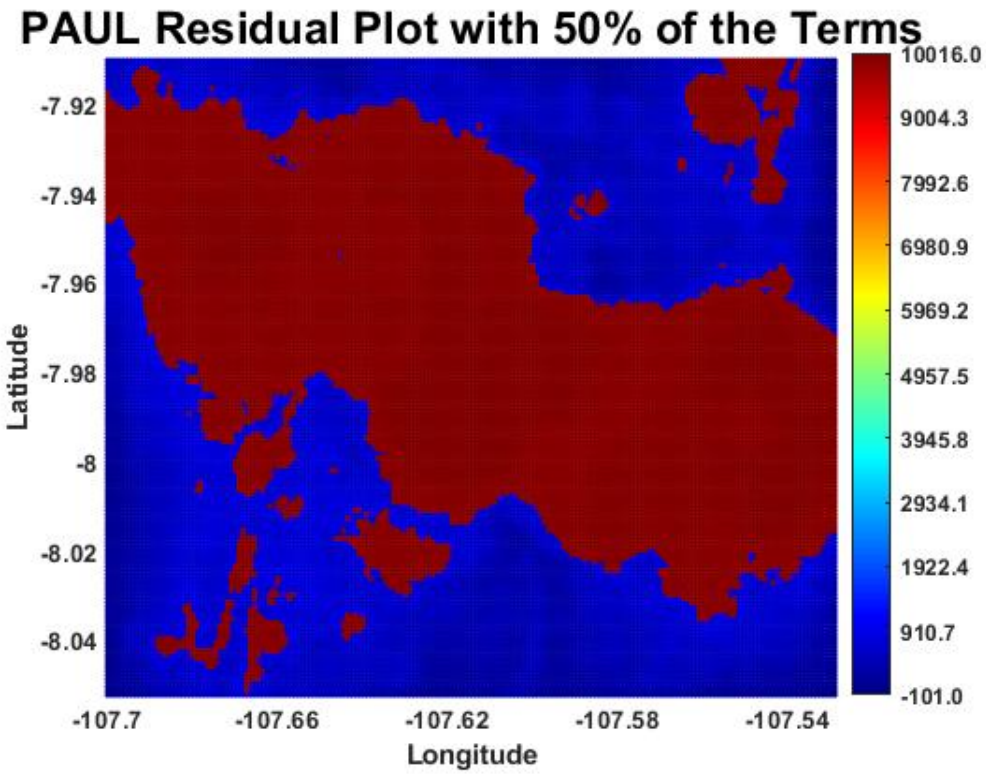

Figure 4.51 Residual plot with only 50% of terms used for the Paul Transform

Note: Units are in meters

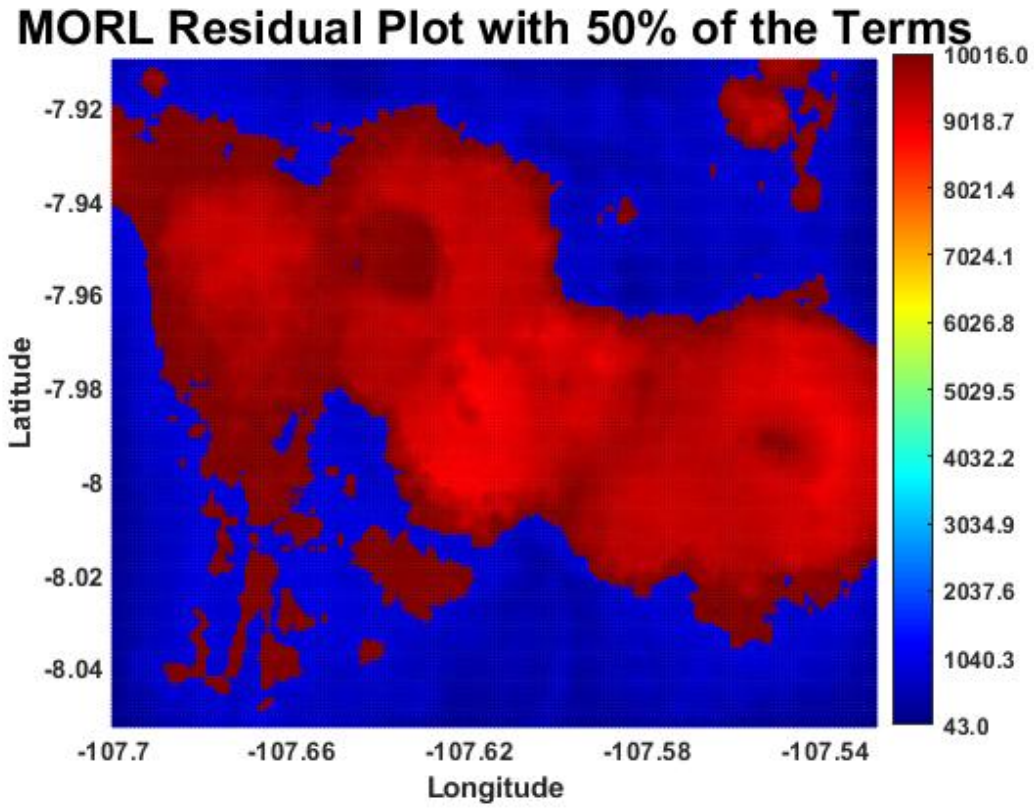

Figure 4.52 Residual plot with only 50% of terms used for the Morlet Transform

Note: Units are in meters.

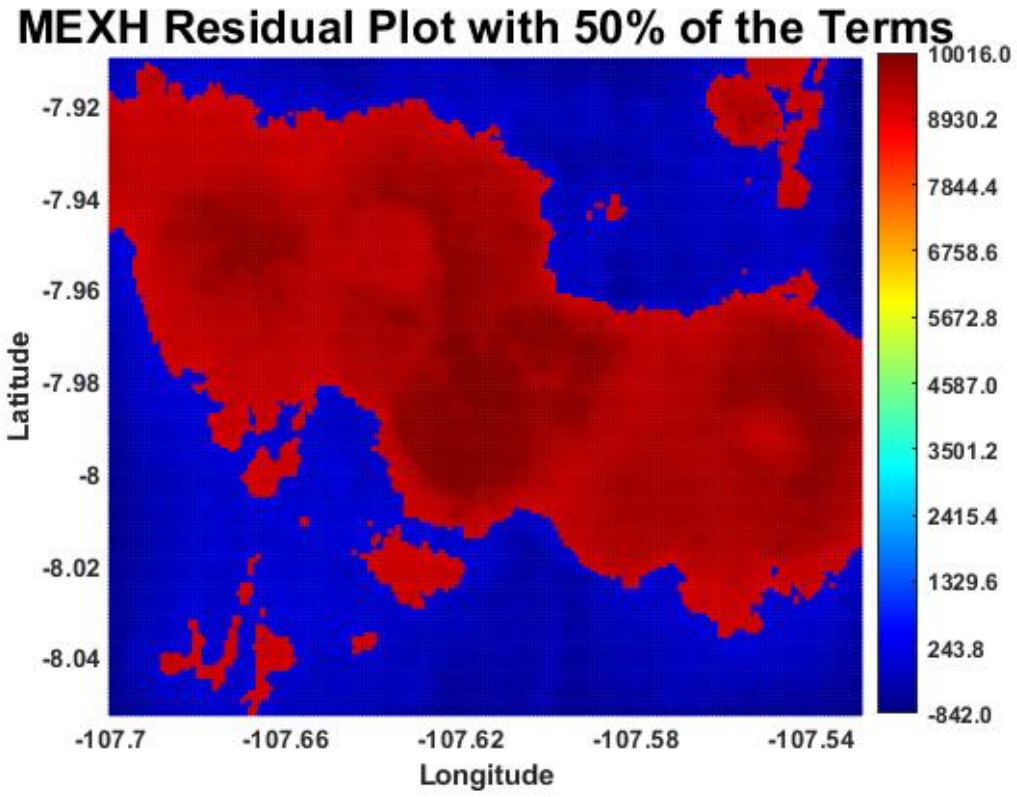

Figure 4.53 Residual plot with only 50% of terms used for the MHW Transform

Note: Units are in meters.

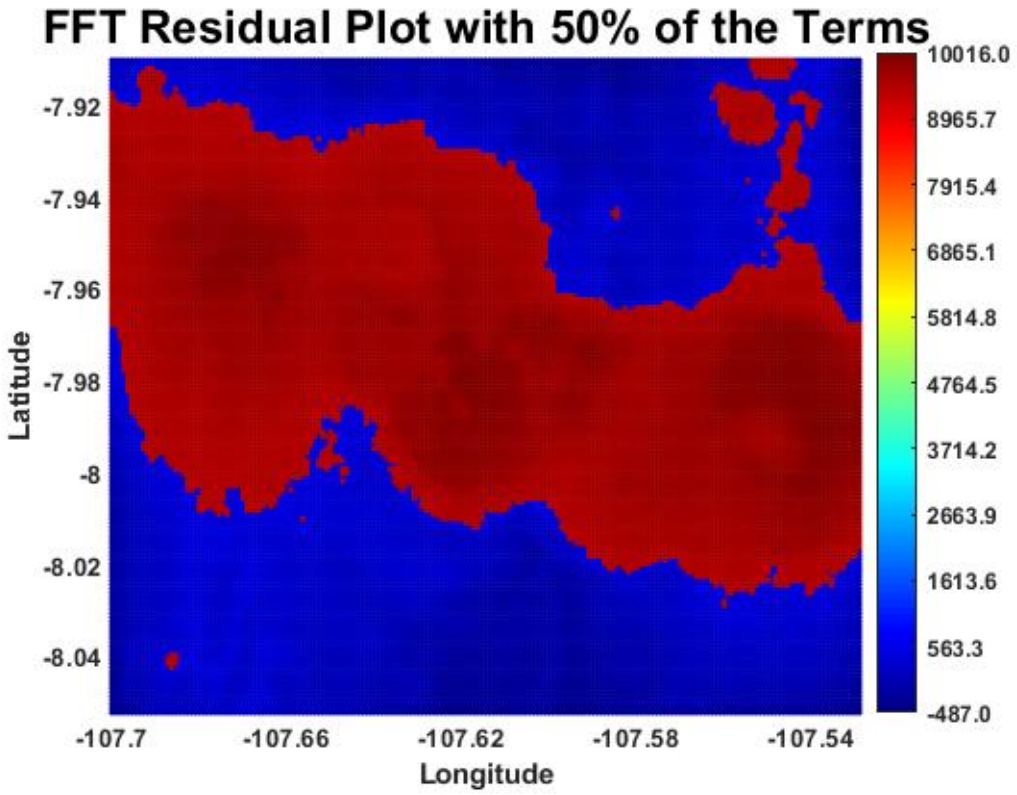

Figure 4.54 Residual plot with only 50% of terms used for the FFT

Note; Units are in meters.

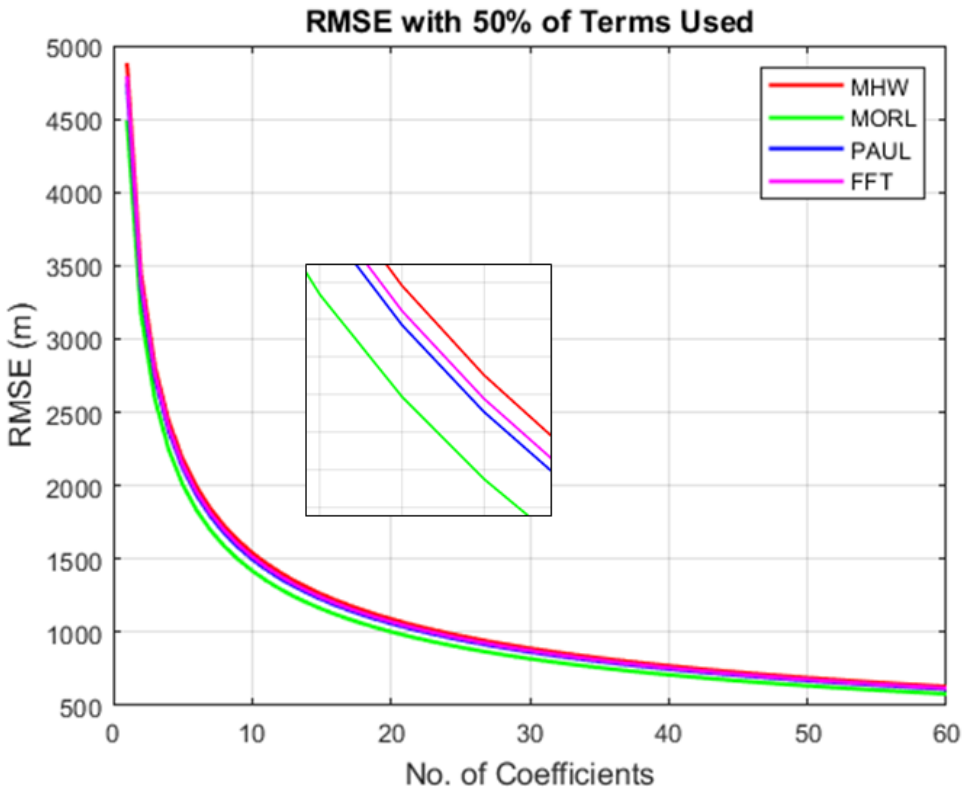

Figure 4.55 RMSE comparison of tested basis functions.

Table 4.3 Student t-test Results

	Null Hypothesis 0 – Accept 1 – Reject	**P (Level of Confidence)**	**CONFIDENCE INTERVAL LOWER LIMIT**	**CONFIDENCE INTERVAL UPPER LIMIT**
MHW & FT	0	0.8768	-245.4366	287.2201
PAUL & FT	0	0.5832	-326.7217	184.6388
MORLET & FT	0	0.9300	-274.1763	250.8338

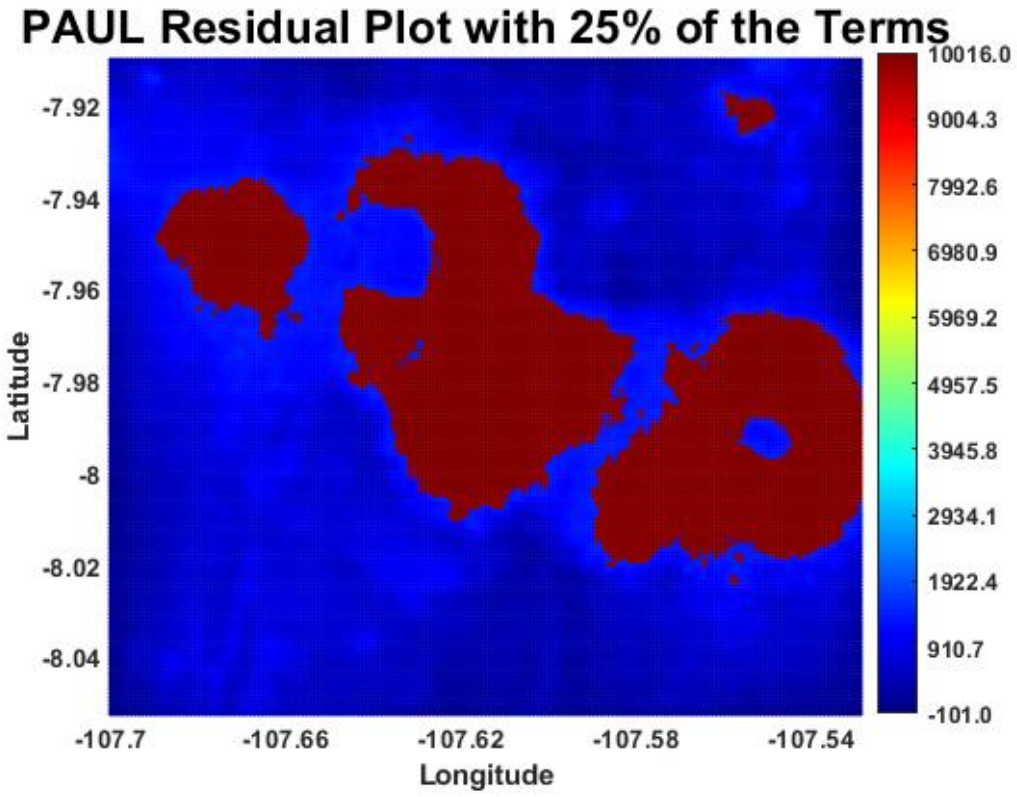

Figure 4.56 Residual plot with only 25% of terms used for the Paul Transform

Note: Units are in meters.

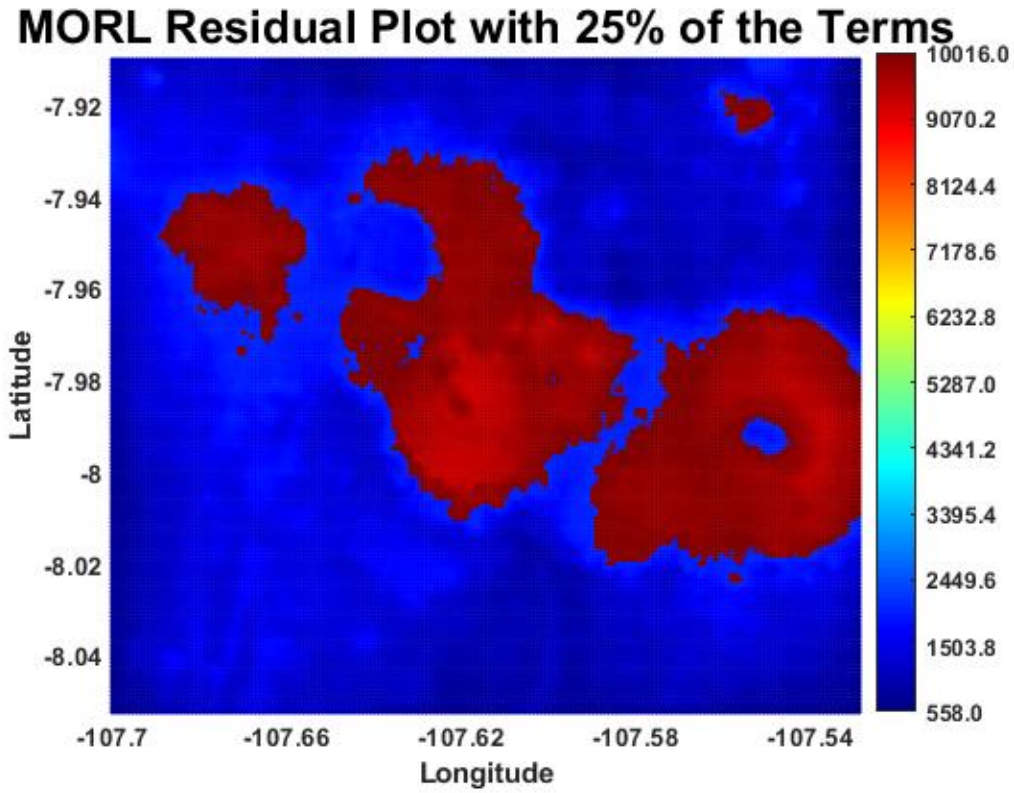

Figure 4.57 Residual plot with only 25% of terms used for the Morlet Transform

Note: Units are in meters.

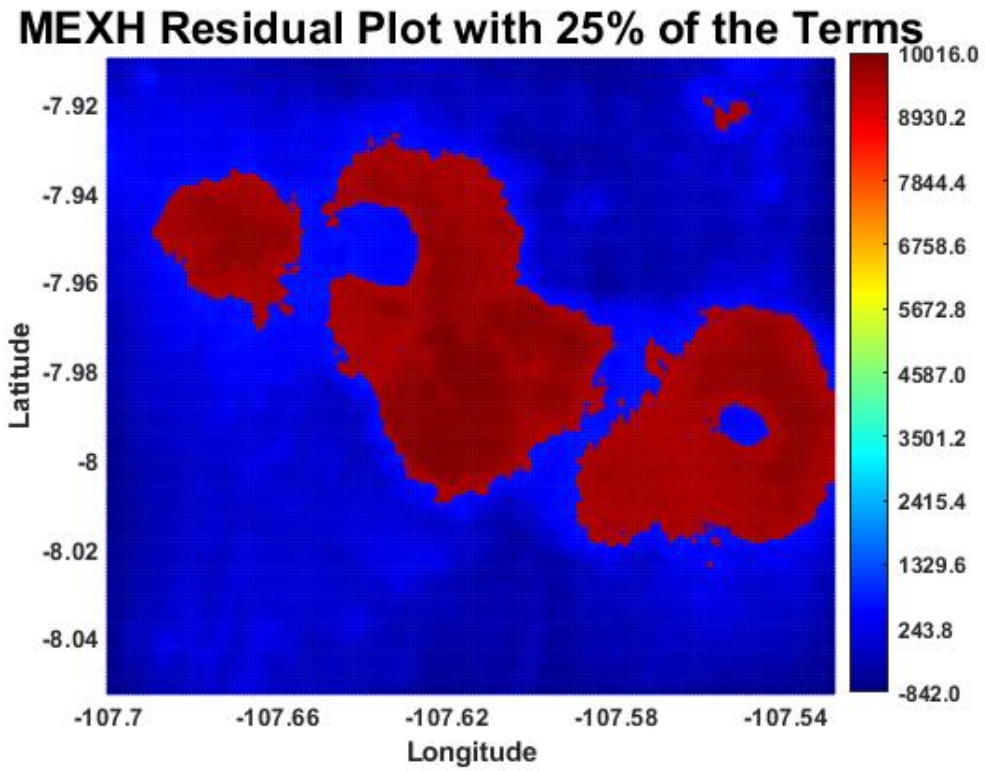

Figure 4.58 Residual plot with only 25% of terms used for the MHW Transform

Note: Units are in meters.

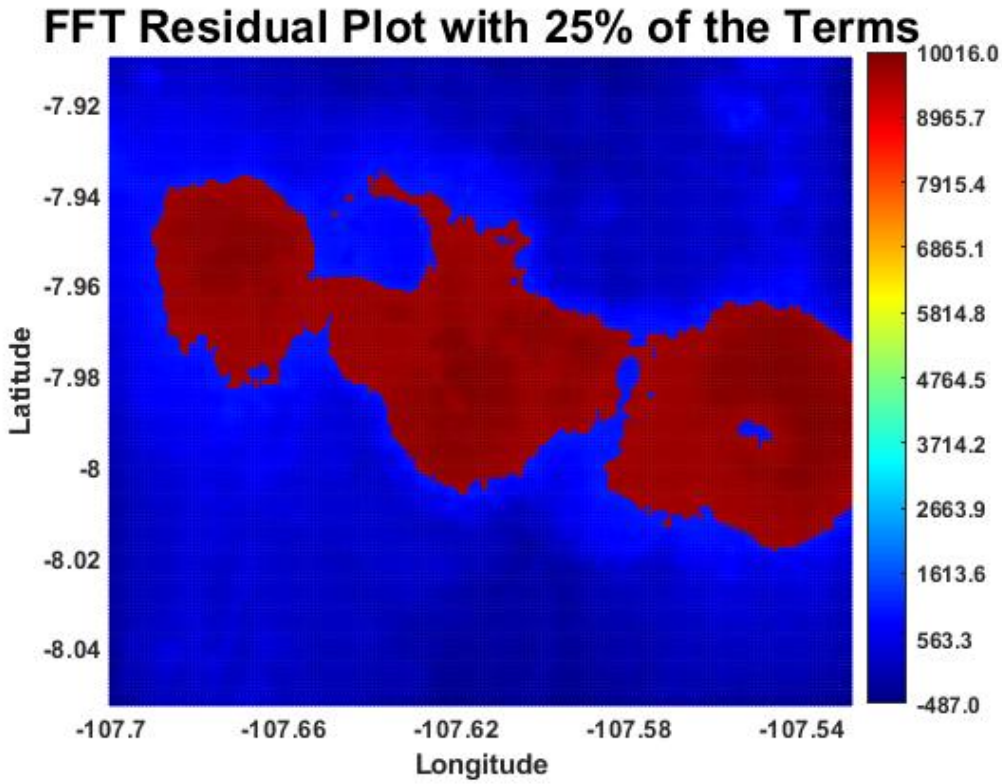

Figure 4.59 Residual plot with only 25% of terms used for the FFT

Note: Units are in meters.

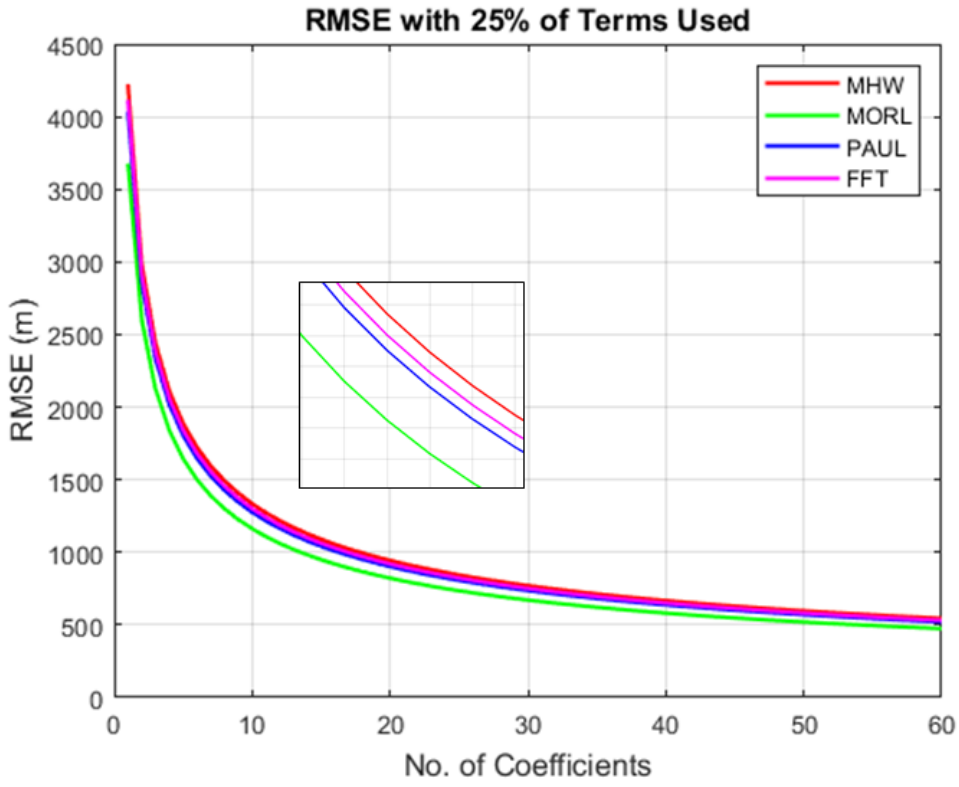

Figure 4.60 Error comparison between tested basis functions

Table 4.4 Student t-test Results

	Null Hypothesis 0 – Accept 1 – Reject	**P (Level of Confidence)**	**CONFIDENCE INTERVAL LOWER LIMIT**	**CONFIDENCE INTERVAL UPPER LIMIT**
MHW & FT	0	0.8267	-204.1320	255.0109
PAUL & FT	0	0.3453	-317.6646	112.0618
MORLET & FT	0	0.8700	-242.9876	205.8208

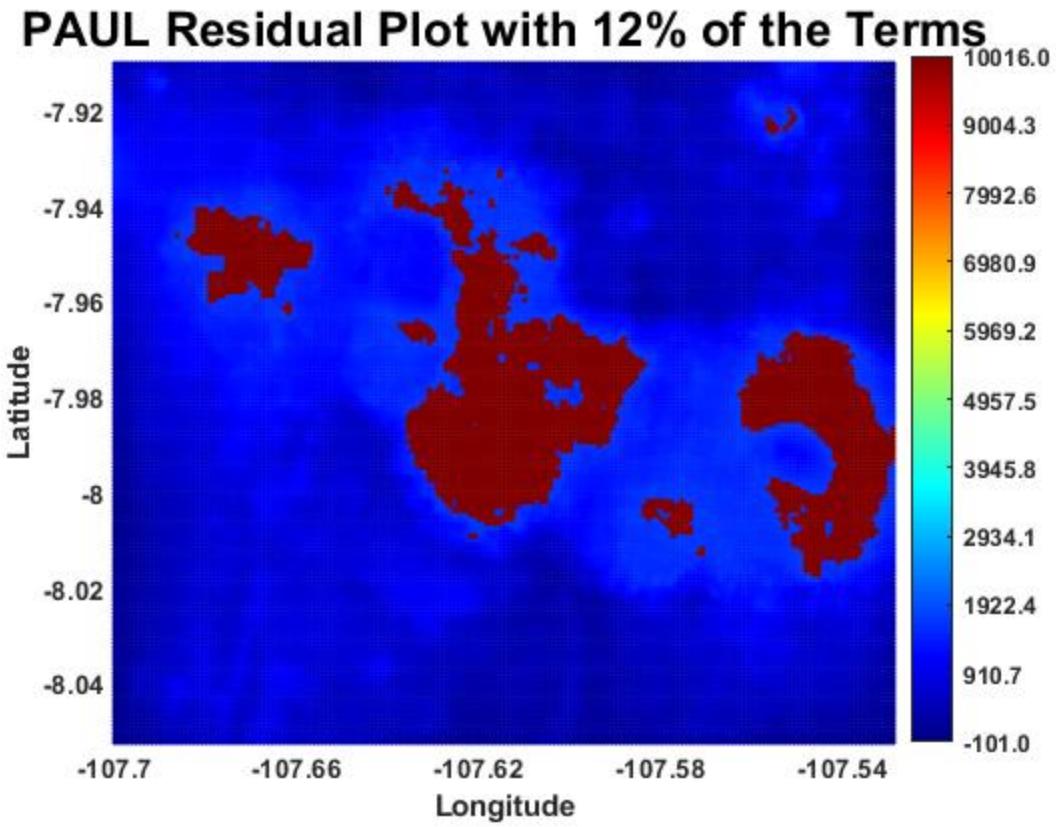

Figure 4.61 Residual plot with only 12% of terms used for the Paul Transform

Note: Units are in meters.

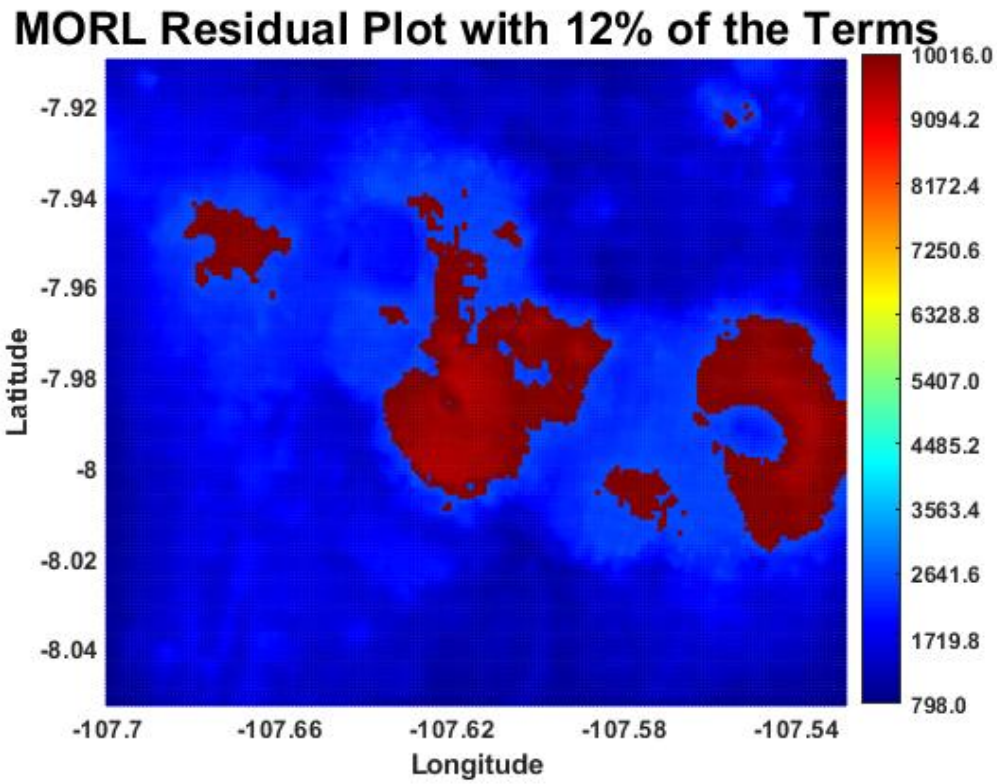

Figure 4.62 Residual plot with only 12% of terms used for the Morlet Transform

Note: Units are in meters.

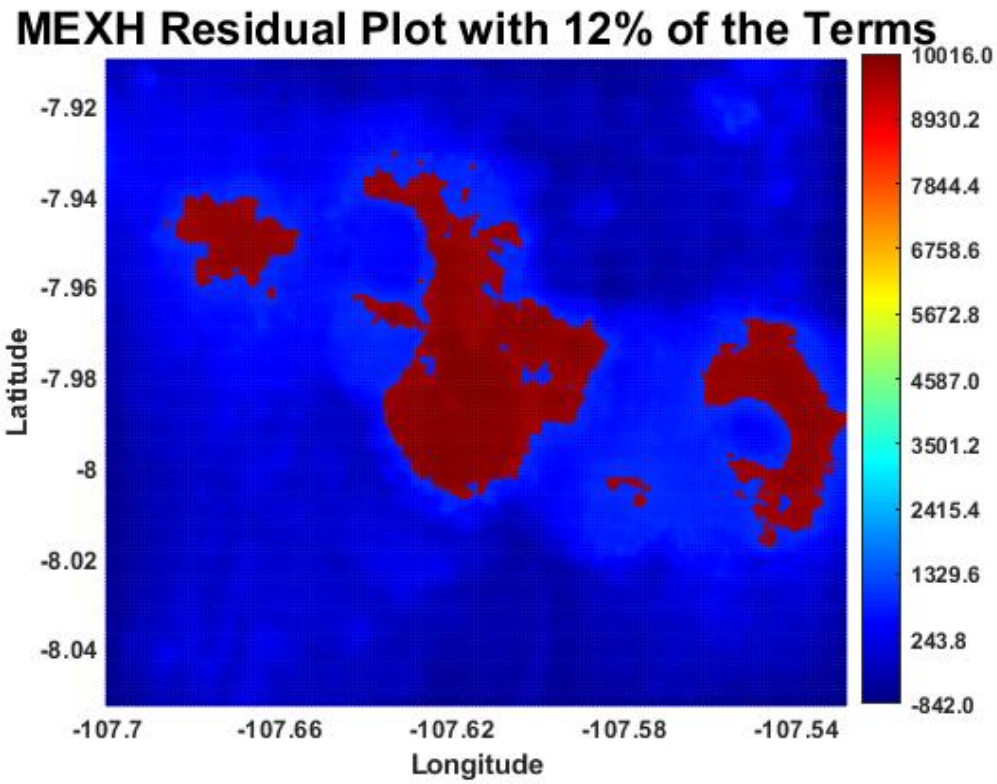

Figure 4.63 Residual plot with only 12% of terms used for the MHW Transform

Note: Units are in meters.

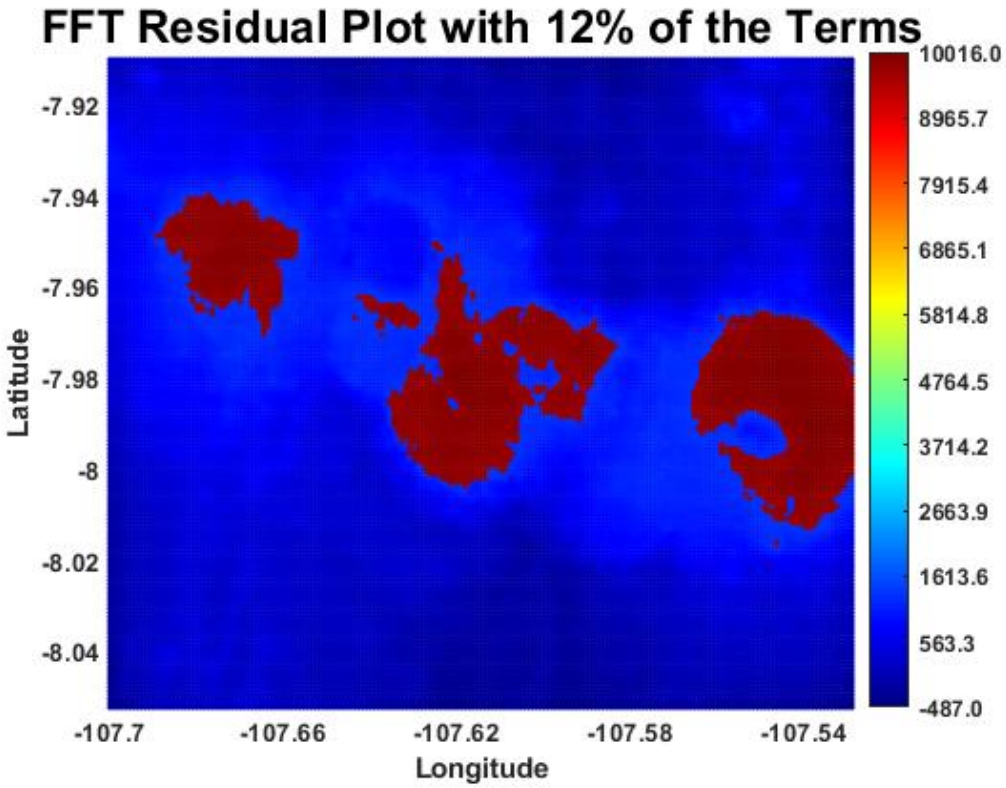

Figure 4.64 Residual plot with only 12% of terms used for the FFT

Note: Units are in meters.

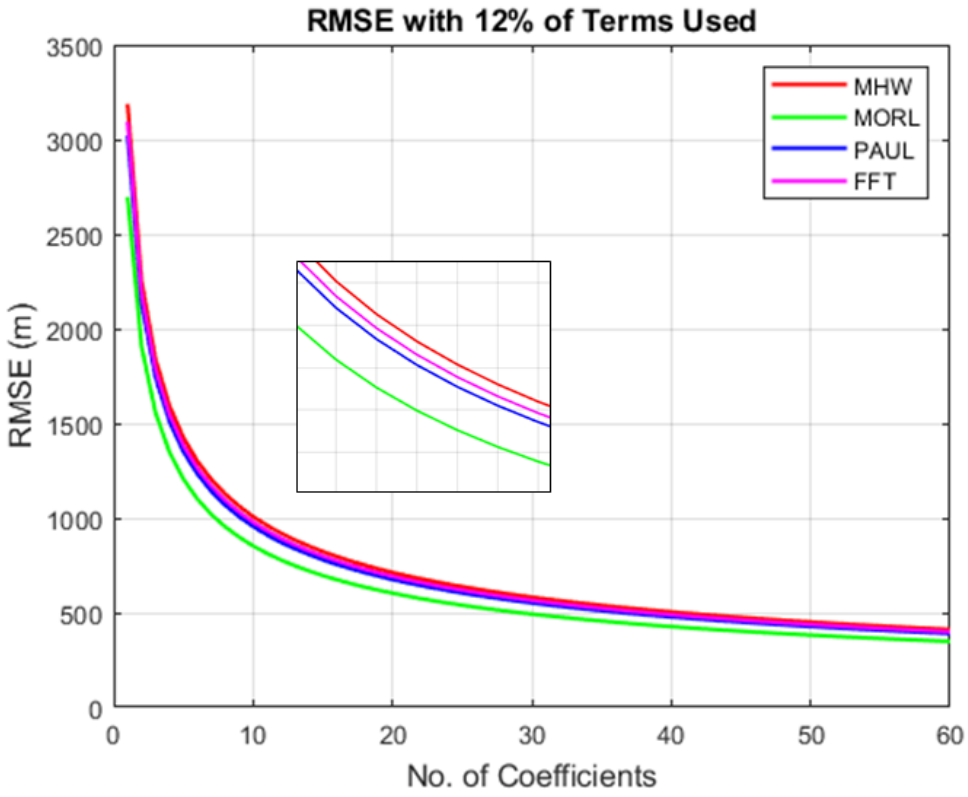

Figure 4.65 Error comparison between tested basis functions

Table 4.5 Student t-test Results

	Null Hypothesis 0 – Accept 1 – Reject	**P (Level of Confidence)**	**CONFIDENCE INTERVAL LOWER LIMIT**	**CONFIDENCE INTERVAL UPPER LIMIT**
MHW & FT	0	0.8012	-150.9011	194.9784
PAUL & FT	0	0.2500	-253.0583	66.5068
MORLET & FT	0	0.8402	-185.5193	151.1541

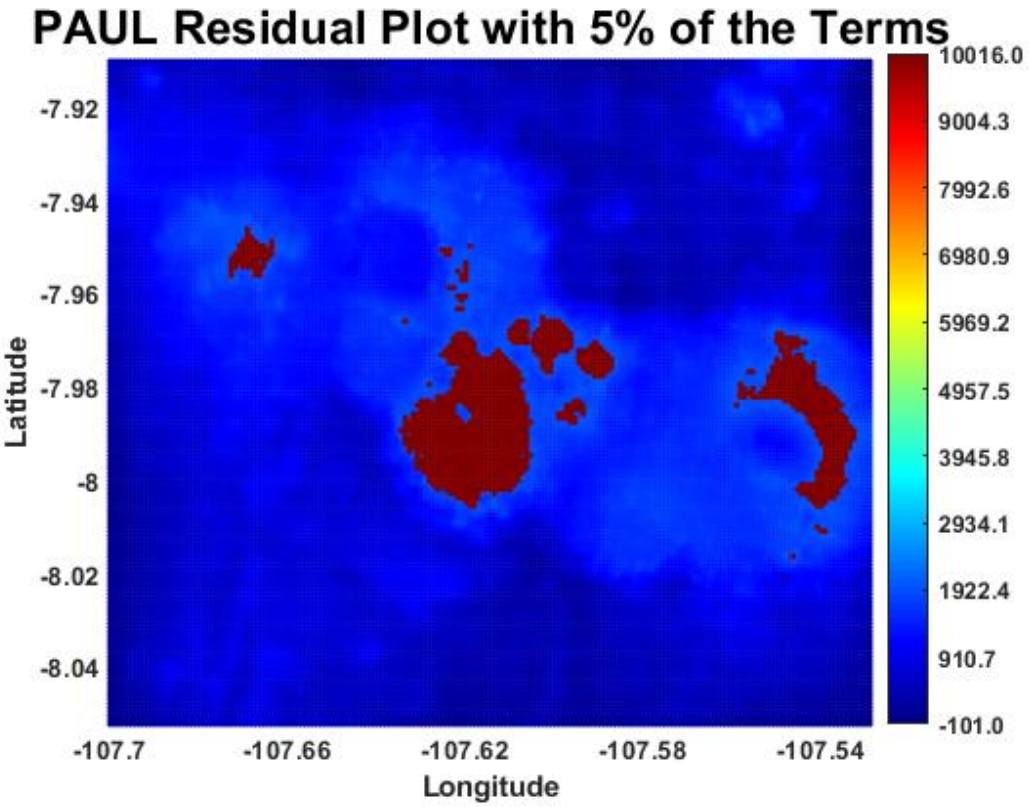

Figure 4.66 Residual plot with only 5% of terms used for the Paul Transform

Note: Units are in meters.

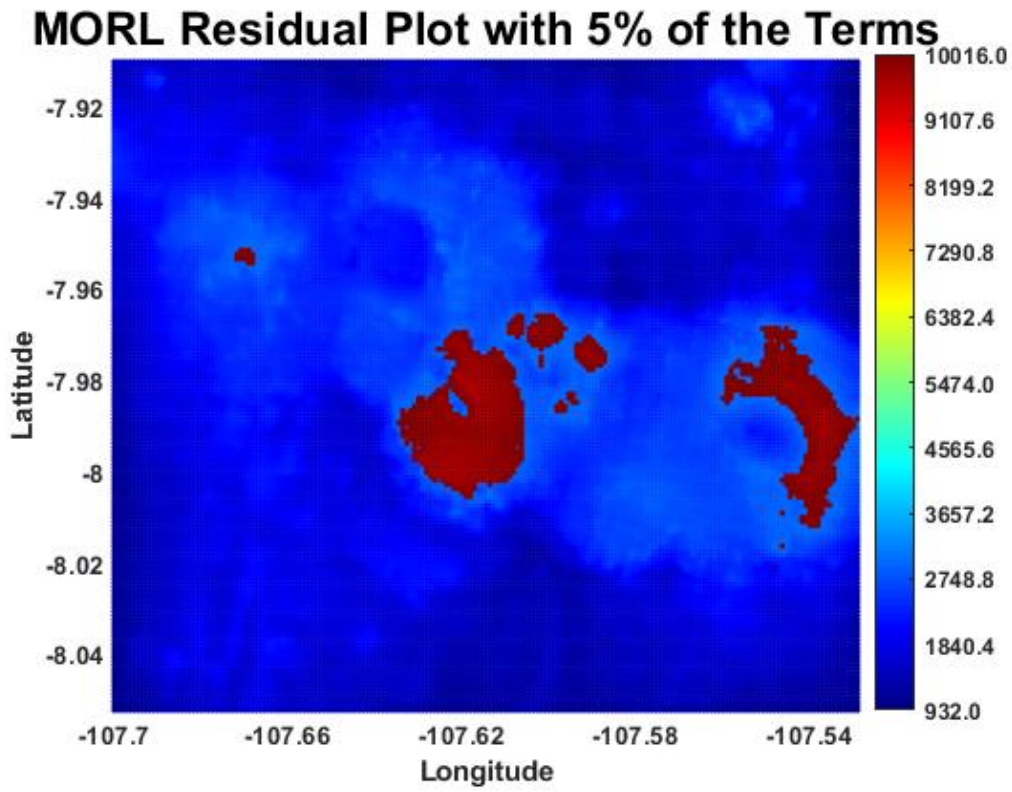

Figure 4.67 Residual plot with only 5% of terms used for the Morlet Transform

Note: Units are in meters.

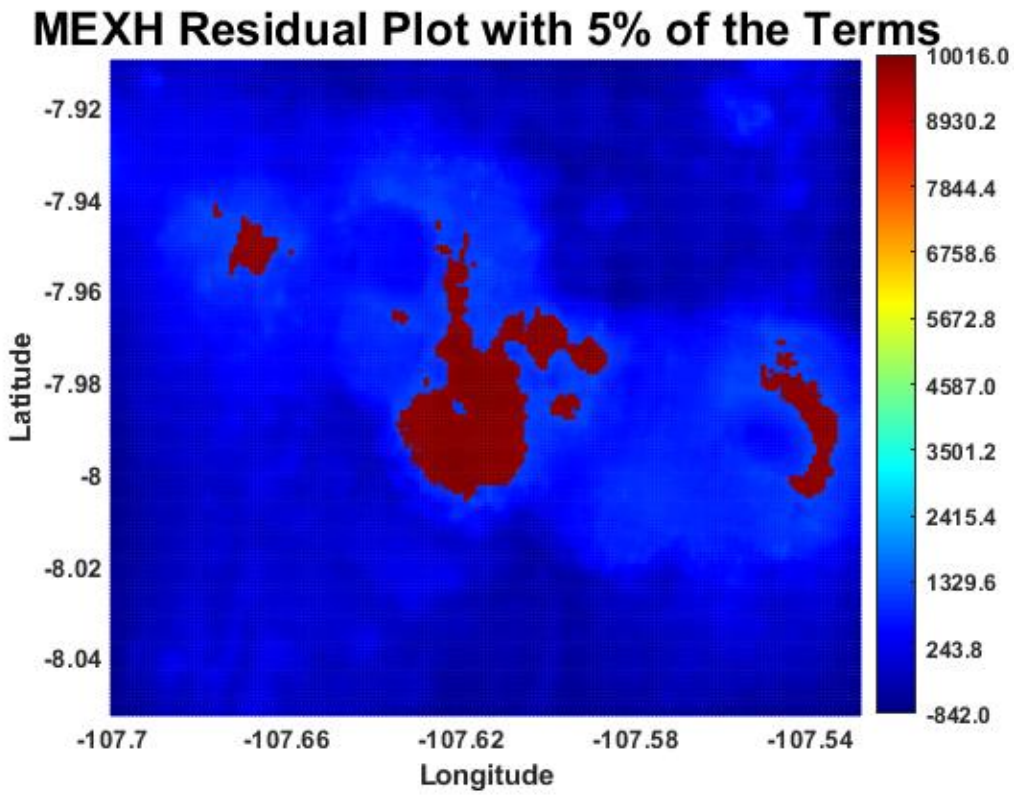

Figure 4.68 Residual plot with only 5% of terms used for the MHW Transform

Note: Units are in meters.

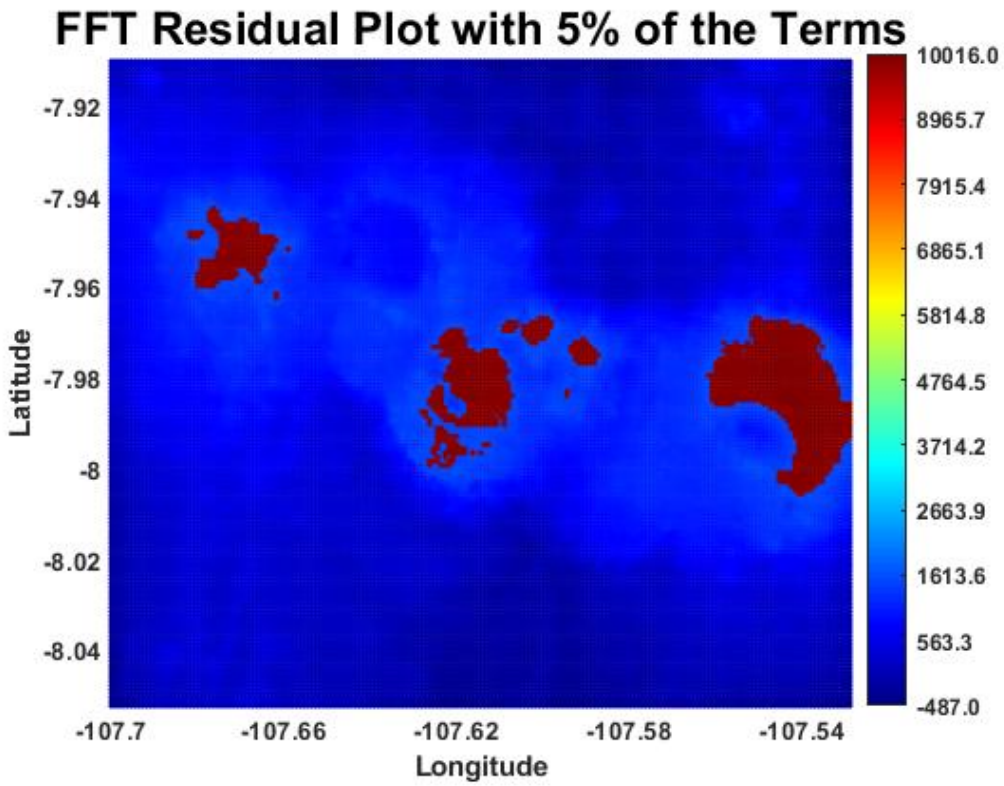

Figure 4.69 Residual plot with only 5% of terms used for the FFT

Note: Units are in meters.

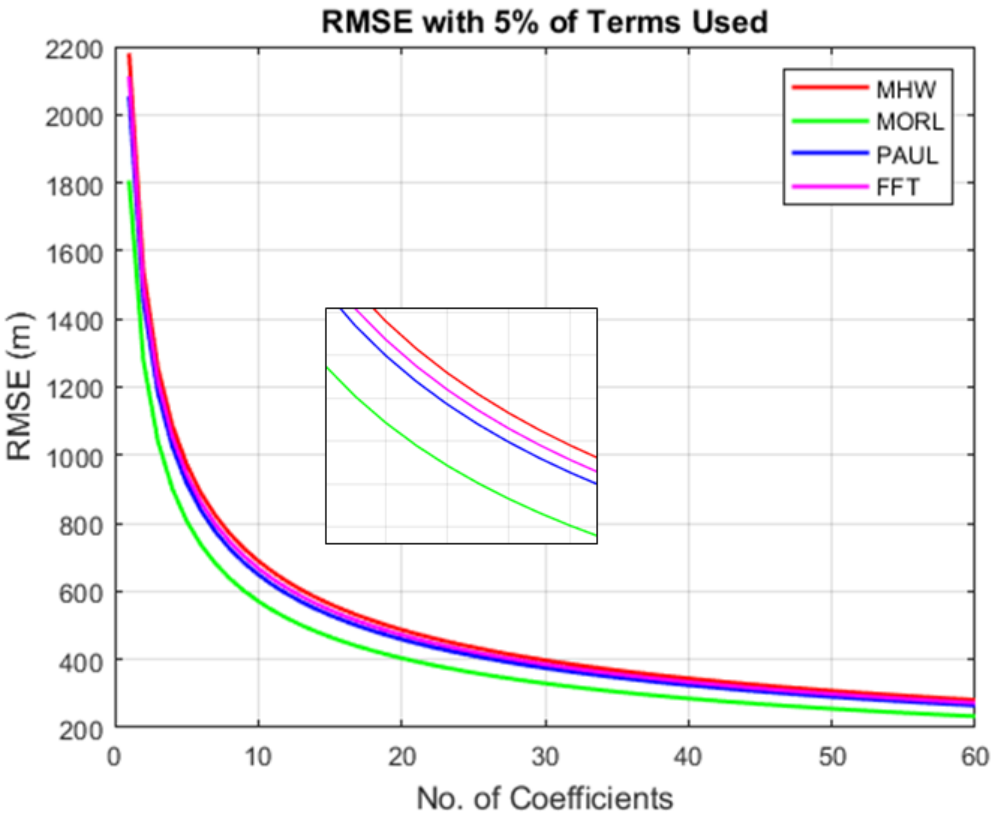

Figure 4.70 Error comparison between tested basis functions

Table 4.6 Student t-test Results

	Null Hypothesis 0 – Accept 1 – Reject	**P (Level of Confidence)**	**CONFIDENCE INTERVAL LOWER LIMIT**	**CONFIDENCE INTERVAL UPPER LIMIT**
MHW & FT	0	0.7912	-102.3501	134.0260
PAUL & FT	0	0.1911	-180.0912	36.3581
MORLET & FT	0	0.8112	-128.5732	100.8348

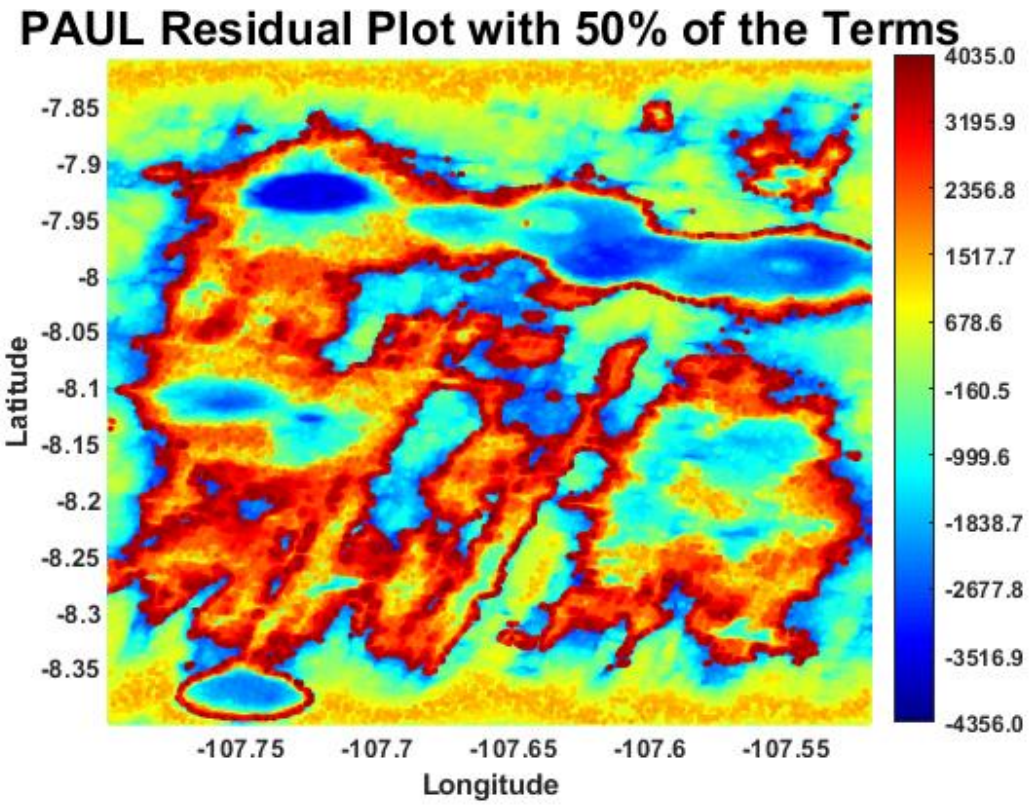

Figure 4.71 Residual of plot of larger area with only 50% of terms used for the Paul Transform

Note: Units are in meters.

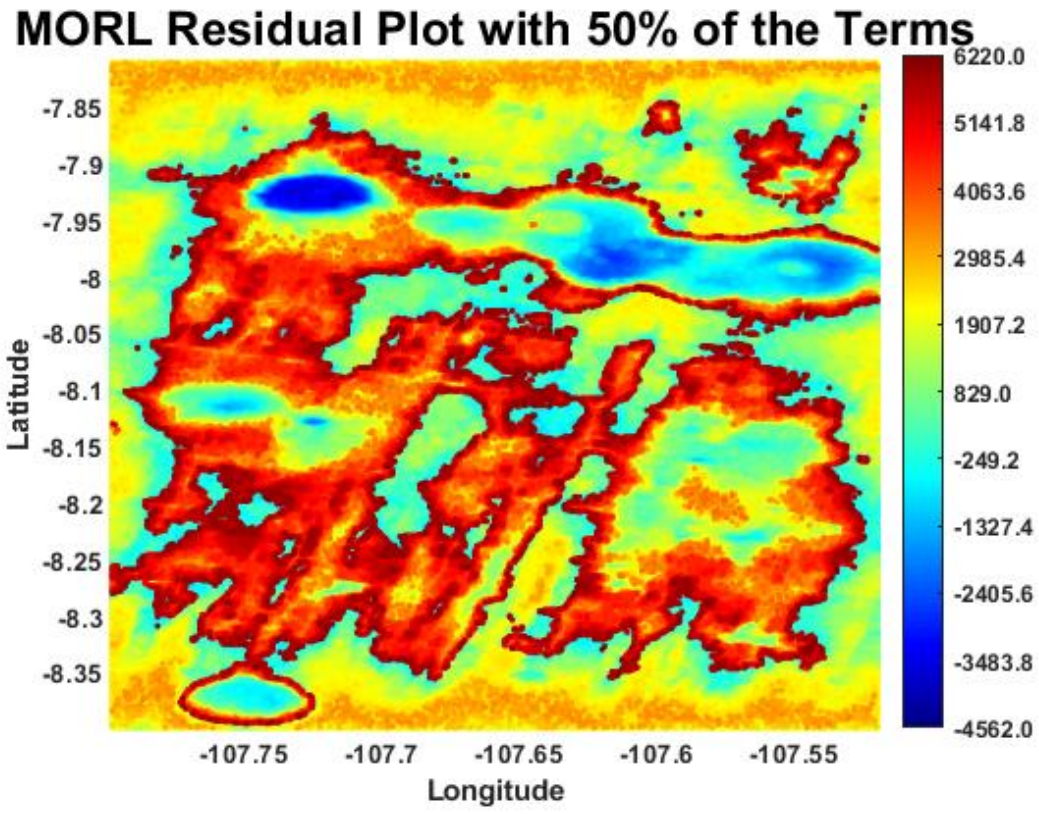

Figure 4.72 Residual of plot of larger area with only 50% of terms used for the Morlet Transform

Note: Units are in meters.

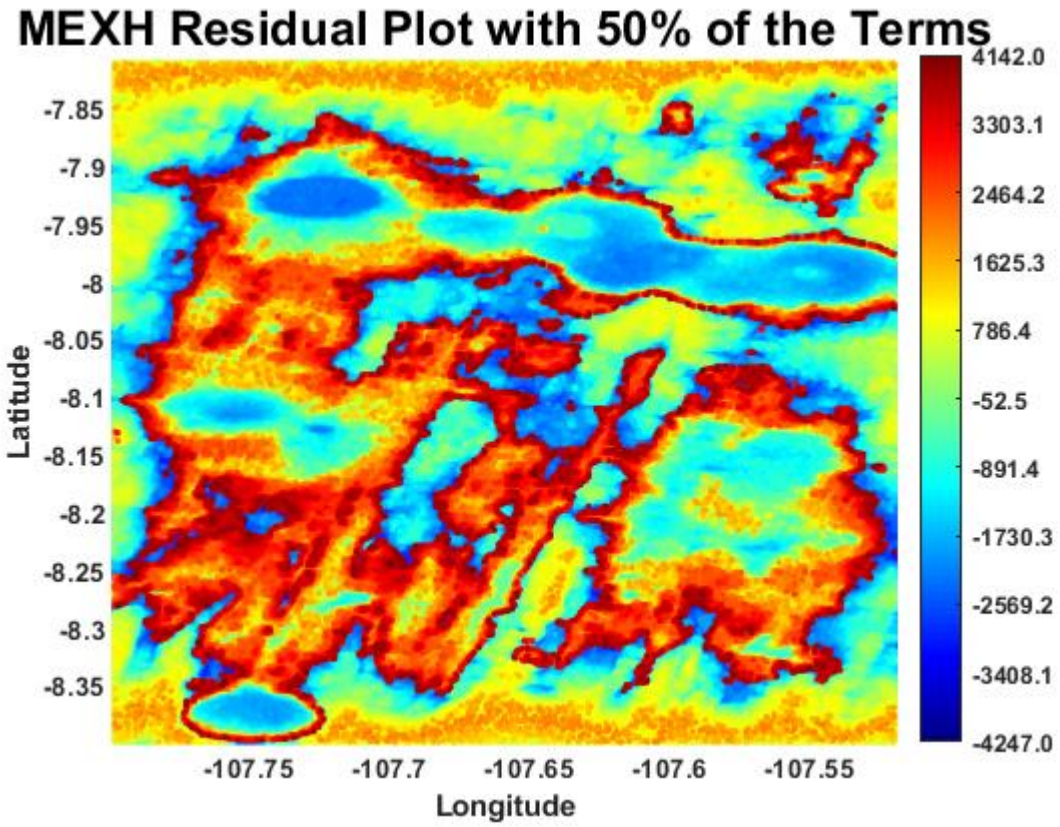

Figure 4.73 Residual of plot of larger area with only 50% of terms used for the MHW Transform

Note: Units are in meters.

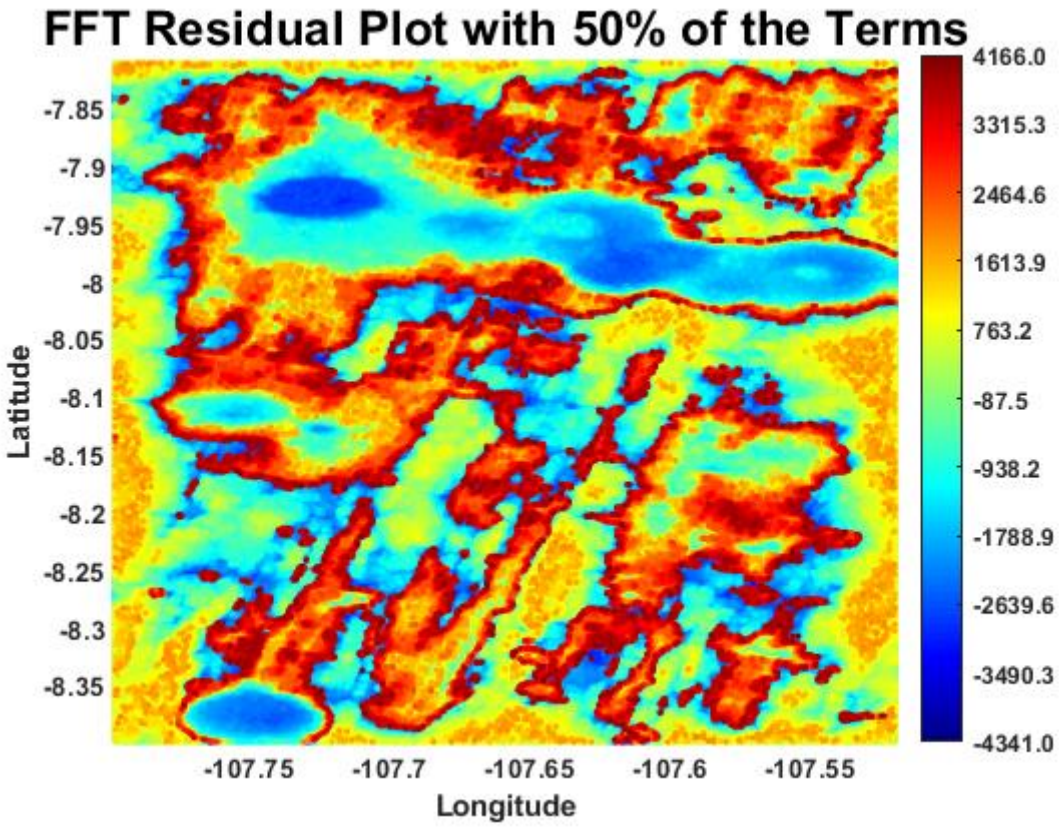

Figure 4.74 Residual of plot of larger area with only 50% of terms used for the FTT

Note: Units are in meters.

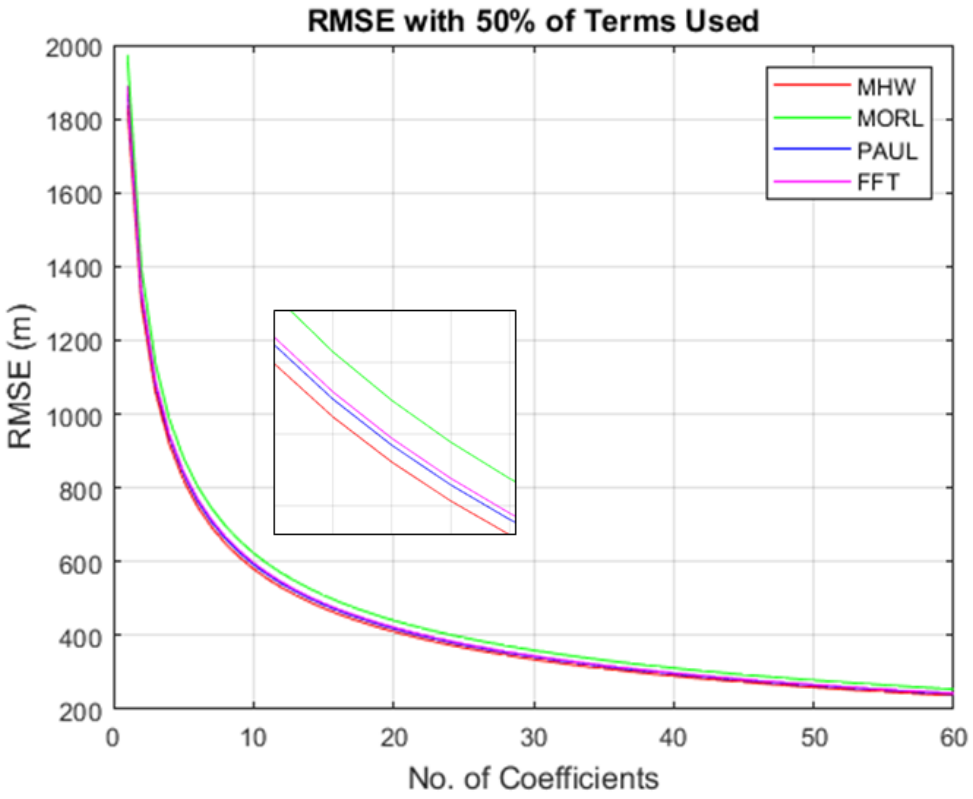

Figure 4.75 Error comparison between tested basis functions

Table 4.7 Student t-test Results

	Null Hypothesis 0 – Accept 1 – Reject	**P (Level of Confidence)**	**CONFIDENCE INTERVAL LOWER LIMIT**	**CONFIDENCE INTERVAL UPPER LIMIT**
MHW & FT	0	0.8919	-114.7938	100.0212
PAUL & FT	0	0.7197	-125.2971	86.7762
MORLET & FT	0	0.7898	-120.9798	92.2154

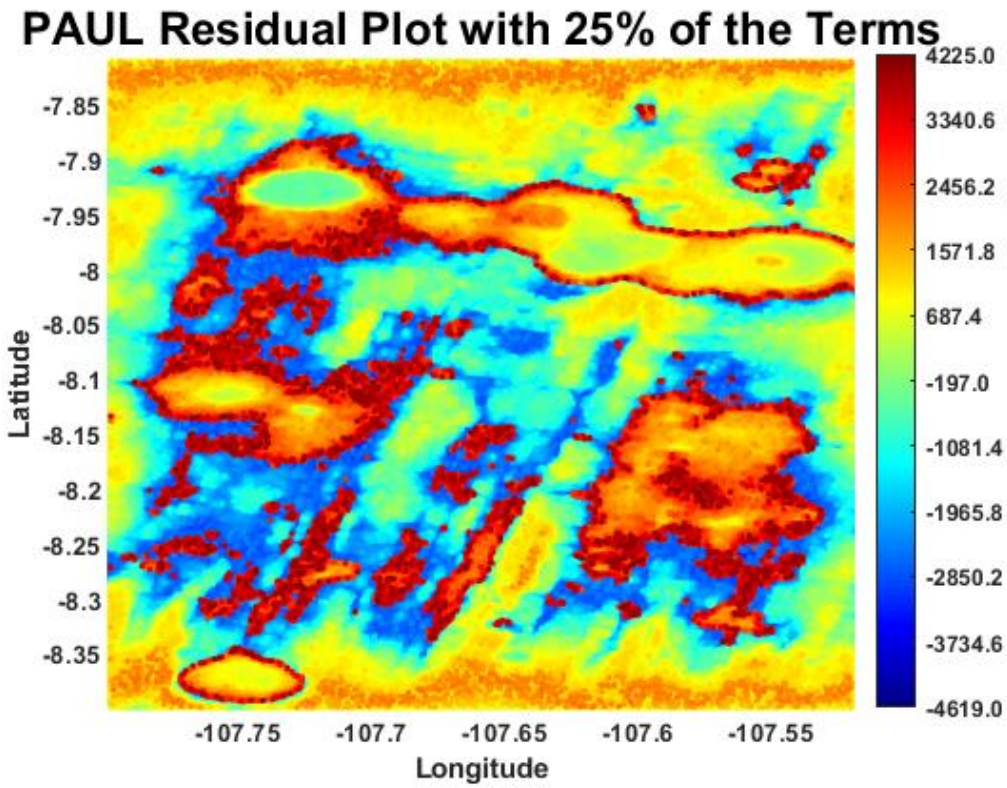

Figure 4.76 Residual of plot of larger area with only 25% of terms used for the Paul Transform

Note: Units are in meters.

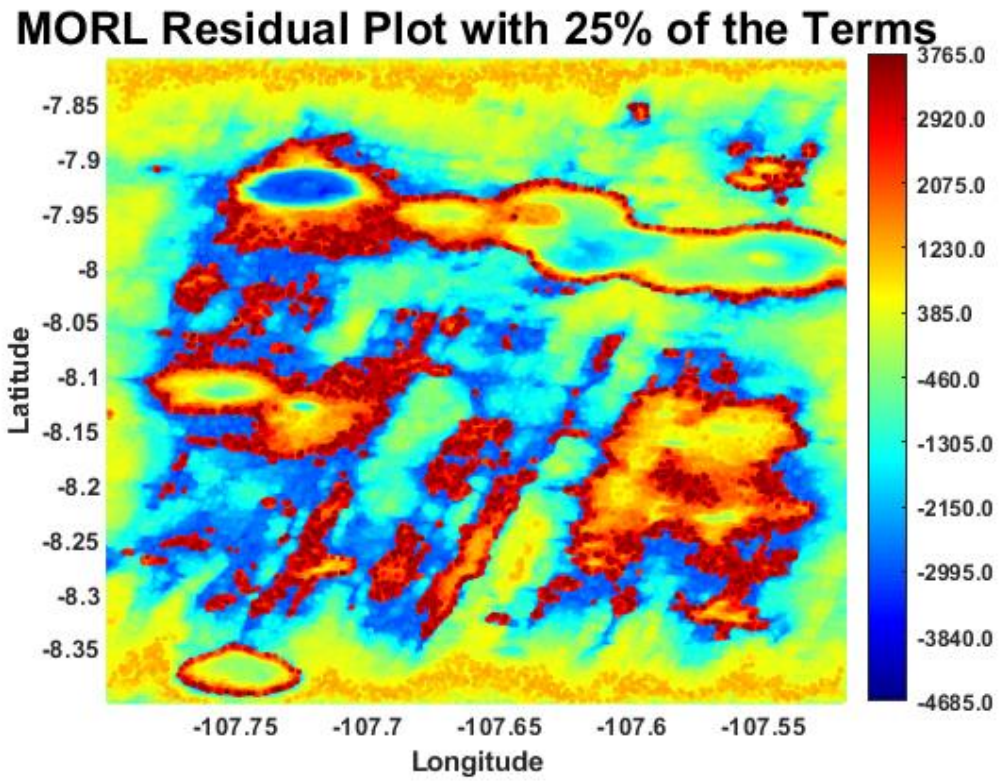

Figure 4.77 Residual of plot of larger area with only 25% of terms used for the Morlet Transform

Note: Units are in meters.

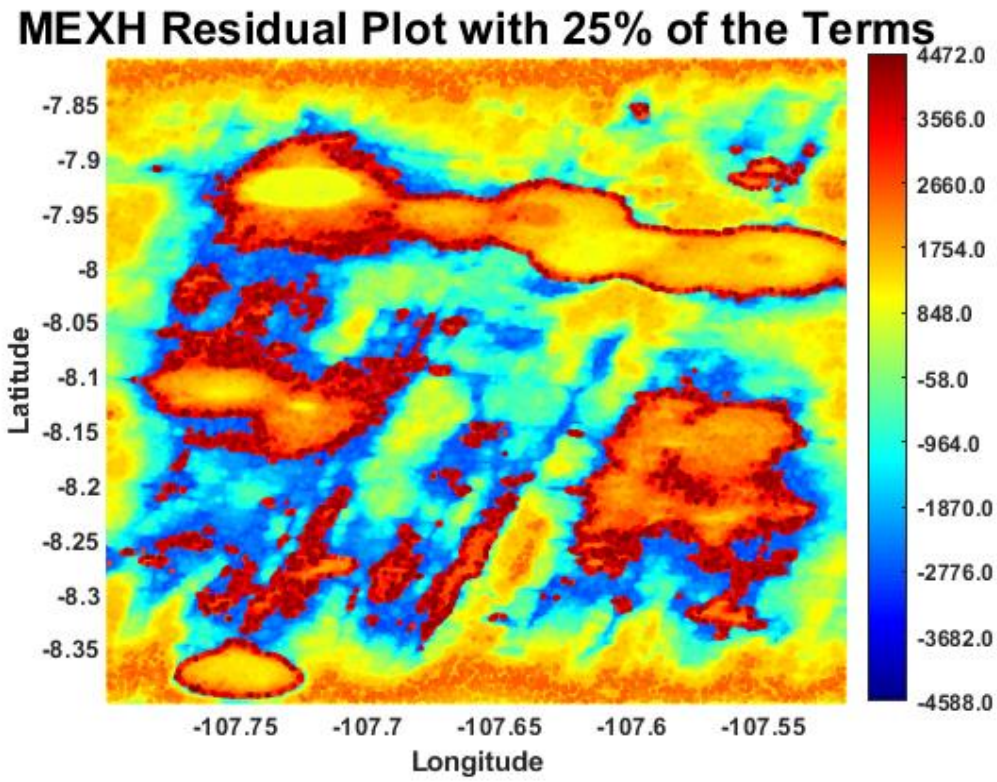

Figure 4.78 Residual of plot of larger area with only 25% of terms used for the MHW Transform

Note: Units are in meters.

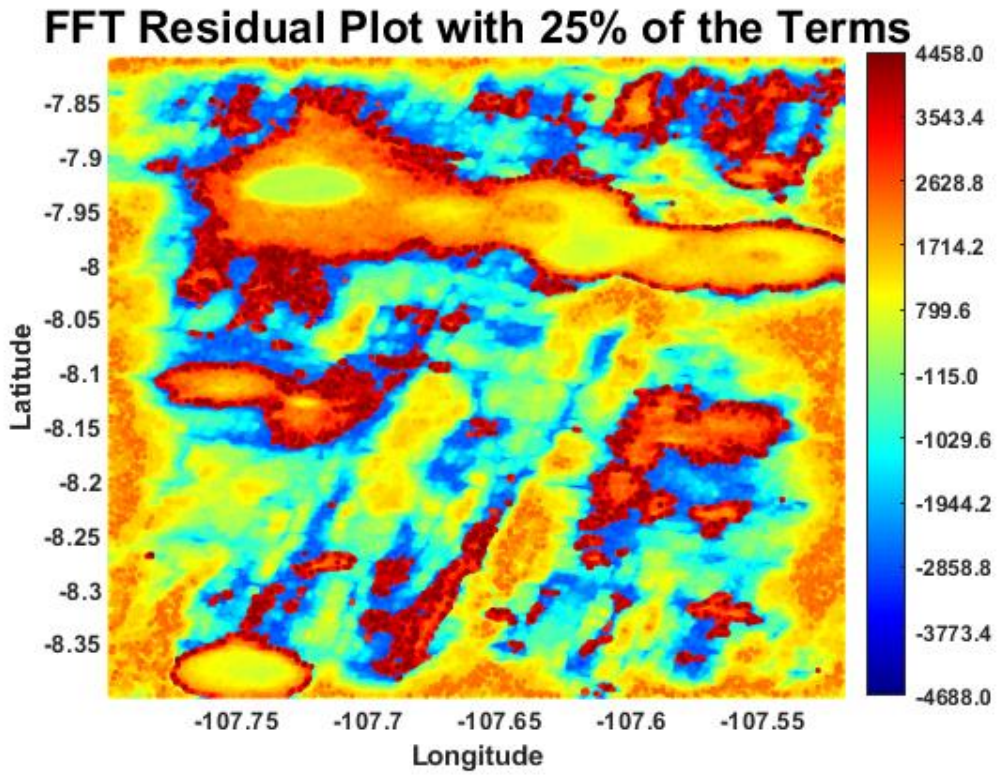

Figure 4.79 Residual of plot of larger area with only 25% of terms used for the MHW Transform

Note: Units are in meters.

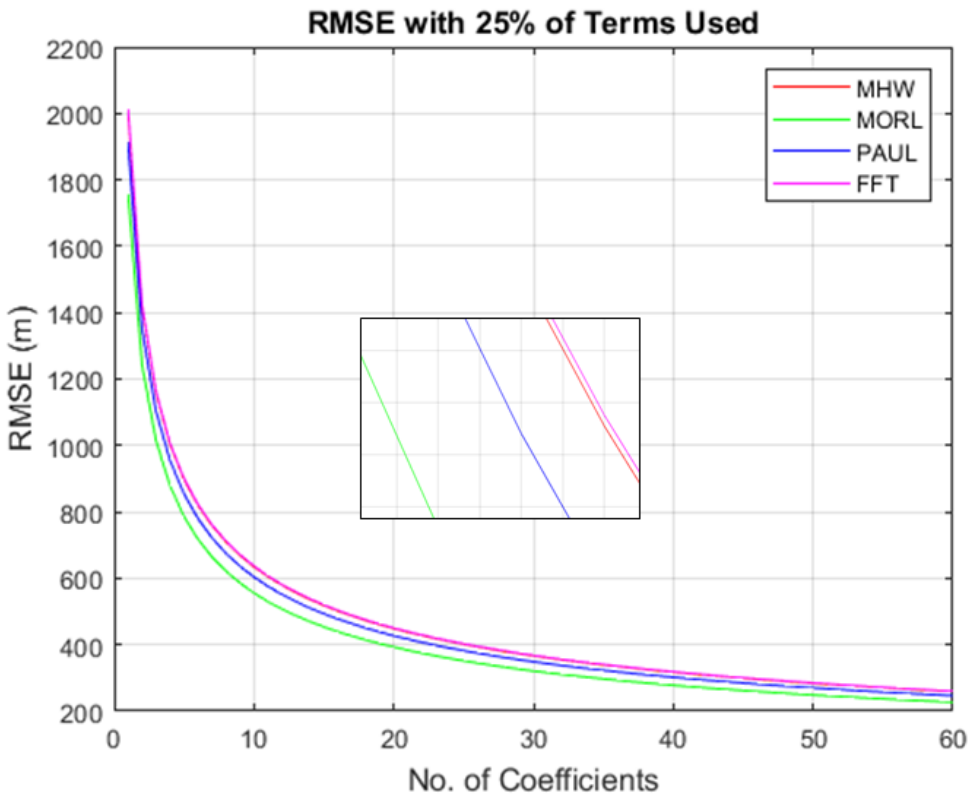

Figure 4.80 Error comparison between tested basis functions

Table 4.8 Student t-test Results

	Null Hypothesis 0 – Accept 1 – Reject	**P (Level of Confidence)**	**CONFIDENCE INTERVAL LOWER LIMIT**	**CONFIDENCE INTERVAL UPPER LIMIT**
MHW & FT	0	0.9768	-112.3739	109.1174
PAUL & FT	0	0.2527	-164.5181	43.6767
MORLET & FT	0	0.6525	-132.7292	83.4457

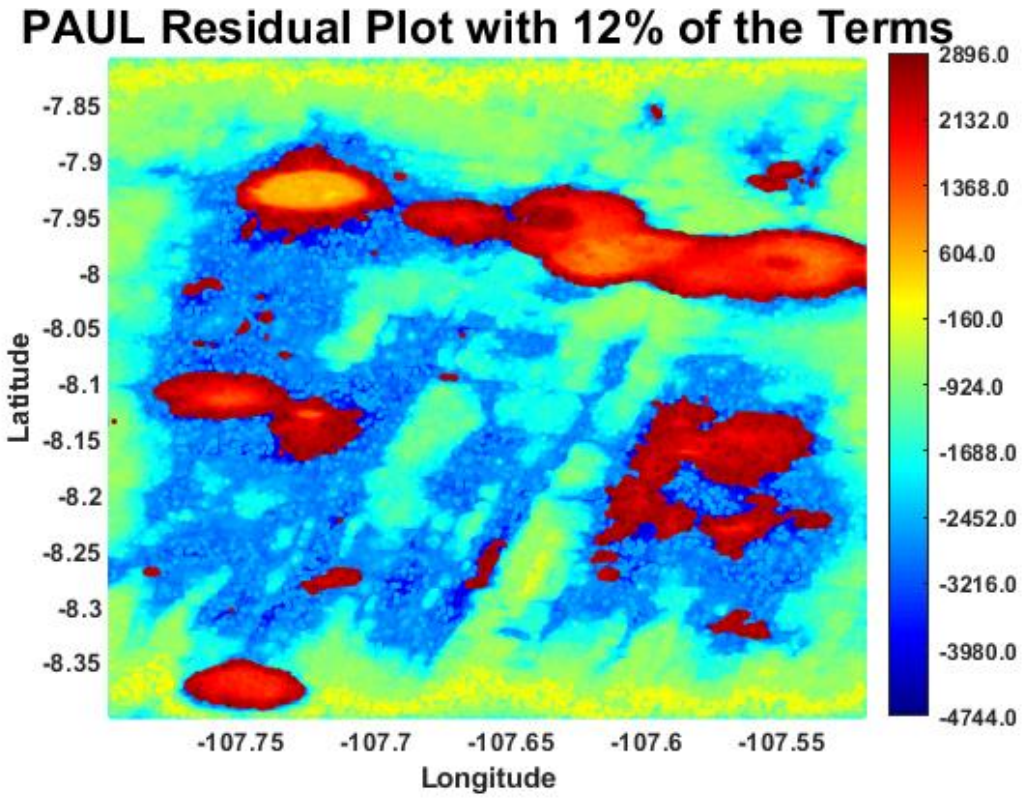

Figure 4.81 Residual of plot of larger area with only 12% of terms used for the Paul Transform

Note: Units are in meters.

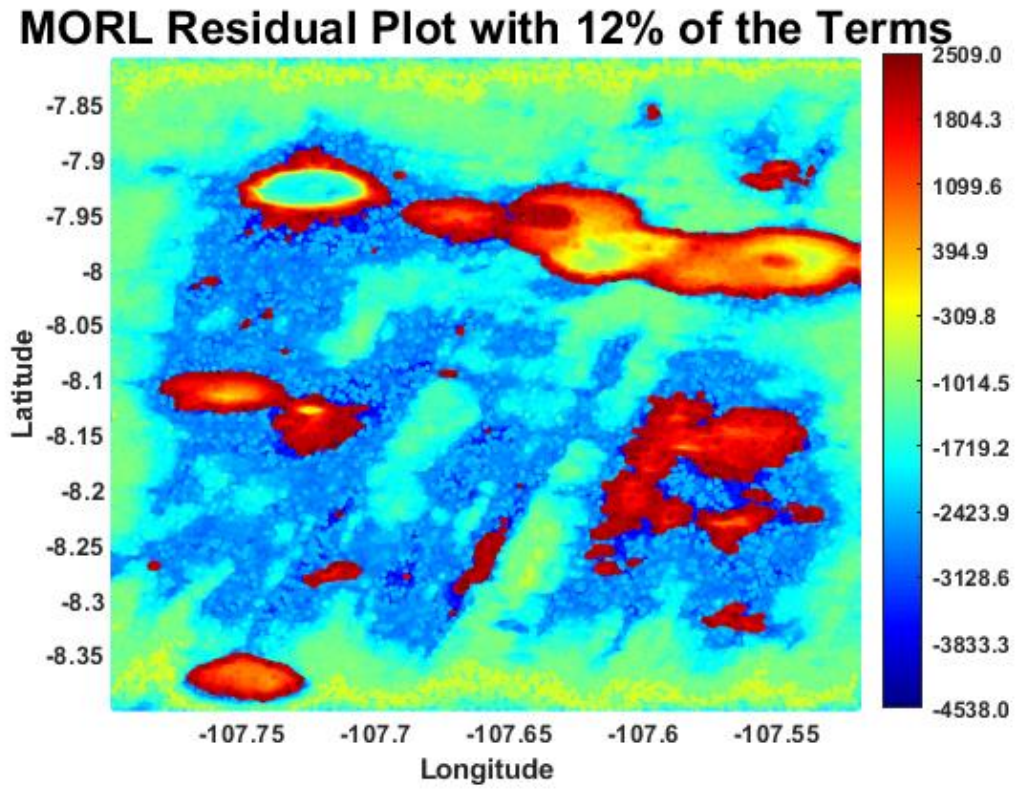

Figure 4.82 Residual of plot of larger area with only 12% of terms used for the Morlet Transform

Note: Units are in meters.

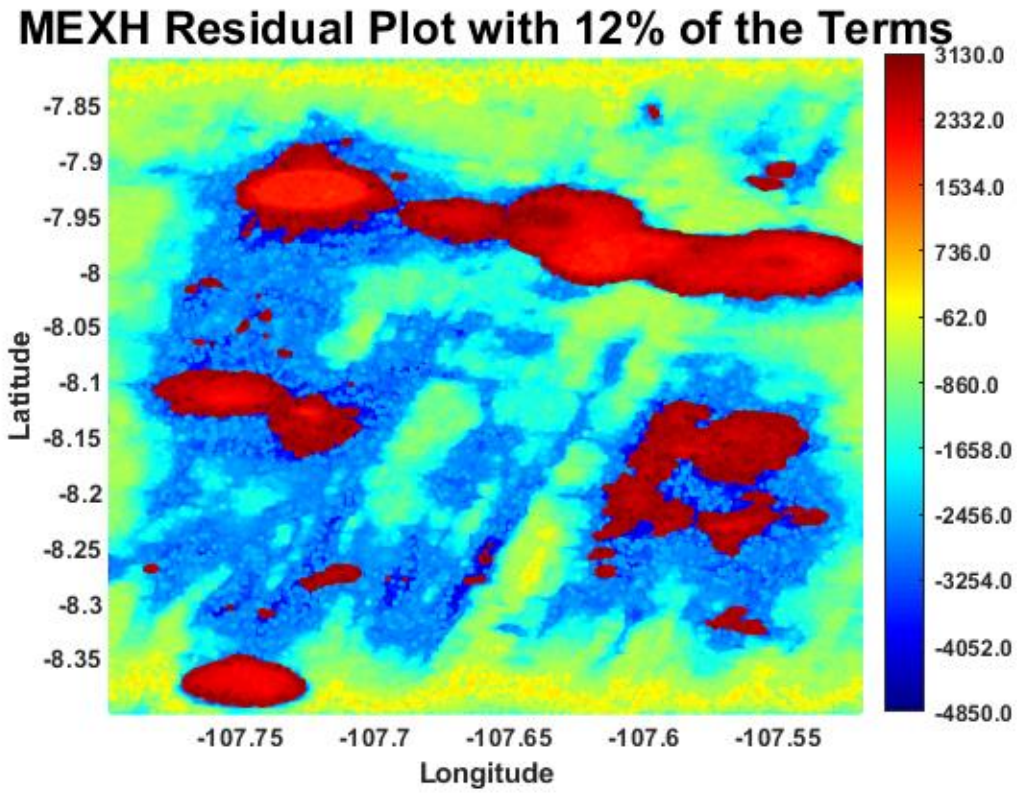

Figure 4.83 Residual of plot of larger area with only 12% of terms used for the MHW Transform

Note: Units are in meters.

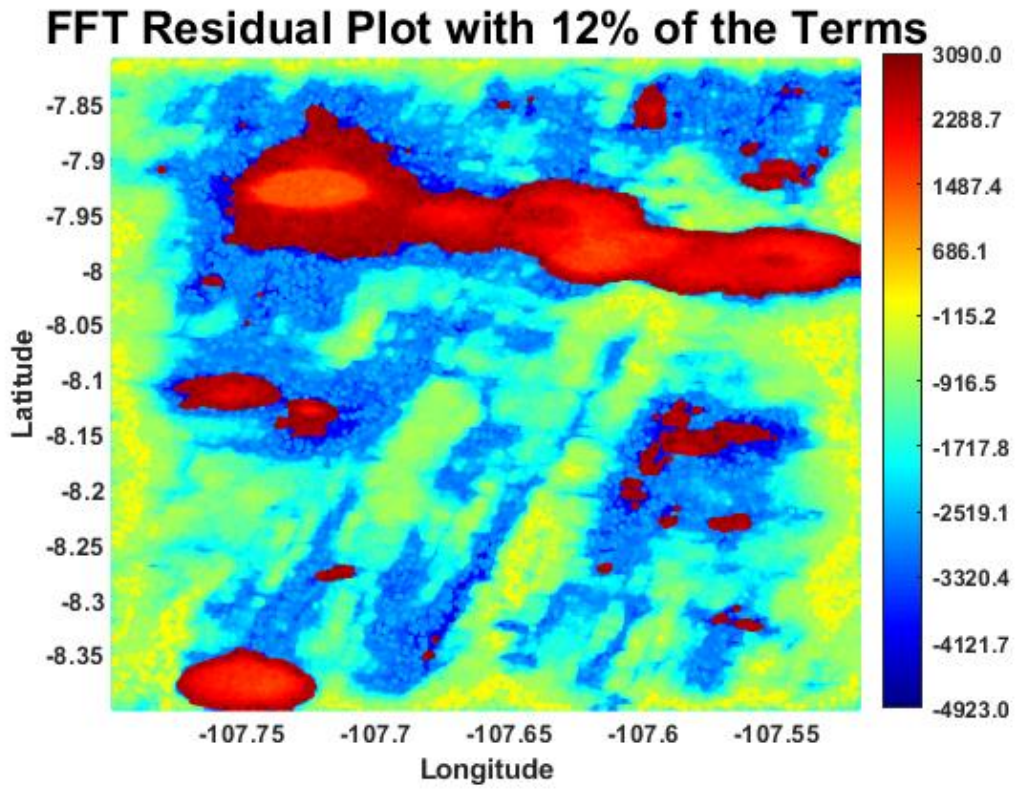

Figure 4.84 Residual of plot of larger area with only 12% of terms used for the FFT

Note: Units are in meters.

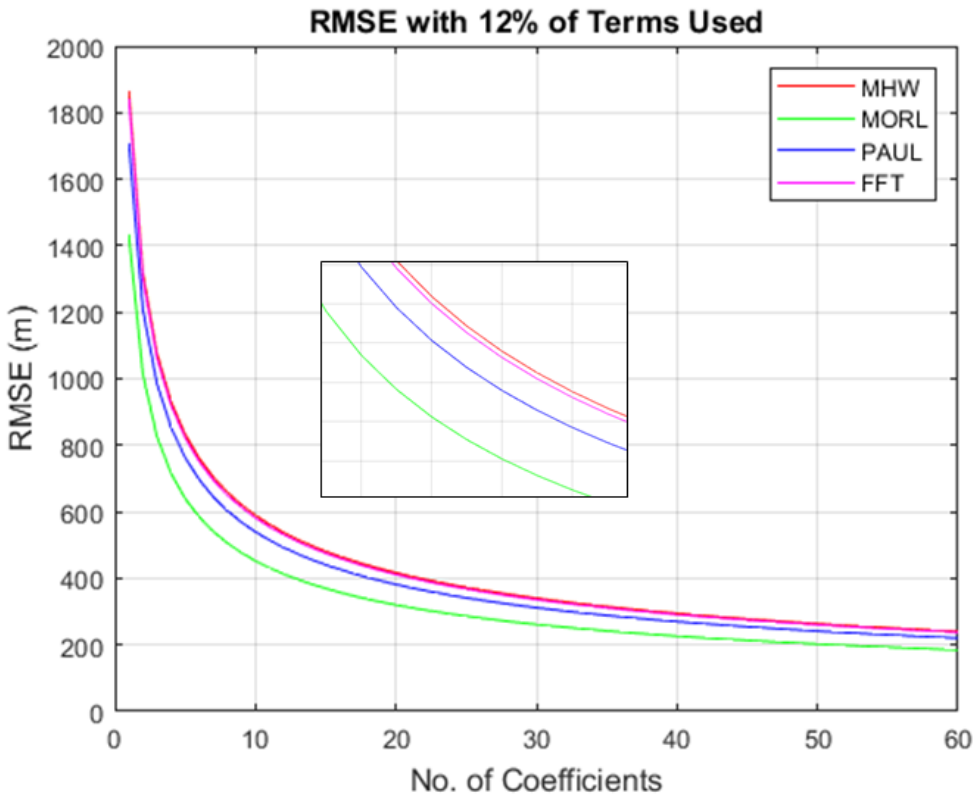

Figure 4.85 Error comparison between tested basis functions

Table 4.9 Student t-test Results

	Null Hypothesis 0 – Accept 1 – Reject	**P (Level of Confidence)**	**CONFIDENCE INTERVAL LOWER LIMIT**	**CONFIDENCE INTERVAL UPPER LIMIT**
MHW & FT	0	0.9078	-96.0080	107.9576
PAUL & FT	1	0.0385	-186.6395	-5.1559
MORLET & FT	0	0.5284	-128.8902	66.4961

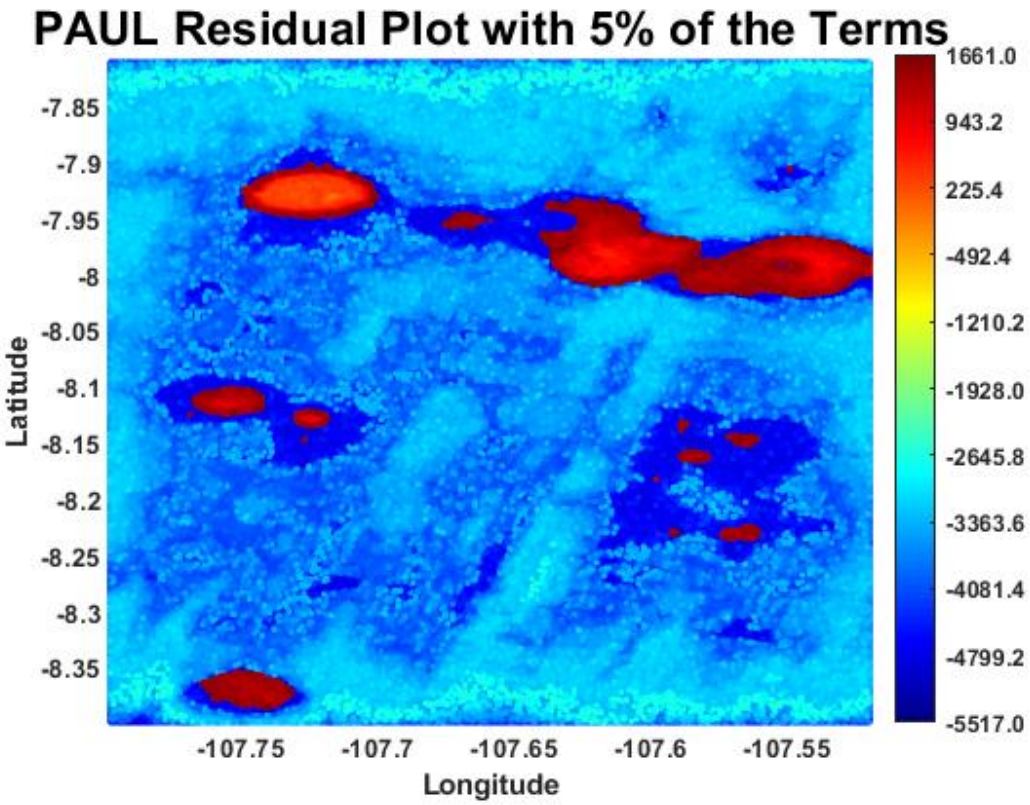

Figure 4.86 Residual of plot of larger area with only 5% of terms used for the Paul Transform

Note: Units are in meters.

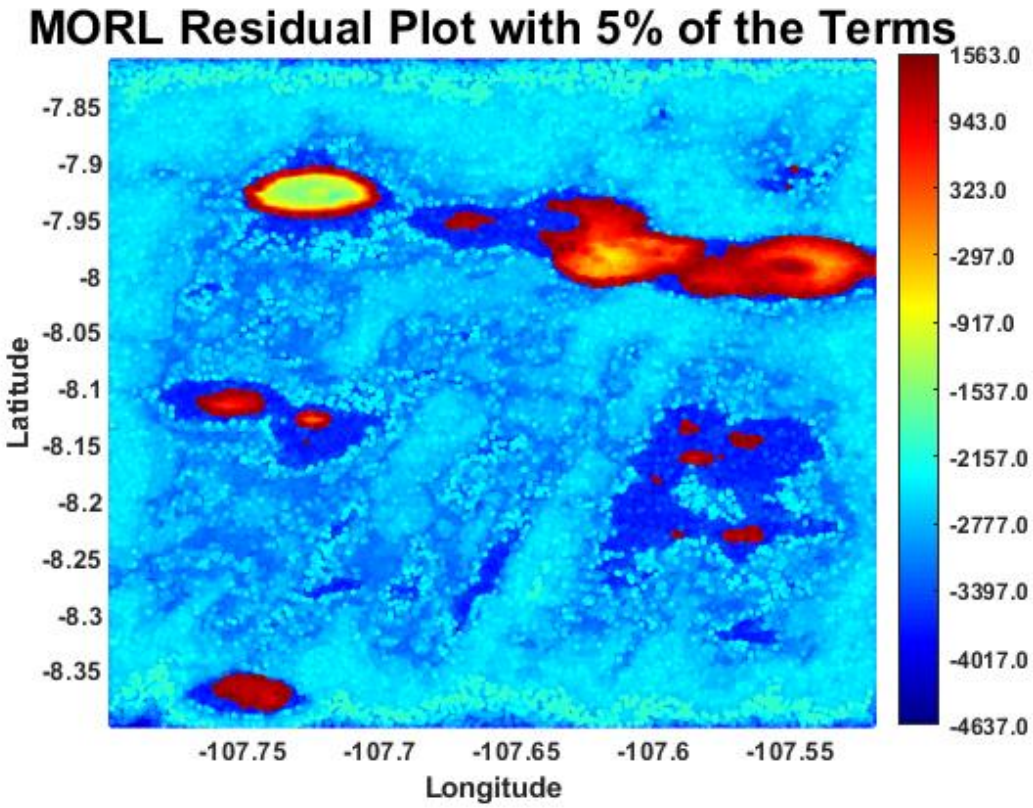

Figure 4.87 Residual of plot of larger area with only 5% of terms used for the Morlet Transform

Note: Units are in meters.

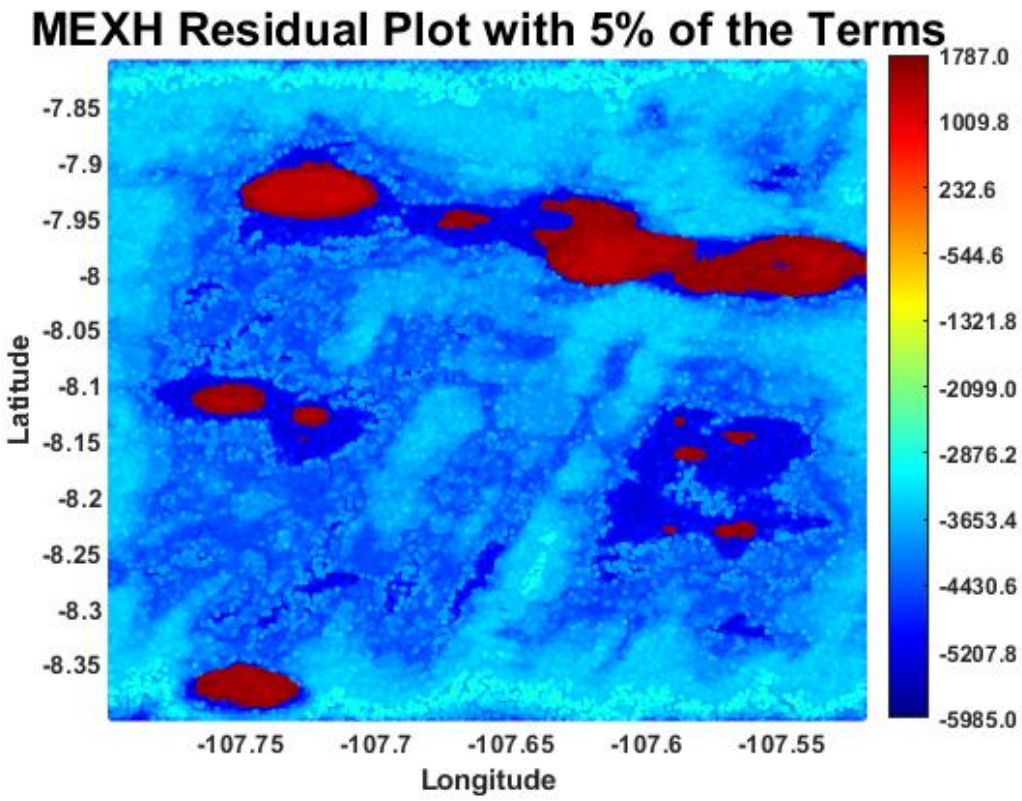

Figure 4.88 Residual of plot of larger area with only 5% of terms used for the MHW Transform

Note: Units are in meters.

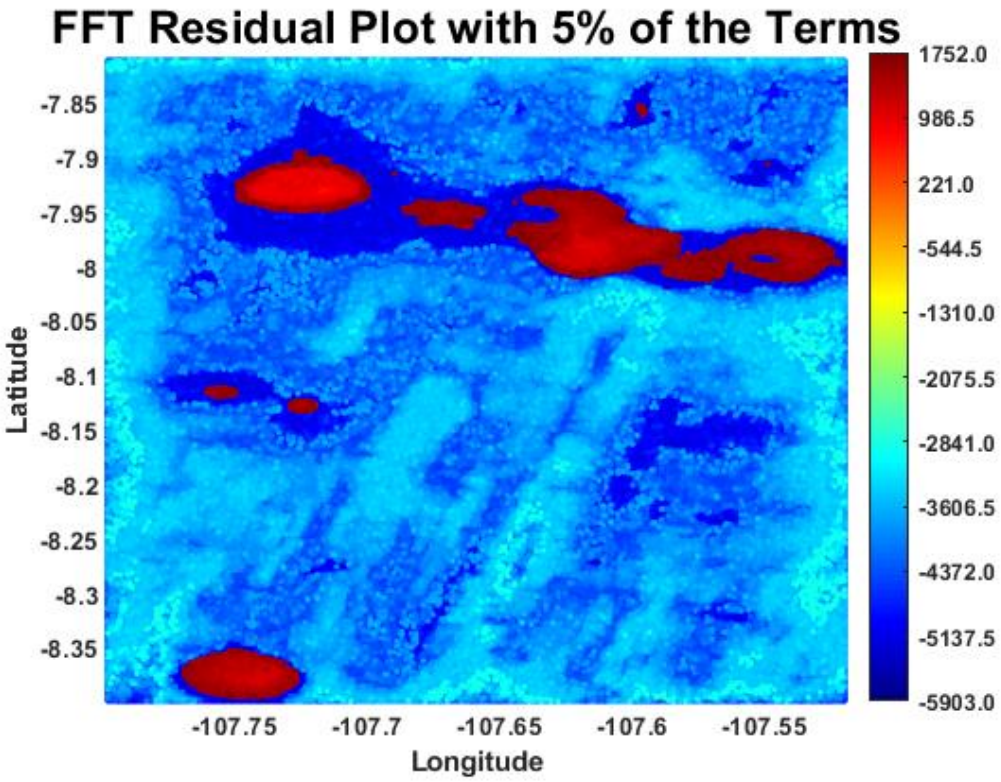

Figure 4.89 Residual of plot of larger area with only 5% of terms used for the FFT

Note: Units are in meters.

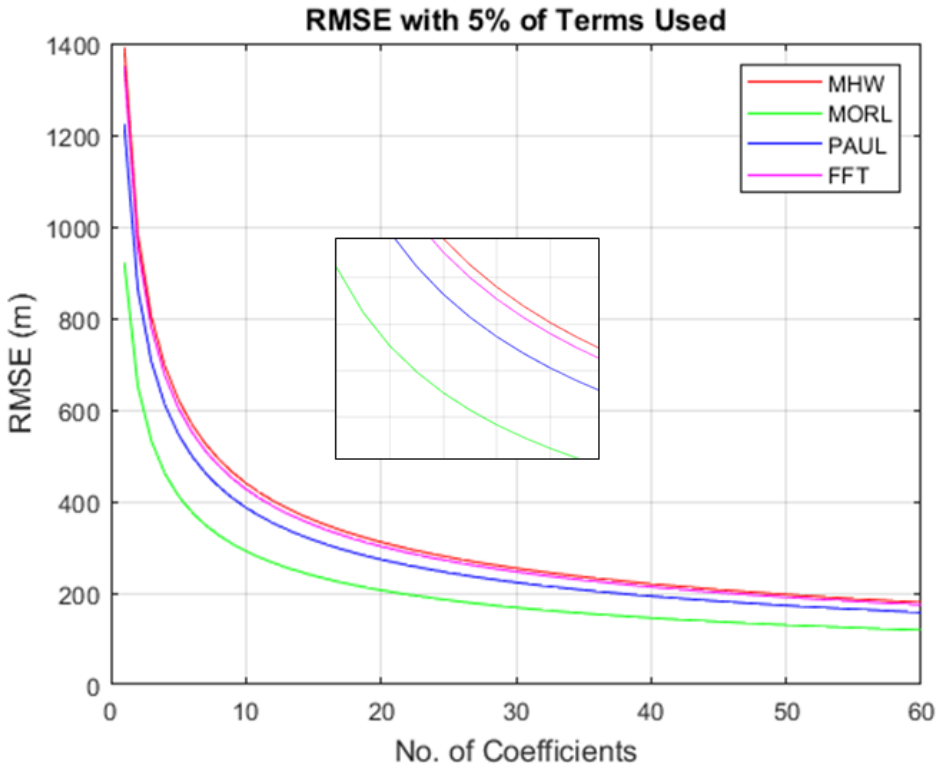

Figure 4.90 Error comparison between tested basis functions

Table 4.10 Student t-test Results

	Null Hypothesis 0 – Accept 1 – Reject	**P (Level of Confidence)**	**CONFIDENCE INTERVAL LOWER LIMIT**	**CONFIDENCE INTERVAL UPPER LIMIT**
MHW & FT	0	0.8000	-65.8268	85.1918
PAUL & FT	1	0.0022	-164.3492	-37.0061
MORLET & FT	0	0.4025	-101.0208	40.8345

4.14 De-noising with a Weiner Filter

As a quick aside, an attempt is made to de-noise a signal in both the Fourier and Continuous wavelet domains utilizing a Wiener filter. The procedure set forth by Perez-Rendon and Robles, 2004, was used. The second example from authors' was tested first. The signal is non-stationary and one-dimensional. The signal is first blurred with a Gaussian filter with a pre-determined standard deviation and random white noise, both of which were implemented via built-in MATLAB functions. The signal was then restored using via deconvolution in both the continuous wavelet and Fourier domains following the formulae provided by the authors. The result differed from that of the authors, in that, their results were near identical reproductions of the original test signal and the solution here was not. It is likely that the authors added a few other steps not listed for brevity.

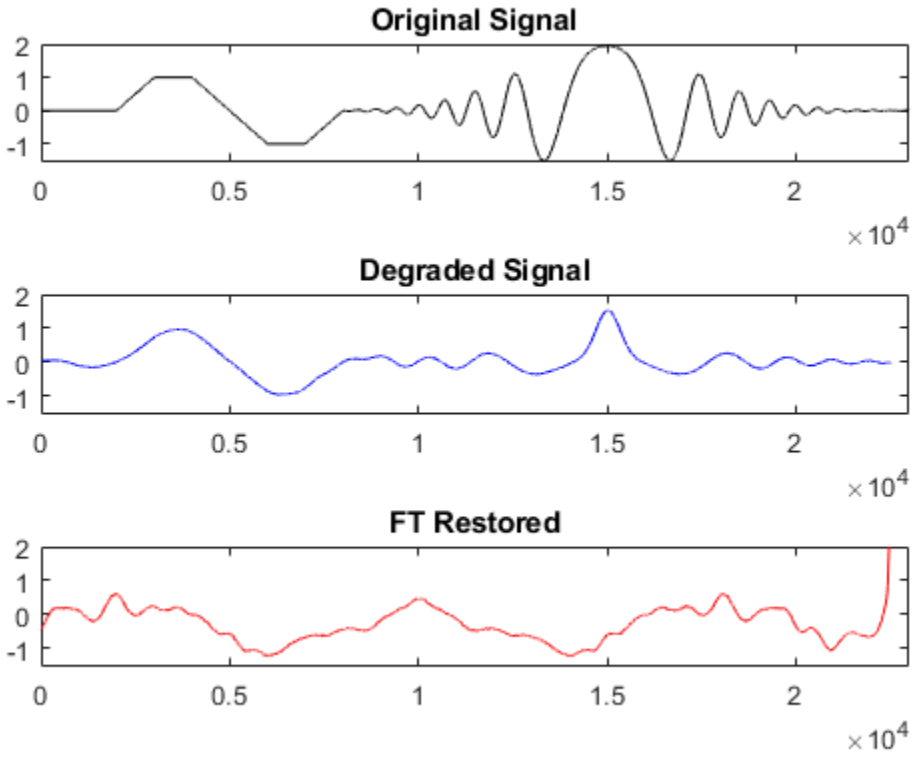

Figure 4.91 Reconstruction of a noisy signal via FFT deconvolution

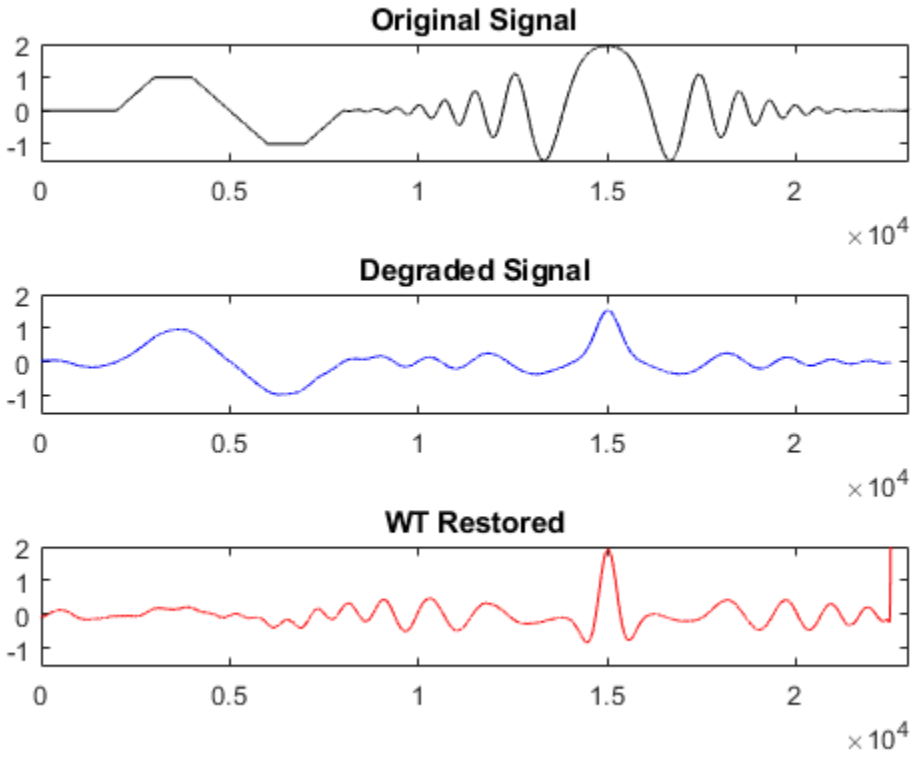

Figure 4.92 Reconstruction of a noisy signal via CWT deconvolution

From the two plots, it is apparent that the CWT was better able at identifying the main lobe in the degraded signal; and the FFT was not able to do so. To continue testing this method, a 2D signal was tested from the SEPR dataset that included a small seamount. See figure 4.93 below.

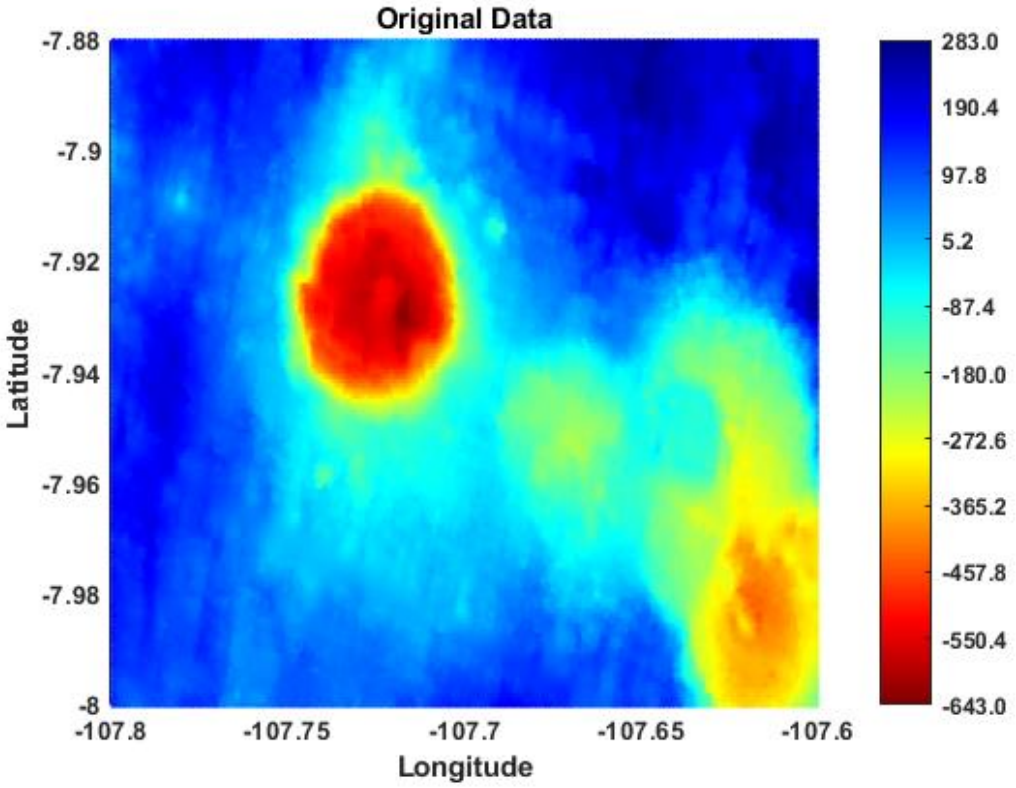

Figure 4.93 Original 2D signal in the SEPR region

Note: Units are in meters.

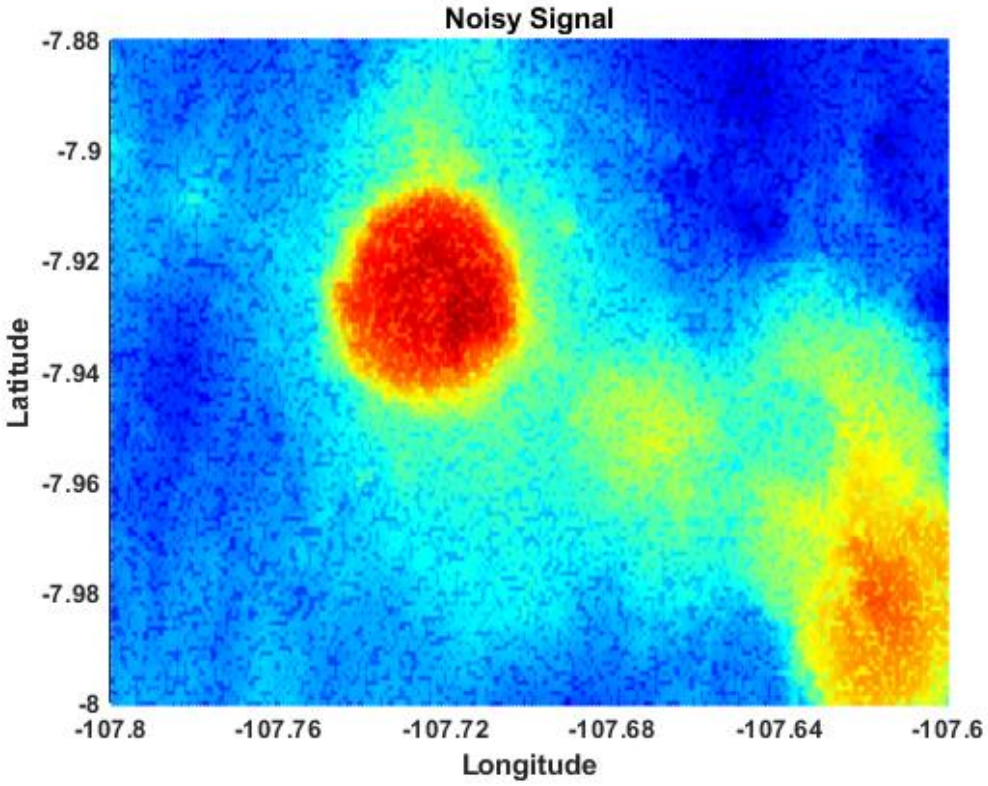

Figure 4.94 Degraded signal with a Gaussian blur in the SEPR region

Signal restoration was attempted in both the Fourier and CWT domains, however, as the Fourier deconvolution did produced a viable reconstruction, a plot for it is not given. Figure 4.95 below is the reconstructed signal in the CWT domain, though.

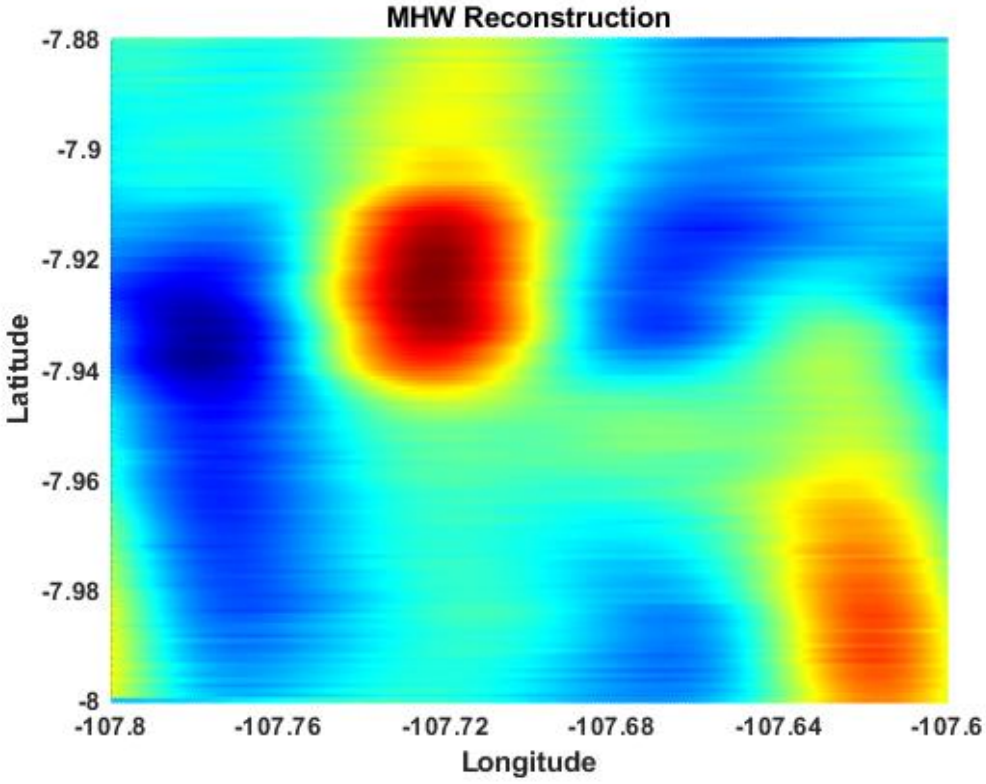

Figure 4.95 Reconstruction of a noisy 2D signal via CWT deconvolution in the SEPR region

The CWT deconvolution was clearly able to remove noise and reconstruct the key features in the original dataset plot. In order to better appreciate the CWT reconstruction an alternate view of the original (with noise) and reconstructed plots is shown.

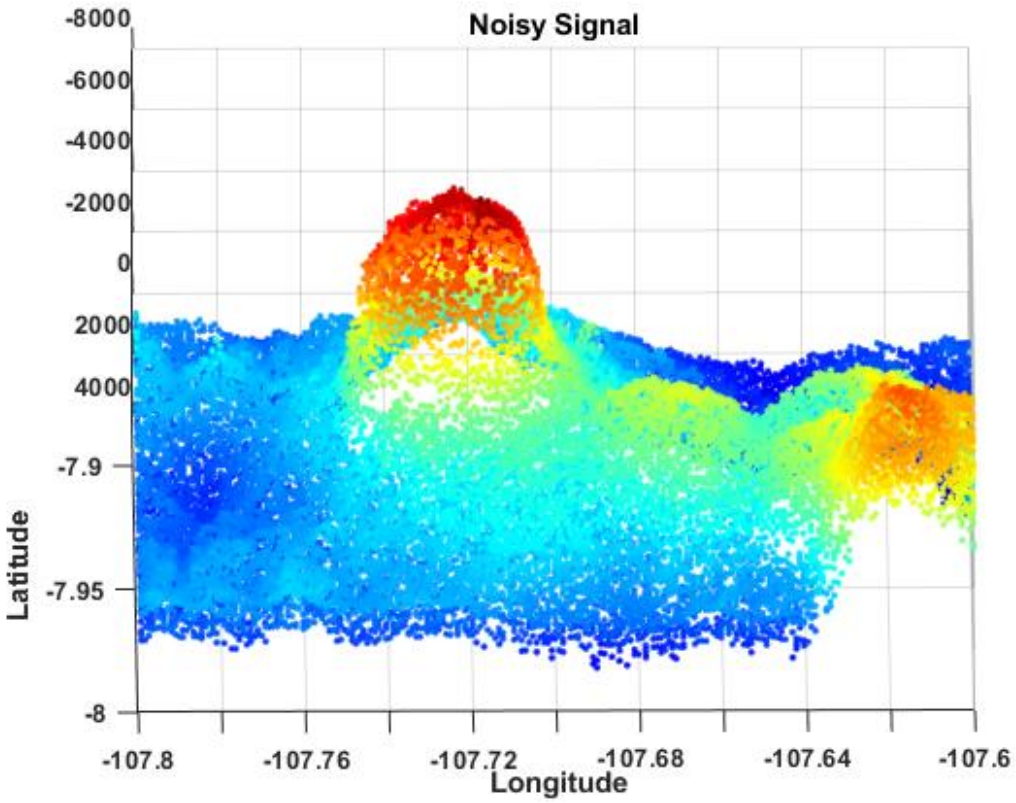

Figure 4.96 Alternate view of the degraded signal with a Gaussian blur in the SEPR region

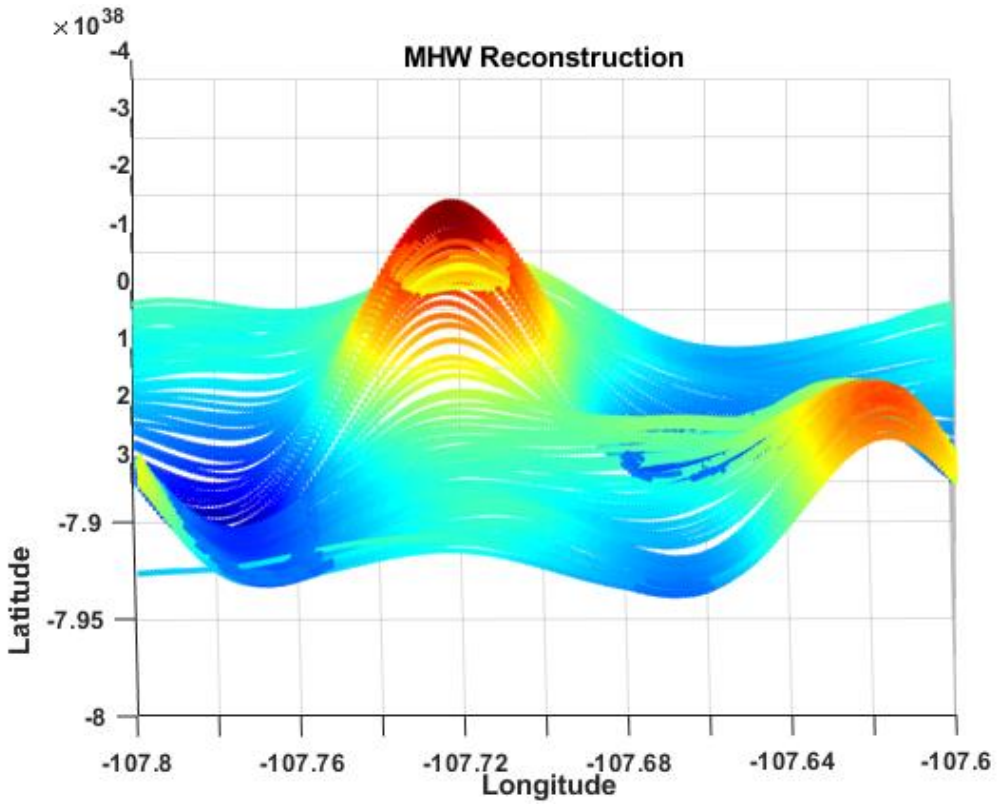

Figure 4.97 Alternate view of the CWT restored signal in the SEPR region

The power of the CWT deconvolution method is apparent. However, as already mentioned previously in this chapter, those calculations are taxing and thus the CWT inverse is not computed directly in MATLAB and is instead replaced with CWT in the Fourier domain.

5.1 Discussion

5.1.1 Initial Tests: Simple 1D Functions

Prior to analyzing the more complex and robust 2D derived bathymetry problem, a simple reconstruction of a basic function was tested, in this case the step function. As mentioned in the results section, in order to show that fewer terms were required by a wavelet as opposed to the Fourier transform in the reconstruction of a signal, the Fourier transform was expressed as a sum of sines and cosines. Whereas with the wavelets, the transform was taken followed by the inverse transform for an increasing number of terms over several iterations. Further, as wavelets are local in nature while the FT is not, a Hamming function was applied to the FT in order to window, and thus provide a more comparable side-by-side analysis. Significant reduction of error was noted between the MHW and the FT and more than twice that between the Daubechies-1 wavelet and the FT while utilizing fewer reconstruction terms (See figure 4.1). This was a clear advantage in simple reconstruction of a simple geometric function.

As the Gibb's phenomenon is a known issue for FTs around discontinuities, an experiment was conducted to determine how many terms were required to be included in signal reconstruction in order to minimize over shoot. Maybe of more importance, FT overshoot was plotted alongside with continuous and discrete wavelets whose Gibb's effects, though are highly negligible. Figure 4.3 clearly demonstrated the superiority of wavelets over FTs in this regard. This was an important result as underwater bathymetric features such as seamounts and spreading centers could behave like discontinuities depending upon their shape and the steepness of their incline/decline.

Further comparisons were made between the basis functions, by testing their utility of reconstructing the potentials of the monopole and cone, term-by-term. In both cases, wavelets outperformed the FT based on RMS error results (figures 4.12 and 4.14). With respect to the monopole potential, RMS error was negligible. However, for an error 0.04 cm^2s^{-2} the Daubechies-1 wavelet required 4 terms, Paul 6 terms, Morlet 7 terms, the Mexican Hat 8 terms and the FT 16 terms. For the case of the cone, wavelets had an RMS error of 40 (cm^2s^{-2}) with about 23 terms, the Morlet with 26 terms while the FT needed 33 terms for the same error level. Although monopole reconstruction RMS error showed a clear distinction between the continuous and discrete wavelets, little statistical distinction could be made between the wavelets for the case of the cone. The reason is likely due to the following: due to the nature of the monopole's geometry, relative error differences were slim. With the cone, a larger relative error was computed. Thus, the difference between the wavelets only appears to be minimal. Regardless, the results of these tests offered further evidence towards supporting the hypothesis that wavelets are the better choice for a basis function in the inversion of satellite altimetry to bathymetry.

With basic testing completed, a data set from the South Eastern Pacific Range was examined, first as a slice of data and then as a 2D area. Prior to actual inversion testing, though, an initial test was conducted by transforming the signals and then taking the inverse transform. This was a simple reconstruction effort and was done on a term-by-term basis. RMS error results showed wavelets performing better but no longer at expected results based on the previous simple examples. It should be noted that the data set was previously filtered via a FFT. This may have impacted the effectiveness of the wavelets. For the 1D case for an RMS error of 5 meters, the Paul and Morlet wavelets

required 4 terms, the Mexican Hat 5 terms and the FT about 7 terms. As table 4.1 (Student t-test) suggests (the rejection of the null hypothesis), there was little statistical difference between the tested wavelets and the FT. For the 2D case, for an RMS error level of 10 meters, about 8 terms were required for all three tested wavelets and 12 terms for the FT. Similarly for the 2D case, the null hypothesis was accepted, thus showing little statistical difference again between the FT and the wavelets.

The final step was to compute the actual derived bathymetry. It has been noted that a solution to the wavelet of the monopole potential is not currently known and software such as GMT does not use wavelets. As such, a compromise was made to utilize the FFT to compute upward and downward continuation while using wavelets as filters for the gravity data. Further, it was not computationally feasible to compute RMS error on a term-by-term basis. To further exacerbate the issue, for the mentioned size of the data set, MATLAB computes the wavelet inverse transform across 34 different scales. It is true that only one scale and thus one computation required, but all scale computations must be computed in order to determine which will best approximate the area of interest. Should the terrain vary throughout the area, then several scales would likely be required. If then, one would like to see RMS error as a function of the number of terms used to produce the signal and limit the error test to only the first 60 terms, that same computer would need to run for over seventeen hours per continuous wavelet to be tested, excluding reset and analysis time. As such, a measure of error could not be made on a term-by-term basis, which may in fact have reduced the true measure of effectiveness of the wavelets over the FT.

Despite the apparent minimal error difference between the continuous wavelets and the FT (with two exceptions), much can still be said about the Morlet transform and the FT. With the large area of figure 4.30 considered, with only 5% of all terms used, a 100% increase in terms was needed by the FT to reach the same 200m RMS error by the Morlet. That is, the 200m error curve of the Morlet required an approximate 22 terms to reach as opposed to the approximate 45 terms by the FT. Further, for the smaller area focusing on the two key seamounts, the Morlet required an approximate 22 terms to reach the 400m error curve as opposed to 32 by the FT, a 50% increase in terms. For the larger area, the Morlet did, however, show some statistical difference when only 5 and 12 percent of the terms were considered. For these instances, the null hypothesis was rejected. That is, when dealing with sparser data sets, the Morlet transform does provide a clear advantage not only over the FT but also the Mexican Hat and Paul wavelets when computing derived bathymetry. Further, even though the rest of the test cases had the acceptance of the null hypothesis, P values (from the Student t-test) for the Morlet were always lower than those for the other two continuous wavelets.

The idea of computing residual plots was suggested in order to determine how each of the basis functions reconstructs a signal. The computation is direct. Take the original signal and subtract from it the reconstruction. It was not necessary to make this computation with all the reconstructions, however. For all the reconstructions previous to the six-step Smith and Sandwell inversions, it is plain to see how reconstruction works with the FT and wavelet basis functions. It has been stated that FTs are global functions and that wavelets are local in nature. As such, wavelet reconstructions will require fewer terms to achieve lower RMS error, as a signal is constructed one term at a time, following

the shape of the signal, while a FT will attempt to produce the whole signal regardless of the number of terms. For the FT, as the number of terms increases, the closer in shape you get to the original signal. This is easily visible with 1D signals and is a clear indicator as to why wavelets had lower RMS error with respect to the number of terms used in signal reconstruction.

In 2D signals, such as with the inversion of gravity to bathymetry, this is not so clear. Residual plots, then, allow us to understand how the signal is produced and why RMS error, in particular for the Morlet wavelet, was lower than that of the FT. Beginning with the larger area (figures 4.71-4.90), a comparison between each of the basis function residual plots with 5% of the terms demonstrates, that with only a few percent of all the terms, continuous wavelets picked out more features than the FT. The same was true when the smaller area that focused on two seamounts was analyzed. As the colorbar indicated, the ranges of values were similar, but the wavelets again were able to better identify the features with fewer terms than the FT. It is here then, that the advantage of locality is demonstrated. It is becoming increasingly clear that locality gives wavelet transforms an edge over FTs in identifying the key features of an area. We must then recall, that at this point wavelets were only used to filter gravity data prior to inversion into bathymetry. The stage is thus set to continue towards a continuity solution in the wavelet domain to determine whether or not an even greater advantage is feasible.

The different basis functions were also tested for their ability to remove noise from a signal. Refer to figures 4.6-4.8 for a visual aid. A slice of data from SEPR was used for this task. Gaussian noise was added to the signal. The FT did nothing to remove the noise from the signal. Whereas the Daubechies wavelet family allowed for greater

control of noise removal via examination of the approximation and detail coefficients, the continuous wavelet, in this case the MHW, quickly and effectively removed the noise and produced a fair approximation to the original signal. Nonetheless, with a little effort, a discrete wavelet such Daubechies-1, can excel in this capacity.

5.1.1.1 Analytical vs. Numerical Solutions

Numerical solutions are a necessary tool used for computing difficult and seemingly unsolvable problems which has enhanced our ability to model a large number of phenomena including atmospheric and oceanic currents, engineering problems and biological patterns. It is, however, not without fault as error is always introduced with numerical approaches, even as computing power has increased allowing for a greater number of terms to be solved, thereby decreasing the amount of error. With the advent of computers and their exponential growth in processing speed, a trend of not attempting to analytically approach a problem is quickly increasing as significant amounts of time can be shifted to other efforts. As was reported previously in the results chapter, a combination of analytical and numerical modeling can reduce the amount of error introduced. Further, as initial testing demonstrated, the blended analytical/numerical approach solution to the Mexican Hat wavelet transform of the Newtonian potential gave a smaller error than the two purely numerical approaches computed for a slice of area of ocean topography located in the SEPR. This type of solution also acted as a baseline to the result that could be expected when numerical tools from the MATLAB toolbox and Generic Mapping Tool (GMT) were used to compute predicted bathymetry for each of the three tested continuous wavelet basis functions.

Although the hypothesis tested true, it was not at the expected amount of reduction of error, as for the most part, there was little to no statistical difference between the FFT and the tested continuous wavelets. The reasons for this, however, are listed. A wavelet solution to upward and downward continuation is as yet believed to be unsolved. This is the case as there is no known solution for a continuous wavelet transform of a monopole, which is a key component to solving downward continuation. Certain methods can be employed such as followed in this dissertation based on the technique employed by Abedi, 2014 (using discrete wavelets), where the wavelets were used to filter gravity data prior taking the known FFT based computations of continuity. Although there was some success there, it is conceivable that a pure wavelet approach to predicted bathymetry is required to achieve the hypothesized reduction of error.

It is also necessary to look at filtering raw satellite data using wavelets as opposed to FFTs. As was shown by Perez-Rendon and Robles (2004) and the work presented here, wavelets, both continuous and discrete, are superior at removing noise from a signal compared to the Fourier transform. Wavelets, however, are computationally more expensive and the denoising approach via convolution/deconvolution are taxing. Nonetheless, with increased computer processing power, this may soon be an issue of the past. A combination of noise removal via wavelets and a wavelet solution to continuity may be the key to not only achieving greater reductions in predicted bathymetry error with newer more dense satellite observations but also with older more sparse data sets. Once these approaches are complete, they could be applied to other transforms such as ridgelets. The ridgelet transform utilizes the relationship between the radon transform, which allows for directional control, and the FFT and continuous wavelets. Techniques

that utilize ridgelets, with the Mexican Hat transform as the basis function, are already being employed by geologists studying ocean features (Nathan J. Downey, 2007).

5.2 Conclusions

Based off of the results obtained in this study, at every step, wavelet transforms demonstrated a clear ability to outperform the Fourier Transform in signal reconstruction and later in the computations of inversion from a gravity to a bathymetric signal. Although in the latter part of the study, inversion via wavelet filtering produced only seemingly small increases in performance, when only 5% of all coefficients were considered, the FT required double the terms as the Morlet in order to reach the same 200m RMS error curve line. Similarly, for the smaller area, a 50% increase in terms was required by the FT to reach a 400m error curve than the Morlet wavelet. In this case, the Morlet wavelet transform demonstrated a clear superiority against the other two tested continuous wavelets as well as the FT when dealing with a limited number of terms. As the number of terms increased, that edge slowly disappeared as expected.

Three hypotheses were tested in this study. The first hypothesis addressed whether sparser basis functions, when applied to satellite altimetry data, would lower RMS error when compared to the FT. The results of this study support acceptance of the hypothesis. In all tested cases, CWTs resulted in a lower RMS error, with only the Mexican Hat wavelet failing to do so in a few cases. It must be stated, however, that in these cases, there was little statistical difference between the Mexican Hat wavelet and the FT. The second hypothesis tested if theses same sparser basis functions would also increase resolution of predicted bathymetry. Here, results seem to indicate that in particular the Morlet wavelet had the ability to not only have the lowest RMS error with

the same number of coefficients but also to increase the level of detail captured in the predicted bathymetric images. Finally, the third hypothesis asked if taking the Fourier Transform of a continuous wavelet to compute wavelet coefficients would result in lower RMS error and result in an analytical solution to the wavelet transform of the gravitational potential anomaly. This method was applied only to the Mexican Hat Transform. The result was a quasi-analytical solution that indeed resulted in lower RMS error compared to the FT approach of computing gravitational potential anomalies.

Continued research should proceed on this topic in the following way. Based on the performance of the Morlet wavelet, greater efforts should be taken to test this transform in a variety of other regions in the ocean. Upward and downward continuation should be computed for at least the three tested continuous wavelets with more emphasis being placed on the Morlet wavelet. Although the Mexican Hat may prove to be easier to compute, every opportunity should be taken to solve continuity in the Morlet domain. Discrete wavelets were largely not considered in order to reduce the scope of work. It is, however recommended, that discrete wavelets also be considered as a viable option due to their well-documented de-noising ability. Finally, ridgelets should also be considered. The key advantage of directionality by ridgelets could be beneficial.

APPENDIX A – List of Symbols

U(P) – is the potential

γ – Newton's gravitational constant

σ – surface density

μ - point mass

k – wavenumber

ρ – density

λ – mass per unit length

γ* – Euler-Mascheroni constant

$\overrightarrow{r_0}$ – observation point

$\vec{r}$ – distance from the z-axis to the source point, where $\vec{r} = x\hat{x} + y\hat{y}$

$\vec{\xi}$ – 3D distance from the origin to the source point

$\overrightarrow{\xi_0}$ – 3D distance from the origin to the observation point

J_0 – zero-order Bessel function

Δg – vertical attraction

$h(\vec{r})$ – topography height

ψ – mother wavelet

ψ* – complex conjugate of ψ

s – scale

Ei – exponential integral

Δ_n – n^{th} order derivative

$\varphi(x)$ – 2-D Gaussian

Γ – Gamma function

$\mathcal{H}$ - Hankel Transform

g_0 – average acceleration of gravity

$\delta(t)$ – impulse function

ω – angular frequency

APPENDIX B Full Steps Between Equations 2.22 and 2.23

Starting with equation 2.22

$$U(P) = \gamma\lambda \left[ln\left|2z_2 - 2z_0 + 2\sqrt{z_2^2 - 2z_0z_2 + (r_0^2 + z_0^2)}\right| - ln\left|2z_1 - 2z_0 + 2\sqrt{z_1^2 - 2z_0z_1 + (r_0^2 + z_0^2)}\right|\right] \quad \text{(AB.1)}$$

Recall that z_1 = -a, z_2 = a and z_0 = 0. Substituting these values into equation AC.1 results in

$$U(P) = \gamma\lambda \left[ln\left|2a + 2\sqrt{a^2 + r_0^2}\right| - ln\left|-2a + 2\sqrt{(-a)^2 + r_0^2}\right|\right] \quad \text{(AB.2)}$$

Utilizing the properties of logarithms and setting $-a^2 = a^2$,

$$U(P) = \gamma\lambda\, ln\left[\frac{2a+2\sqrt{a^2+r_0^2}}{-2a+2\sqrt{a^2+r_0^2}}\right] \quad \text{(AB.3)}$$

Now factoring out and cancelling 2 we arrive at equation 2.23

$$U(P) = \gamma\lambda\, ln\left[\frac{a+\sqrt{a^2+r_0^2}}{-a+\sqrt{a^2+r_0^2}}\right] \quad \text{(AB.4)}$$

APPENDIX C The Proof of Parseval's Relation for Hankel Transforms

The following proof of Parseval's Relation for Hankel Transforms is taken from Debnath (1995).

The Hankel Transform of some functions f(r) and g(r) are set as:

$$\tilde{f}(k) = \mathcal{H}_n\{f(r)\} \text{ and } \tilde{g}(k) = \mathcal{H}_n\{g(r)\} \qquad \text{(AC.1, AC.2)}$$

Thus,

$$\int_0^\infty r\, f(r)\, g(r)\, dr = \int_0^\infty k\, \tilde{f}(k)\, \tilde{g}(k)\, dk \qquad \text{(AC.3)}$$

Proof:

$$\int_0^\infty k\, \tilde{f}(k)\, \tilde{g}(k)\, dk = \int_0^\infty k\, \tilde{f}(k)\, dk \int_0^\infty r\, J_n\,(kr) g(r)\, dr \qquad \text{(AC.4)}$$

The order of integration is interchangeable, thus rearranging we obtain:

$$\int_0^\infty r\, g(r)\, dr \int_0^\infty k\, J_n\,(kr) \tilde{f}(k)\, dk = \int_0^\infty r\, g(r)\, f(r)\, dr \qquad \text{(AC.5)}$$

APPENDIX D Proof of Equation 4.33

Lemma, from Jameson (1994)

Let

$$I = \int_{-\infty}^{\infty} e^{-x^2}\, dx \tag{AD.1}$$

We next will set A as the region in the (x,y) plane defined as

$$0 \le z \le e^{-x^2}, x \ge 0 \tag{AD.2}$$

After rotation of the region A about the z-axis, a new 3D region is formed, defined by

$$0 \le z \le e^{-x^2-y^2} \tag{AD.3}$$

Its volume is thus represented as

$$\int_{-\infty}^{\infty}\int_{-\infty}^{\infty} e^{-x^2-y^2}\, dxdy = I^2 \tag{AD.4}$$

However, as the volume was formed through the rotation about the z-axis, of the curve

$$x^2 = -\ln z,\ for\ 0 < z \le 1 \tag{AD.5}$$

It must equal

$$\int_0^1 \pi x^2 dz = \pi \int_0^1 -\ln z\, dz = \pi \tag{AD.6}$$

Recalling equation AE.4,

$$I^2 = \pi, thus\ I = \sqrt{\pi} \tag{AD.7}$$

APPENDIX E Nichols and Yates Proof

The below proof is taken from Nichols and Yates (1950).

Assume the following:

$$\int_0^\infty e^{-x^2}dx = A, \text{ where } \int_0^\infty = \lim_{h\to\infty}\int_0^\infty \cdot \qquad \text{(AE.1, AE.2)}$$

The surface $z = e^{-(x^2+y^2)}$ is produced by revolving the curve $z = e^{-y^2}$ about the z-axis.

The surface z then has the volume:

$$V = 4\int_0^\infty \int_0^\infty e^{-(x^2+y^2)}\,dxdy \qquad \text{(AE.3)}$$

Using the properties of exponents, we can separate the exponential into two parts and rearrange the equation as:

$$V = 4\int_0^\infty \left[\int_0^\infty e^{-x^2}dx\right] e^{-y^2}dy \qquad \text{(AE.4)}$$

Now substituting equation AF.1 into the AF.4:

$$V = 4\int_0^\infty A\, e^{-y^2}dy \qquad \text{(AE.5)}$$

Similarly for $e^{-y^2}dy$ we may substitute, resulting:

$$V = 4A^2 \qquad \text{(AE.6)}$$

If, however, the method of hollow cylinders is considered:

$$V = 2\pi\int_0^\infty y\, e^{-y^2}dy = \pi \qquad \text{(AE.7)}$$

We may then show

$$V = 4A^2 = \pi \qquad \text{(AE.8)}$$

Thus, we can see that

$$A = \frac{\sqrt{\pi}}{2} \qquad \text{(AE.9)}$$

We now see that indeed

$$\int_0^\infty e^{-x^2}\,dx = \frac{\sqrt{\pi}}{2} \qquad \text{(AE.10)}$$

REFERENCES

Abramowitz, M. (1964). *Handbook of Mathematical Functions with Formulas, Graphs and Mathematical Tables.* Wiley-Interscience.

Antonio F. Perez-Rendon, R. R. (2004). The convolution theorem for the continuous wavelet transform. *Signal Processing*, 55-67.

Argueso, F., J. Gonzalez-Nuevo, J. L. Sanz, L. Toffolatti, P. Vielva, D. Herranz and M. Lopez-Caniego (2006), The Mexican Hat Wavelet Family. Application to point source detection in cosmic microwave background maps. Monthly Notices of the Royal Astronomical Society. DOI: 10.1111/j.1365-2966.2006.10442.x

Bateman, H. (1954). *Table of Integral Transforms.* New York: McGraw Hill.

Blakely, R. J. (1995). Potential Theory in Gravity and Magnetic Applications. New York, Cambridge University Press.

Boas, M. L. (2005), Mathematical Methods in the Physical Sciences, 3rd ed., Wiley: Hoboken, NJ. ISBN: 0471198269.

Bracewell, R.N. (1965), *The Fourier Transform and Its Application* Second. J. V. Brown & M. Gardner, eds., New York: McGraw-Hill Book Company.

Chelton, D. B., J. C. Reis, B. J. Haines, F. Lee-Lueng, and P. S. Callahan (2001), Chapter 1 Satellite Altimetry, in Satellite Altimetry and Earth Sciences, Volume 69: A Handbook of Techniques and Applications (International Geophysics), edited, pp. 1-122, Academic Press.

Conrad, K. (n.d.). Differentiation under the integral sign. Storrs, Connecticut.

C. P. Nicholas, R. Y. (1950). The probability integral. *Mathematical Journal of America*, 412-413.

Daubechies, I. (1992), *Ten Lectures on Wavelets*. Society for Industrial and Applied Mathematics, Philadephia.

Debnath, L. (1995). *Integral Transforms and Their Applications.* Boca Raton: CRC Press LLC.

Elad, M. (2010), Sparse and Redundant Representations: from Theory to Applications in Signal and Image Processing, New York : Springer.

Gabor, D. (1946). Theory of Communication. *Journal of Institution of Electrical Engineers*, 429-441.

Garcia, E. S., D. T. Sandwell, and W. H. F. Smith (2014), Retracking CryoSat-2, Envisat and Jason-1 radar altimetry waveforms for improved gravity field recovery, Geophysical Journal International, 196(3), 1402-1422. doi: 10.1093/gji/ggt469

Gibbs, J. W. (1898). "Fourier's Series." Nature **59**(1522): 1.

David M. Glover, W. J. J., Scott C. Doney (2011). Modeling Methods for Marine Science. New York, Cambridge University Press.

Griffiths, D. J. (1981). Introduction to Electrodynamics. Upper Saddle, New Jersey.

Haxby, W. F., G. D. Karner, J. L. LaBrecque and J. K. Weissel (1983), Digital images of combined oceanic and continental data sets and their use in tectonic studies. EOS, 64(52), pp. 995-1004. Available at: http://onlinelibrary.wiley.com/doi/10.1029/EO064i052p00995/pdf.

Hofmann-Wellenhof, B., and H. Moritz (2006), Physical Geodesy, 2 ed., Springer Science & Business Media, New York.

Kellogg, O. (1953). *Foundations of Potential Theory.* New York: Dover.

Maysam Abedi, A. G.-H. (2014). A new stable downward continuation of airborne magnetic data based on Wavelet deconvolution. *Near Surface Geophysics*, 751-762.

Nathan J. Downey, R. W. (2007). A ridgelet transform method for constraining tectonic models via abyssal-hill morphology. *Geochemistry Geophysics Geosystems*.

NIST Digital Library of Mathematical Functions, http://dlmf. nist.gov/, Release 1.0.10 of 2015-08-07, National Institutes of Standards and Technology, access date: 2015-11-09.

Papoulis, A. (1962). The Fourier Integral and its Applications. New York, McGraw-Hill Book Company, INC.

Parker, R.L. (1972), The Rapid Calculation of Potential Anomalies. *Geophysical Journal International*, 31(4), pp.447–455. Available at: http://gji.oxfordjournals.org/content/31/4/447.short\nhttp://gji.oxfordjournals.org/cgi/doi/10.1111/j.1365-246X.1973.tb06513.x.

Pavlis N.K., Holmes S.A. Kenyon S.C., Factor J.K. (2012), The development and evaluation of the Earth Gravitational Model 2008 (EGM2008), Journal of Geophysical Research: Solid Earth (1978-2012) Volume 117, Issue B4, Art. JB008916. doi: 10.1029/2011JB008916.

Phillips G. M. and P. M. Taylor (1996). Theory and Applications of Numerical Analysis, 2nd ed., Academic Press: San Diego, CA. ISBN: 0-12-553560-0.

Piessens, R. (2000). The Hankel Transform. In *The Transforms and Applications Handbook.* Boca Raton: CRC Press LLC.

Rasmussen, H. O. (1993). The Wavelet Gibbs Phenomenon. Wavelets, Fractals, and Fourier Transforms. M. e. a. Farge. Oxford, Oxford University Press**:** 123-142.

Ryan, H. (1994), Ricker, Ormsby, Klauder, Butterworth - A choice of wavelets, CSEG Recorder.

Ryan W. B. F., Carbotte S. M., Coplan J. O., et al (2009), Global Multi-Resolution Topography synthesis. Geochemistry, Geophysics, Geosystems. doi: 10.1029/2008GC002332

Sandwell, D. T., R. D. Müller, W. H. F. Smith, E. Garcia, and R. Francis (2014), New global marine gravity model from CryoSat-2 and Jason-1 reveals buried tectonic structure, Science, 346(6205), 65-67. doi: 10.1126/science.1258213

Sandwell, D. T., and W. H. F. Smith (2009), Global marine gravity from retracked Geosat and ERS-1 altimetry: Ridge segmentation versus spreading rate, Journal of Geophysical Research-Solid Earth, 114, 18. doi: 10.1029/2008jb006008.

Scripps Institute of Oceanography (2014), Measured and Estimated Seafloor Topography, Website URL: http://topex.ucsd.edu/ WWW_html/mar_topo.html, retrived 20 November 2015.

Smith, W. H. F., and Sandwell, D.T. (1994), Bathymetric prediction from dense satellite altimetry and sparse shipboard bathymetry. *Journal of Geophysical Research*, 99(B11), pp.21803–21824.

Smith, W. H. F., and D. T. Sandwell (1997), Global sea floor topography from satellite altimetry and ship depth soundings, Science, 277(5334), 1956-1962. doi: 10.1126/science.277.5334.1956

Spiegel, M. R. (1968). *Mathematical Handbook of Formulas and Tables.* McGraw-Hill.

Starck, J. L., F. Murtagh, and J. M. Fadili (2015), Sparse image and signal processing : wavelets, curvelets, morphological diversity, New York, Cambridge.

Stegun, A. a. (1964). *Handbook of Mathematical Functions with Formulas, Graphs and Mathematical Tables.* Wiley-Interscience.

Téllez, M., R. Cerutti, and S. Trione (1997), Tables of Fourier, Laplace and Hankel Transforms of (u,n)-Dimensional Generalized Functions, Acta Applicandae Mathematicae, 48(3), 235-284. doi: 10.1023/A:1005721811911.

Thomson, R. E., William J. Emery (1998). Data Analysis Methods in Physical Oceanography. Oxford, Elsevier.

Torrence, C. & Compo, G. P. (1998), A practical guide to wavelet analysis. *Bams*, 79, p.61.

Vidakovic, Brani, P.M. (1991), Wavelets for Kids, A Tutorial Introduction. *American Meteorological Society*.

Weatherall, P., et. al (2015). "A new digital bathymetric modelof the world's oceans." Earth and Space Science: 331-345.

Wolfgang Torge, J. M. (2012). *Geodesy.* Berlin: Walter de Gruyter.

Wyld, H. W. (1999), Mathematical Methods in Physics, 2 ed., Persues Books, Reading,MA.